NONLINEAR DYNAMICS IN LATTICES OF BISTABLE ELEMENTS

by

Myungwon Hwang

A Dissertation

Submitted to the Faculty of Purdue University

In Partial Fulfillment of the Requirements for the degree of

Doctor of Philosophy

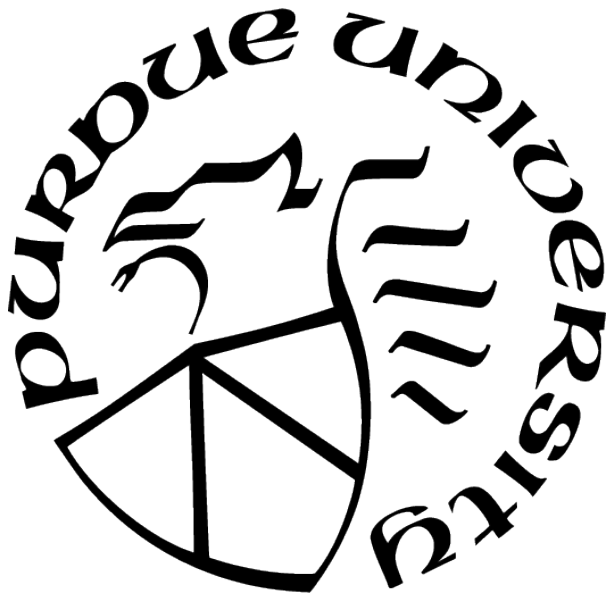

School of Mechanical Engineering

West Lafayette, Indiana

December 2020

THE PURDUE UNIVERSITY GRADUATE SCHOOL
STATEMENT OF COMMITTEE APPROVAL

Dr. Andres F. Arrieta, Chair

School of Mechanical Engineering

Dr. Fabio Semperlotti

School of Mechanical Engineering

Dr. Carlo Scalo

School of Mechanical Engineering

Dr. Pablo D. Zavattieri

School of Civil Engineering

Approved by:

Nicole L. Key

ACKNOWLEDGMENTS

It is a great honor to thank many people who made this thesis possible.

I cannot emphasize how grateful I am to ...

... my academic advisor, Prof. Andres F. Arrieta, for giving me the opportunity to work at Programmable Structures Lab. He has patiently waited for me to gain as much academic experience as possible and shaped me into a better researcher. I will always remember this piece of advice that enlightened me: "Think Simple."

... Prof. Carlo Scalo for giving me a chance to be involved in exciting research work and ushering me into the joy of computational analyses. His advice and encouraging words both in academic and personal life have been invaluable for me to move forward.

... Prof. Fabio Semperlotti and Prof. Pablo D. Zavattieri for being my committee advisors and providing me valuable feedback during the course of my Doctoral study. Their comments have led me to think more deeply and understand better about my project.

... my former advisor, Prof. Dewey H. Hodges, for having me equipped with solid fundamental knowledge and prepared for academic life. I have always wanted and am still pursuing to lead a life full of commitment like him.

Also, many thanks to ...

... my fellow PSL members. In particular, Janav, Aman, Katie, Matt, Sal, and Jose for creating a pleasant and entertaining working environment.

... my old friend, Scott Paik, for enriching my life with the years of good memories and stories since my undergraduate years.

Finally, I have to express my deepest gratitude to ...

... my cousin, Kimin Um, for having supported me in countless ways for the last 15 years. I have no words to express my gratitude for his help.

... my parents, Younghye Kim and Sunhong Hwang. They have always believed in me and provided me unconditional support for all of my decisions.

... my wonderful wife, Hyun Jin Cho for always being by my side and getting through the unprecedented pandemic period together. I could not have reached this milestone without your support and patience.

TABLE OF CONTENTS

LIST OF TABLES

LIST OF FIGURES

ABSTRACT

Lattices composed of bistable elements are of great significance across various fields of science and engineering due to their ability to support a class of solitary waves, called transition waves. Common with all solitary waves, transition waves carry highly concentrated energy with minimal degradation and thus have many useful engineering applications, such as extreme waveguides, bandgap transmission, vibration absorption, and energy harvesting. The rich dynamics arising from the strong nonlinearities of the constitutive bistable microstructures still have much to be unveiled for the practical implementation of the transition waves in real-world engineering structures. Especially, the quasi-particle characteristics of the transition waves can potentially address the performance limits posed by the unit cell size in linear metamaterials.

In this thesis, we first present an input-independent generation of transition waves in the lattices of asymmetric bistable unit cells when snap-through transitions occur at any site within the lattice. The resulting responses are invariant across the lattice except near the boundaries. These characteristics imply useful applications in broadband energy harvesting, exploiting the highly concentrated energy of the transition waves. We further observe that the inherent lattice discreteness induces dominantly monochromatic oscillatory tail following the main transition wave. This radiated energy of the tail can always be efficiently harvested through resonant transduction regardless of the input excitations. This type of bistable lattice transforms any input disturbance into an output form that can be conveniently transduced; thus, energy harvesting becomes an inherent metamaterial property of the bistable lattice.

To enhance the responses further for improved energy harvesting capability, we introduce engineered defects in the form of a mass impurity, inhomogeneous inter-site stiffness, and their combinations, achieving localization of energy at desired sites. Remarkably, we also observe a long-lived breather-like mode for the first time in this type of lattice. To enhance the tail motions globally across the lattice, we investigate the responses in a set of bistable lattices with the same mass and elastic densities but with different lattice spacing distances

(or lattice discreteness). From the available tail energy, we observe a significant increase in the harvesting capability with the increased lattice discreteness.

Next, the effect of functional grading on the onsite and inter-site stiffnesses are investigated to augment the control of the transition waves in the bistable lattices. The unidirectionality still remains in the direction of decreasing stiffness, while a boomerang-like wave reversal occurs in the direction of increasing stiffness. Both the compression and rarefaction transition waves are allowed to propagate, enabling continuous transmission of the transition waves without complex resetting mechanisms, thus expanding the bistable lattices' functionality for practical applications.

The observed input-independent dynamics of the one-dimensional bistable lattices can be extended to higher-dimensional metastructures by allowing macrostructural flexibility. Metabeams composed of spring-joined bistable elements are subjected to in-plane sinusoidal input at the microstructural level, and the out-of-plane responses at the macrosctructural level are measured. As long as transition waves are triggered within the metabeam, the most dominant output frequency occurs near the natural frequency of the macroscopic structure regardless of the input excitations initiating the transition waves, yielding energy transfer between uncorrelated frequencies.

Finally, high-fidelity in-house numerical solvers are developed for the massively parallelized computation of the problems involving generic bistable architectures, addressing the problem size limit. The improved numerical solution accuracy and computational performance, compared to those of commercial solvers, provide great potential to discover new dynamics by drastically expanding the accessible analysis regimes.

The experiments, simulations, and theoretical contributions in this thesis illustrate the possibilities afforded by strongly nonlinear phenomena to tailor the dynamics of materials systems. Importantly, the presented results show mechanisms to affect global dynamic properties unconstrained by the unit cell size, thereby offering new routes to extreme dynamics beyond current metamaterial architectures.

1. INTRODUCTION

1.1 Background

1.1.1 Acoustic Metamaterials

In the past two decades, the concept of metamaterials [3–5] has drawn significant research attention due to their potential to expand the feasible material property space [6]. In its most general definition, a metamaterial encompasses any material whose constitutive units are artificially engineered to exhibit unconventional mechanical (e.g., negative Poisson's ratio [7–9], negative thermal expansion coefficient [10–12]), acoustic (e.g., negative refractive index [13], negative effective mass density [14]), and electromagnetic (e.g., negative permeability and permittivity [15]) properties. Particularly, the dynamic properties of typical metamaterials can be fully characterized by the associated wave dispersion relations (or the band structures of the phonon, the quantum of the vibration) [16, 17], and the high tuning flexibility of the dispersion relations have been exploited to yield a myriad of engineering applications, such as transmission lines, noise control, energy harvesting, superlenses [18], and cloaking [19–21].

The dispersion relation mainly arises from two different mechanisms, namely, Bragg scattering [22] and local resonance [2, 23] [Fig. 1.1]. Bragg scattering occurs in a periodic arrangement of scatterers, where the interference between the incident and radiated waves control the allowed and prohibited bands for wave propagation. However, its engineering practicality is limited since the spatial gap needs to be of the order of the operating wavelength. That is, the size of the structures need to be impractically large to influence wave propagation at the low-frequency regime. For example, the artwork in Fig. 1.1(A), known to have the sound attenuation peak at 1,670 Hz, provides a qualitative idea of how large a structure need to be for low-frequency operations [1, 24]. On the other hand, the local resonance utilizes the inertial and elastic properties of the unit cell itself, theoretically enabling spectral gaps several orders smaller than the relevant wavelengths as long as the target mass and stiffness values can be realized. However, the tunability of these values are still restricted by physical sizes of the constitutive elements – for example, to achieve a unit cell with a low characteristic frequency, either the stiffness needs to be negligibly small (which would

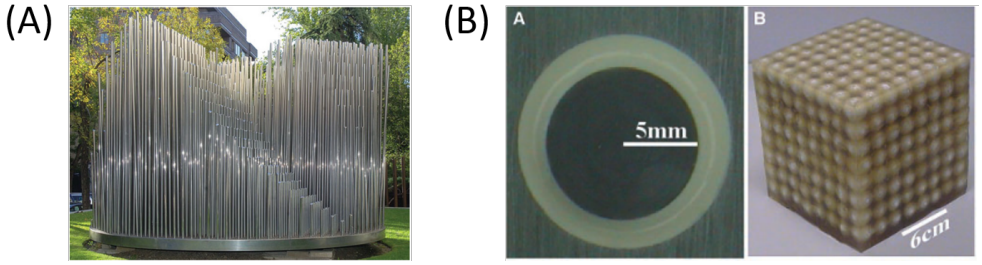

Figure 1.1. (A) Sempere's sculpture, exhibiting Bragg's scattering phenomenon (from Ref. [1]). (B) Locally resonant sonic materials (from Ref. [2]).

cause the loss of static stability of the structure), or the inertia needs to be impractically high (which would occupy a large space even with the densest materials available in nature). Hence, utilization of the local resonance is not entirely free from the size issue of the unit cells; there still exists physical limitation for allowed performance ranges.

Compared to abundant research on the behaviors of the metamaterials in the linear regime, the utilization of nonlinearities in metamaterials has still much to be explored. For structures involving weak nonlinearities (i.e., small perturbations while keeping the effect of the first few higher-order strain terms), the associated nonlinear dispersion relations can be obtained systematically [25–28]. The introduced nonlinearities make the dispersion relations amplitude-dependent and alter the location and size of the bandgaps [29, 30]. However, the expansion of the desired performance is only a small perturbation around the linearized counterpart; *the reliance on Bragg scattering or local resonance as the underlying mechanism for defining the metamaterials' dynamic characteristics still remains.* To surpass this performance limit, we need a fundamentally different mechanism to govern the dynamic characteristics of the metamaterials from the scattering or local resonance. A potential route is to exploit intrinsically nonlinear mechanisms with no linearized counterparts for the design of metamaterials. In §1.1.2, we present metamaterial architectures composed of bistable microstructures, enabling particle-like transmission of energy. Such architectures can potentially provide a transformative route to address the restricted operating bandwidth and surpass the existing performance limit set by the unit cell size.

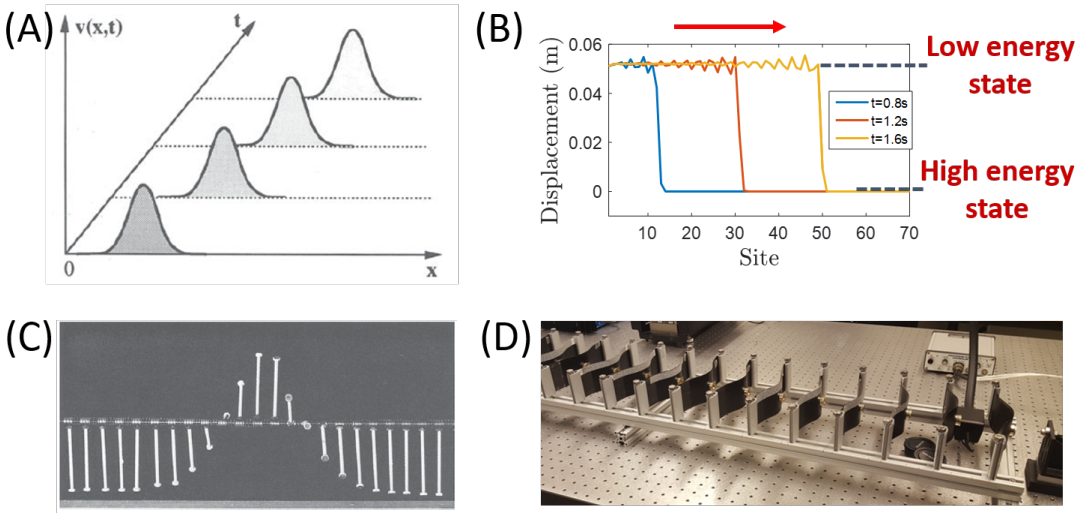

Figure 1.2. Typical shape of (A) a non-topological soliton (from Ref. [31]) and (B) a topological soliton. (C) Pendulum chain connected by torsional springs (from Ref. [32]). (D) Bistable latttice with asymmetric onsite potentials under magnetic interaction.

1.1.2 Solitary Waves

Solitary waves (or solitons in a less restricted sense) display uninterrupted propagation of stable pulses even in dispersive systems and are known as the most stable ways to transmit energy [33–35]. Not only their apparent merits in terms of stable propagation of energy but also their remarkable mathematical properties, appearing in the context of completely integrable systems [36–40], and great potential to explain many physical phenomena, such as shallow water waves [39], signal propagation in optical fiber [41, 42], gravitational waves [43], and DNA fluctuations [44], have attracted scientists in many different fields over the last half century. Solitary waves are also of practical importance in engineering applications since their generation requires nonlinear sources, which are present in any real physical systems, to cancel inherently dispersive effects.

There are two main classes of solitary waves: topological solitary waves and non-topological solitary waves. The term *topology* in this context is the topology of the potential energy surface of the system [45]. Any pulse whose waveform starts and ends at the same state is called a *non-topological wave* [see Fig. 1.2(A)]. On the other hand, one with different starting and end states is called a *topological wave* [see Fig. 1.2(B)]. Due to its state transitioning

characteristic of the waveform, the topological wave is also called a *transition wave* [46–49]. The very nature that its waveform is formed across two different energy wells makes the topological solitary wave more stable than the non-topological counterpart; that is, it requires much more energy to break the topological waveform. The governing equation of the system having topological solitary waves is invariant under Lorentz transformation, hence suitable for demonstrating special relativity. Also, the energy density of the topological solitary waves can be shown to have a localization with an effective mass, essentially behaving like a particle [31, 45]. Hence, its dual characteristics as a wave and particle have attracted the quantum mechanics community as well. Furthermore, simple models based on topological solitary waves can be used to explain macroscopic behaviors such as plasticity in materials [50–55], ferroelectricity [56], and Bose-Einstein condensate [57, 58].

Compared to the considerable amount of theoretical and numerical work revealing the existence and characteristics of the solitary waves, the experimental demonstrations of the solitary waves have been mostly limited in hydrodynamic [59–61] and optical systems [42, 62–64]. However, to transfer the extreme transport properties of the solitary waves into forming acoustic metamaterials, experimental realization in mechanical systems is essential. One successful implementation has been achieved in the context of granular chains [65, 66], where strong nonlinearity in the inter-site Hertzian contact force gives rise to a class of non-topological solitary waves. In terms of topological solitary waves, on the other hand, the experimental mechanical model has long been limited to the classical pendulum chain [32] [see Fig. 1.2(C)].

Topological solitons are strictly nonlinear phenomena implying that their behavior has no linear counterpart and cannot be analyzed by linearization, thus serving as a potential mechanism for creating nonlinear metamaterials. Recently, lattices composed of bistable unit cells [67, 68] under various forms of inter-site forces [69–73] have shown to exhibit stable propagation of topological solitary waves, or transition waves [see Fig. 1.2(D)]. In particular, the imposed asymmetry in each onsite potential interacts with the external dissipation and produces a unique unidirectional property [69, 70]. Using bistable elements as microstructure building blocks also has a particular advantage in constructing metamaterials since a collection of bistable elements can be readily manufactured into a structured material form,

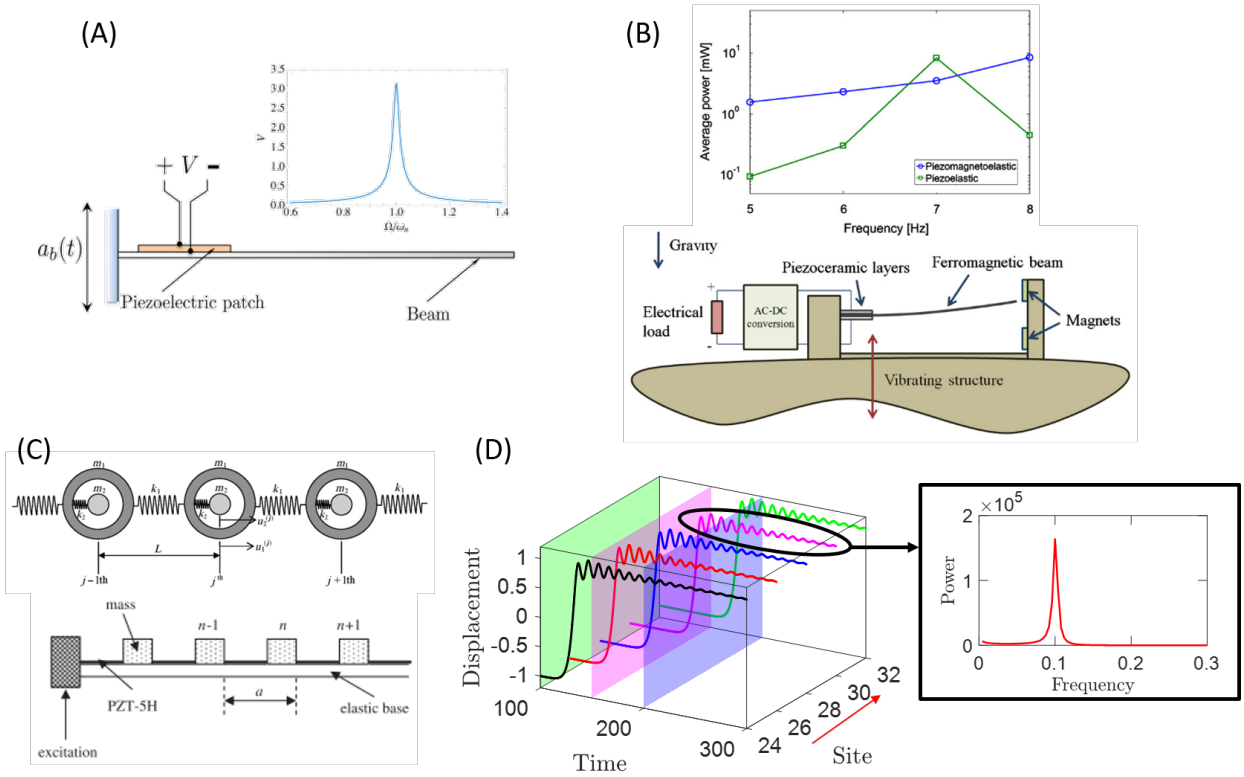

Figure 1.3. (A) Typical linear vibration energy harvester (from Ref. [74]). (B) Bistable nonlinear energy harvester and its power output comparison with monostable harvester (from Ref. [75]). (C) Metamaterial-based energy harvester designs (from Ref. [76, 77]). (D) Generation of oscillatory tail as a result of propagating snap-through transition at each site. The tail vibrates dominantly at a single frequency.

as opposed to the classical pendulum chains. If macroscopic dynamic properties can arise from such quasi-particle waves, we may potentially achieve a new mechanical platform that fundamentally breaks the tie between the unit cell design (determining the phononic band structure) and the resulting dynamic properties.

1.1.3 Broadband Energy Harvesting

Conventional linear vibration-based energy harvesters operate on the resonant excitation of the host structure [78–81]. This limits their optimal performance only to narrow bandwidths around the host structures' natural frequencies [see Fig. 1.3(A)]. Exploiting the dynamics of nonlinear oscillators has been one popular area of research to improve such

restricted bandwidth since coexisting solution branches generally allow a broader spectrum of response amplification [74, 82–88] [see Fig. 1.3(B)]. However, the harvester's fundamental reliance on its mechanical resonance still limits the usefulness only to a finite frequency band around the system's linear resonant frequency. As an alternate route, the idea of exploiting band gaps or energy-carrying waves in metamaterial-inspired structures has drawn research attention in that their locally-resonant building blocks allow for high flexibility in tuning the operational frequency bands and miniaturizing the harvester designs [76, 77, 89–96] [see Fig. 1.3(C)]. Even so, they are still not fully free from the size constraints since their performances fundamentally depend on the characteristic frequencies of the unit cells as introduced in §1.1.1. This implies that the metamaterial needs to be designed impractically large to achieve a low-frequency energy harvester.

This aspect can change drastically with the observation and implementation of solitary waves in nonlinear metamaterials as introduced in §1.1.2. As a corollary to the extreme directionality observed in the bistable lattices with asymmetric onsite potentials, it can be further identified that such lattices have response invariance that is totally independent of the types and intensity of the input excitations upon generation of transition waves in the lattice [97]. The response invariance applies not only to the main transition part of the wave but also to the radiated oscillatory tail resulting from the snap-through transitions of the unit cells. The motion of the tail, or phononic radiation, is dominated by a single frequency [see Fig. 1.3(D)] since it is essentially the free vibration around one of the stable equilibria, which originates from the local state transition imposed by the traveling topological soliton. This energy radiation as a transition wave propagates is a result of lattice discreteness, or in other words, the continuum is formed by an array of individual constitutive units. This input-independent nature and the response invariance are particularly beneficial for broadband energy harvesting in that we can transform any types of inputs, even quasistatic or random excitations, into a specific type of output that is convenient for power conversion as long as transition waves are triggered. Thus, we can achieve resonant transduction from the tail vibrations every time the unit cells are excited by the transition waves along the lattice. With an integrated power conversion mechanism at each unit cell, the bistable lattices can serve a supplementary function of powering small but crucial devices without

constantly matching resonant frequencies to the frequencies of the sources. In the sense that the harvesting capability is coupled to the ability to transmit transition waves, the bistable lattices can be regarded as intrinsically energy-harvesting metamaterials.

1.1.4 Response Enhancement in Metamaterials

In §1.1.3, we have shown that the energy in the single-frequency tails left behind propagating transition waves can be efficiently harvested through resonant transduction. Therefore, amplifying the induced tails is central to improving energy harvesting capability. One approach to enhance the tail vibrations is introducing engineered defects in otherwise periodic bistable lattices. The engineered defects are known to create spatially localized modes and have been widely exploited to focus energy at desired sites both in linear and nonlinear waveguides [98–103]. In this thesis, defects in the form of mass impurities and inter-site force disparities are utilized to concentrate the wave energy at specific sites of the bistable lattice with asymmetric onsite potentials.

Since the radiation of the trailing vibrations occurs as a result of the inherent discreteness of the lattice, we can also manipulate the degree of the lattice discreteness to enhance the transducible tail energy collectively across the lattice. The effect of the lattice discreteness on the propagation properties of the transition waves have been investigated analytically and numerically [104–107]. However, the studies on the discreteness effect on the generated tail motions and accordingly the energy harvesting capability are still rare findings. To that end, we prepare a set of equivalent bistable lattices with varying stiffness ratios between onsite and inter-site elements, otherwise having the same macroscopic inertial and elastic densities. The trade-offs between the wave transport properties and the enhanced transducible tail motions as a function of lattice discreteness is numerically investigated, providing design maps for desired applications.

1.1.5 Augmenting Control of Transition Waves

The unidirectionality of the transition waves in the bistable lattices introduced in §1.1.2 provides an ideal implementation for high-fidelity transmission lines and protective materi-

als that can re-route any destructive events away from the crucial infrastructures. In the continuum limit, an assembly composed of symmetric bistable lattices can be approximated into a Klein-Gordon equation with ϕ-4 potential, assuming we keep the bistable strain potential up to 4^{th}-order terms only. The exact solution for this equation exists in the form of $\phi(x,t) = \pm \tanh \frac{x-vt}{\sqrt{2}\sqrt{1-v^2}}$ [45]. The solution with the plus sign corresponds to the kink solution, and the one with the minus sign corresponds to the anti-kink solution. In contrast, the studied bistable lattices supporting unidirectionality can only support a single type of the topological solitary waves (either kink or anti-kink depending on the initial arrangement of the bistable elements). This is due to the introduced asymmetry in the bistable onsite potential, which is required to overcome the inherent dissipation in any real physical systems. Therefore, the functionalities of the studied bistable lattices for broader applications are limited in that a separate resetting mechanism is required for a continuous operation. One mathematical model inspired by the reactive biological mechanism has shown the reversible transmission of the transition waves [108]. However, passive mechanisms to enhance the manipulation of the transition waves are yet to be discovered.

Identifying that having symmetric bistable potentials is a necessary condition to allow response symmetry between two stable equilibrium configurations, we can alternately utilize functionally graded lattice properties while keeping the symmetry of the bistable potentials to achieve stable transition wave propagation. This approach can be understood as continuously reducing the potential barriers the transition waves need to overcome. The dynamics of the perturbed Sine-Gordon models [109–113] or ϕ-4 models [114–117] in the presence of a single or stochastic inhomogeneity have been studied analytically and numerically in the past. In this thesis, we use the perturbation approach around the known soliton solutions to investigate ϕ-4 model under spatially varying inertial or elastic properties in the presence of system damping. The resulting stability and directionality of the transition waves can potentially enhance the control of transition waves without aid from any external or active resetting mechanisms.

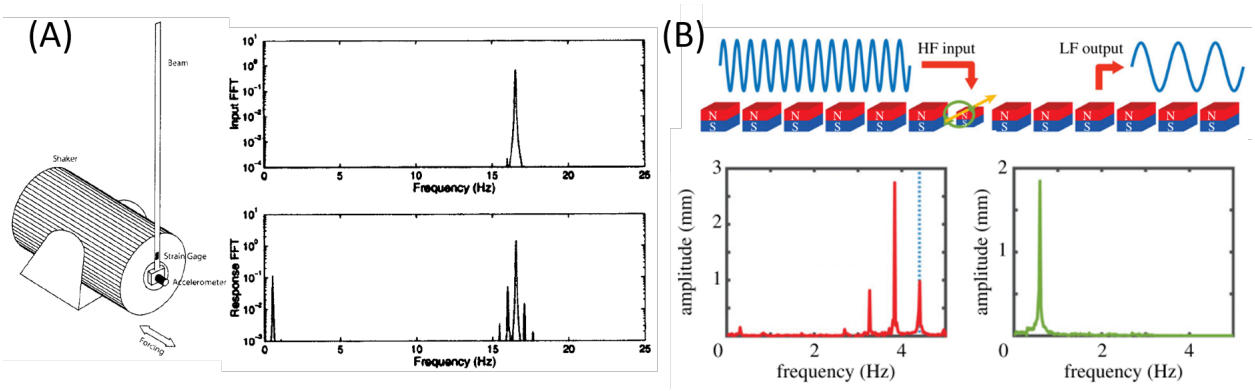

Figure 1.4. (A) Frequency conversion between normal modes through nonlinear coupling (from Ref. [118]). (B) Frequency between a defect and extended modes. Fourier spectrum at the input site is plotted in red, and the spectrum at the measuring site is plotted in green (from Ref. [119]).

1.1.6 Frequency Conversion

Transformation of a motion into another with different frequency components is useful for speed control [120] and energy harvesting [87, 121, 122]. Compared to the ample research work in photonic systems [123–128], frequency conversion in mechanical systems remain largely unexplored. Similar to the practice in photonics, existing frequency conversion methods in mechanical systems utilize nonlinearities of the systems. In nonlinear single-degree-of-freedom systems, frequency conversion can appear as subharmonic/superharmonic resonances, or the presence of multiple input frequencies amount to the summation or the difference of the constituting frequencies [129, 130]. Even richer dynamics can be observed in multi-mode systems, where energy can be transferred between linear normal modes through nonlinear coupling [118, 131] [see Fig. 1.4(A)]. Recently, inter-modal energy exchange through nonlinearly generated higher harmonics in lattice structures has been theoretically and experimentally investigated [132–134]. In addition, almost complete high to low-frequency conversion has been demonstrated in magnetic metamaterials with a defect through the coupled resonance of the localized defect mode and extended lattice modes [119] [see Fig. 1.4(B)]. However, all of the above frequency conversion methods require the desired target frequency to be of specific relationships (e.g., commensurate) to the input frequencies and normal modes of the systems, which is not ideal for truly broad operating conditions.

One notable technique free from the limited input frequency requirement is the utilization of frequency up-conversion [135]. Nevertheless, this technique requires either the source or the internal mechanisms to be impulsive to excite the natural modes of the vibrating structures.

Inspired by the impulsive excitation of the natural modes, one potential solution for energy exchange between incommensurate frequencies can be found in metamaterials supporting transition waves. As introduced in §1.1.2, transition waves exhibit particle-like characteristics, which can be utilized as traveling quasi-particles exciting the normal modes of the systems. This mechanism is an extension of the input-independent dynamics present in the 1-D bistable lattices to a higher-dimensional system. For the 1-D lattices, the presence of the extreme dynamics at the unit cell level makes it difficult to access them for practical implementations – for example, energy transduction mechanisms need to be integrated at the microscopic level. Hence, transcending the input-independent behaviors to a larger scale, where the resulting dynamics can be more readily accessible, is desired. In this thesis, we seek to develop a generic architecture that takes advantage of the quasi-particle nature and the input-independence of the transition wave to achieve energy transfer between incommensurate frequencies at two different size scales.

1.1.7 Extreme Computational Scaling

For the acoustic metamaterials operating in the linear or weakly nonlinear regime, the focus is mostly on finding and tuning the band structures, which can be obtained by analyzing the single unit cell with either Bloch wave theorem [136] or transfer matrix method [137]. Hence, computational efficiency has not been a major restraining factor for the analyses of most metamaterial designs. For metamaterials leveraging unit cell's strong nonlinearity, exact solutions are in general not available. Thus, there is a need to seek numerical means to explore the metamaterials' rich nonlinear dynamics fully. However, even for strongly nonlinear systems, many metamaterial designs are confined to a one-dimensional space, or the interest lies in wave generations rather than the full-scale structural behaviors. Thus, any general commercial solvers or ad-hoc programs written in high-level programming languages have sufficed the needs for their analyses. Nevertheless, for practical engineering applications, metamaterials need to be miniaturized or used as building blocks for even larger-scale

macrostructures whose dynamics span beyond a one-dimensional space. Such analyses would require the computation of millions of unit cells. Solving a nonlinear problem for such a large number of degrees of freedom would be challenging even with the most powerful computer systems available to date. Thus, an efficient computational implementation is needed.

When numerically solving spatiotemporal problems, the determination of the current temporal state cannot be made without the computation of the previous states; computations in the temporal domain are strictly sequential jobs. However, the spatial data can be processed at any order within each time step. The inherently periodic arrangements of the metamaterials provide an advantageous condition for efficient parallel computation. In this thesis, we implement a dedicated in-house computational tool with message-passing interface (MPI) libraries to allow massively parallelized computation of the problems involving general architectures composed of bistable or multistable elements. The high scalability with the number of processes enables not only an efficient and expeditious workflow but also a potential for investigating rich nonlinear dynamics previously inaccessible due to the massive problem sizes.

1.2 Objectives

The fundamental goal of this thesis is to uncover rich nonlinear behaviors in the lattices with bistable unit cells and to utilize the observed dynamics for engineering applications. To that end, the following specific objectives are set:

1. To construct metamaterials whose dynamic characteristics are dictated by quasi-particle behaviors of the transition waves, breaking the strong dependence of the dispersion relations on the constitutive microstructures. This leads to the responses having weak dependence on the input excitations as long as transition waves are generated.

2. To demonstrate experimentally broadband energy harvesting in bistable lattices with asymmetric onsite potentials, taking advantage of the generation of the input-independent monochromatic tails as a result of the transition waves.

3. To establish the relative importance of factors enhancing the propagation properties and radiated vibration energy of transition waves by breaking the periodicity of the microstructures and by manipulating lattice discreteness.

4. To augment the directional control of transition waves by introducing stiffness grading in either inter-site or onsite members. This enhances the utility of transition waves in real-world applications.

5. To extend the input-independent dynamics to higher dimensional structures, achieving nonlinear interaction between two disparate size scales. This allows energy transfer from broad inputs in microstructure to a single coherent output in macrostructure.

6. To develop an efficient computational tool for analyzing large-scale general bistable or multistable architectures. This enhanced computational capability allows access to the previously unreachable analysis domains, potentially uncovering new, interesting dynamics.

1.3 Thesis Contributions

The novelty of this compilation work lies in the conceptual development of generic bistable architectures with unconventional dynamic properties that are applicable across various fields of physics – that is, the observed dynamic properties are not restricted to specific designs or implementations. The following is the list of the resulting original contributions from this thesis:

1. The dynamics of bistable lattices are investigated, establishing transition waves as a mechanism to achieve input-independent and highly coherent responses in metamaterials. This provides a means to bypass the strong limits imposed by the conventional frequency proportionality in linear and weakly nonlinear systems. This remarkable property allows for multi-functional metamaterials with built-in broadband energy harvesting capability. (see Ch. 2 as published in Scientific Reports, 2018.)

2. We identify the role of the transition-wave-induced monochromatic tail vibration on the energy harvesting capability of bistable metamaterials. Response enhancement

strategies are presented in terms of the introduction of engineered defects (see Ch. 2) and increased lattice discreteness (see Ch. 3 as published in Proc. SPIE, 2019). These strategies increase the harvesting capabilities either locally or globally in the bistable lattices, and stable breather-like modes are also observed.

3. The periodicity of the bistable lattice is perturbed by functionally grading the lattice stiffness to augment the control of the transition waves. Interesting Boomerang-like beaming is observed, and the existence of both compressive and rarefactional transition waves are demonstrated, which expands the utility of the bistable lattice in real-world applications. (see Ch. 4 as published in Physical Review E, 2018.)

4. The input-independent characteristics of the transition waves in a one-dimensional bistable lattice can be extended to interact with the macro-scale dynamics. The conversion from an input excitation in lattice-level to a coherent output response in (meta)structural level is demonstrated by utilizing metastructures composed of bistable microstructures with allowed transverse degrees of freedom. The simple physics governing the input bandwidth and output frequency allows for extreme tuning flexibility, enabling energy transfer between incommensurate frequencies several orders of magnitude apart. (see Ch. 5)

5. A high-fidelity simulation tool that can run on millions of parallel processes for analyzing generic bistable metastructures is developed. The high scalability with the number of processes enables the potential for investigating rich nonlinear dynamics previously inaccessible. The tool is implemented to be easily upgradable to cover higher-dimensional problems upon the development of such models. (see Ch. 6)

In addition, the studied dynamics can promote the following future contributions:

1. Even though an abundance of theoretical and numerical work has been performed proving the existence of breathers, the inevitable external dissipation causes difficulty in observing them experimentally. A bistable lattice will be manufactured with low-damping materials, and the existence of topological breathers will be experimentally demonstrated in a mechanical lattice.

2. In quantum mechanics, de Broglie wave is allowed to have negative kinetic energy, enabling the nonzero probability of a particle tunneling through classically forbidden potential barriers. A transformation of low-energy non-topological soliton into higher-energy topological soliton, which is classically forbidden, will be demonstrated by breaking the periodicity of the bistable lattice.

2. INPUT-INDEPENDENT ENERGY HARVESTING IN BISTABLE LATTICES FROM TRANSITION WAVES

Myungwon Hwang, Andres F. Arrieta

This chapter is published in:
Scientific Reports, 2018, 8, 3630.
DOI: 10.1038/s41598-018-22003-7
Supplementary Information is attached as Appendix A.

2.1 Abstract

We demonstrate the utilisation of transition waves for realising input-invariant, frequency-independent energy harvesting in 1D lattices of bistable elements. We propose a metamaterial-inspired design with an integrated electromechanical transduction mechanism to the unit cell, rendering the power conversion capability an intrinsic property of the lattice. Moreover, focusing of transmitted energy to desired locations is demonstrated numerically and experimentally by introducing engineered defects in the form of perturbation in mass or inter-element forcing. We achieve further localisation of energy and numerically observe a breather-like mode for the first time in this type of lattice, improving the harvesting performance by an order of magnitude. Our approach considers generic bistable unit cells and thus provides a universal mechanism to harvest energy and realise metamaterials effectively behaving as a capacitor and power delivery system.

2.2 Introduction

The utilisation of nonlinearity in vibration-based energy harvesting has been widely studied for improving the restricted bandwidth in which energy can be efficiently converted [74, 83–86, 88, 138–143]. Recently, the high tunability of the band structures in phononic crystals has drawn a significant attention from researchers as an alternate route to achieve the broad-band energy harvesting [77, 89, 90]. However, the fundamental reliance on mechanical resonances and band gaps to convert energy from oscillatory sources restricts its applicability

to finite frequency bands. This problem is exacerbated by the dimensional limit constraining resonant conversion at low structural frequencies in view of the inverse relationship between size and natural frequency; harvesting at low frequencies implies the use of impractically large devices. The research efforts have been extended to metamaterial-based energy harvesting concepts [76, 91–93, 95, 96], whose locally resonant feature offers unit cell designs in subwavelength scales and more tuning flexibility in band gap formation [2, 4, 144]; several authors have specifically addressed the challenge of the scalability [94, 145]. Nonetheless, the optimal operating frequencies are still relatively high compared to the typical frequency range of the structural sources [146, 147], and their harvesting performances depend on the frequency, types, and strengths of the input excitations. Moreover, the operation principle through focusing dispersive waves fundamentally constrains the robust harvesting of energy to a small specific area only.

Nonlinear metamaterials capable of sustaining solitary waves for a broad class of inputs may simultaneously address the problems posed by dispersion, high frequency, and narrow-band conversion. In the context of a granular chain [66], Ref. [148] has demonstrated the harvesting of energy from solitary waves arising from low-frequency impulse excitations using a nonlinear medium itself as a means to concentrate energy to a focal point, where piezoelectric conversion is conducted. Ref. [149] has laid a foundational work on harvesting energy from non-topological solitary waves within a granular lattice through an embedded piezoelectric sensor. However, the study of topological solitons and associated dynamics for energy harvesting has received much less attention.

We demonstrate that the invariance of transition waves to different boundary inputs in 1D lattices of bistable elements [48, 69, 70] enables the concentration, transmission, and harvesting of input energy independently from the excitations. We calculate the amount of available energy to be harvested from the topological transition waves and introduce electromechanical unit cells, allowing for the design of metamaterials with inherent capacity to harvest energy carried in the form of transition waves. In addition, engineered defects [98–103] are utilised to further manipulate the lattice dynamics. A single or distributed defect(s) introducing mass and/or inter-element forcing perturbations to the lattice periodicity allow us to focus energy in a specific lattice region, enabling an efficient method for transduction.

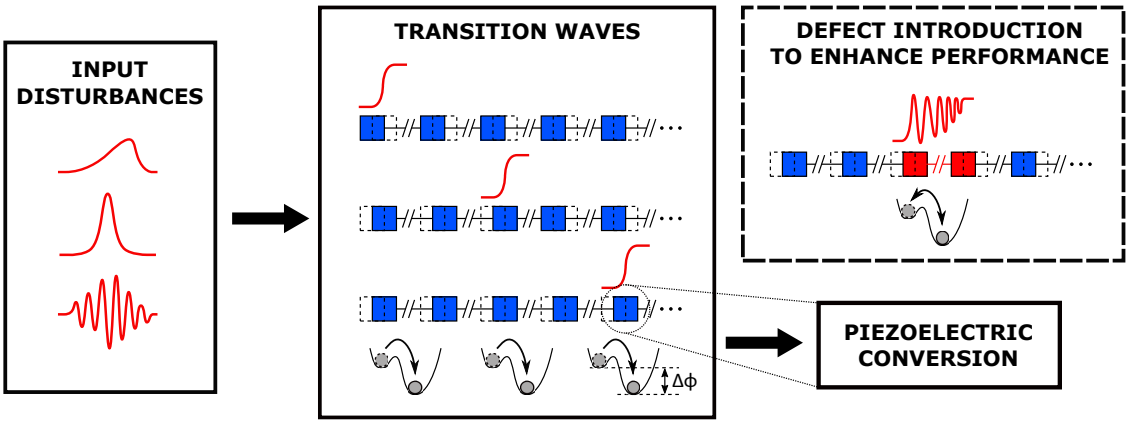

Figure 2.1. Conceptual work flow of energy harvesting from transition waves in bistable lattices.

Our numerical simulations reveal the presence of breather-like modes, enabling the transduction of energy triggered by a transition wave into an oscillatory form, thereby creating a mechanism to deliver power from the lattice over a longer time period. This system behaves as a mechanical capacitor with a tunable discharge rate capable of delivering electrical energy. The used bistable unit cells are generic and can be realised through a broad range of architectures [150–153]. Therefore, the uncovered dynamics allow for creating a general robust lattice-intrinsic mechanism for transmitting, focusing, and converting energy from motion, giving rise to inherently harvesting metamaterials as illustrated in Fig. 2.1.

2.3 Bistable Lattice Model

The studied model is based on a 1D periodic lattice of bistable elements connected by inter-element magnetic forces [69]. Figure 2.2 shows a schematic representation of the lattice and the experimental setup used throughout. The experimental lattice model is built using 15 identically prepared bistable elements fabricated from carbon fiber reinforced composite laminates [67]. The input excitation is applied at the first site, and three measuring sites (9^{th}, 10^{th}, 11^{th}) within the lattice are selected for the analyses to minimise any unwanted boundary effects. The dynamic response of the lattice is captured by a commercial high-speed digital image correlation system (VIC-3D).

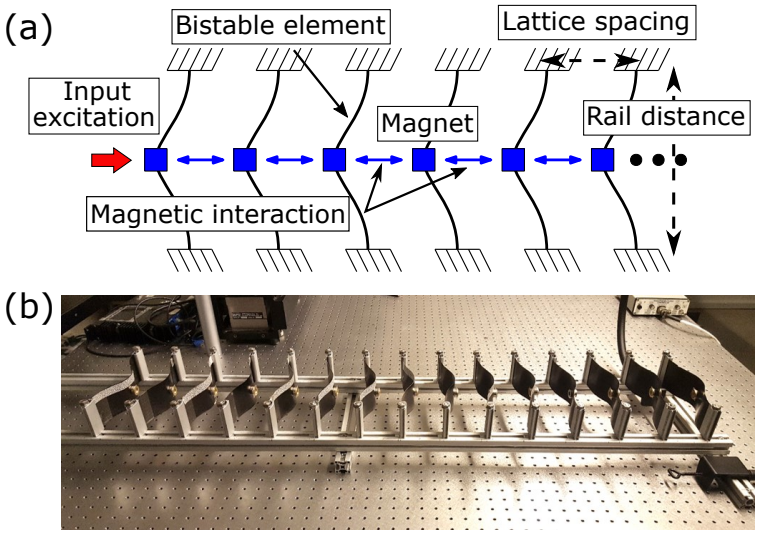

Figure 2.2. (a) Schematics and (b) experimental setup of the lattice with bi-stable unit cells.

The system is studied numerically with a discrete analytical model governed by the advance-delay differential equation given by

$$m\ddot{u}_n = \mathcal{F}_{mag}(u_{n-1}, u_n, u_{n+1}) + \mathcal{F}_{onsite}(u_n) - b\dot{u}_n, \tag{2.1}$$

where u_n is displacement at n^{th} site from the static equilibrium with the higher energy potential, and overdot represents derivative with respect to time. The inter-element magnetic force and the on-site force are given by

$$\begin{aligned} \mathcal{F}_{mag} &= -A(u_{n+1} - u_n + L)^p + A(u_n - u_{n-1} + L)^p, \\ \mathcal{F}_{onsite} &= -2C_2u_n - 3C_3u_n^2 - 4C_4u_n^3. \end{aligned} \tag{2.2}$$

The following baseline lattice parameters are used unless specified otherwise: mass $m = 29.4$ g, lattice spacing $L = 0.07$ m, rail distance $R = 0.225$ m, and the element damping $b = 0.52$ Ns/m. The choice of element damping is made to approximate the decay rate exhibited by the experimental system. The measured values for the magnetic interaction parameters A and p and for the coefficients C_2, C_3, and C_4 of the cubic force functions are specified in Supplementary Fig. 1. Newmark-β method [**chopra2012**] is used to numerically study

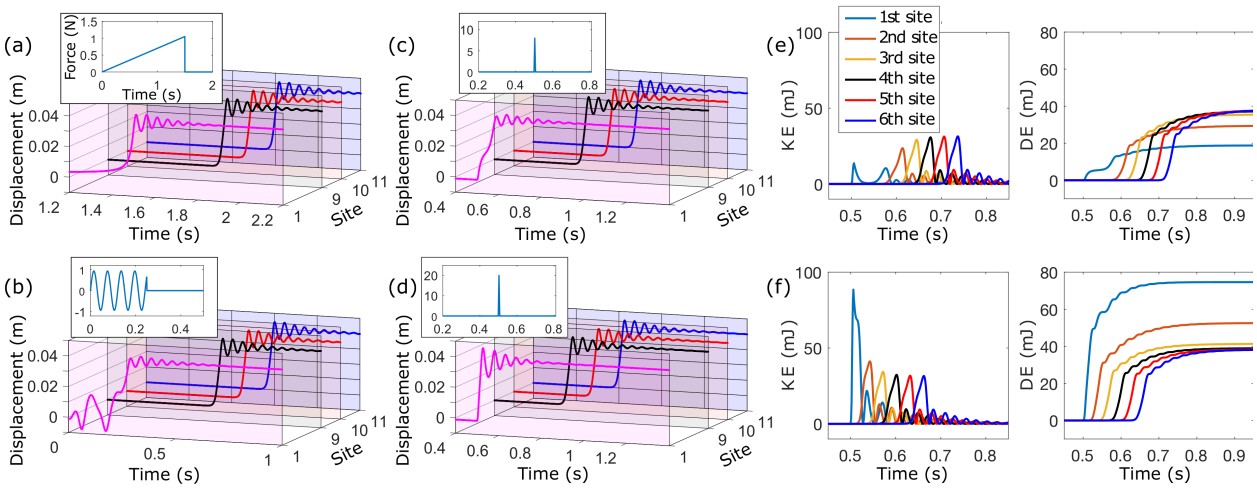

Figure 2.3. Lattice responses generating transition waves for different input forces applied at 1st site: (a) quasi-static, (b) sinusoidal within the pass band, and (c),(d) impulse-like loads with different intensities. Kinetic and dissipated energies at each site under impulse-like loads of (e) low and (f) high levels.

the responses of the unit cells as transition waves propagate. We choose a sufficiently large number of elements (N=500) to simulate a semi-infinite boundary.

2.4 Response Invariance

In the linear regime, the dispersion relation between the nondimensionalised wave number $\bar{k}$ and frequency $\bar{\omega}$ is obtained as

$$\bar{k} = \pm 2 \arcsin \sqrt{\frac{-\bar{\omega}^2 - \mathrm{i}\bar{\omega}\bar{b} - \bar{\mathcal{F}}_{onsite}(\bar{u}_n^*)}{4p}}. \tag{2.3}$$

The presence of an imaginary part contributes to wave attenuation, and thus phonons disintegrate eventually in a physical setup, where damping is always present ($\bar{b}$>0) – see Supplementary Information for the derivation of the dispersion relation and phonon transmission.

However, a very different aspect can be observed when a transition wave is generated. The time responses of the elements at the input and measuring sites under a quasi-static application of load, sinusoidal excitation, and impulse-like excitation are shown in Figs. 2.3(a), (b) and (c), respectively. Additionally, the response under a higher-intensity impulse [Fig. 2.3(d)] is presented. Although the response form and the time it takes to trigger snapthrough of the

first element are different for each excitation condition, the responses at the measuring sites (9^{th}, 10^{th}, 11^{th}) are essentially the same for all four cases. This shows that the waveform is preserved along the path of propagation (except near the lattice boundaries) as long as the initial state transition is triggered by any means, thus input-invariant response.

The invariant lattice response is validated experimentally by using quasi-static and impulsive inputs of various rates and intensities on the demonstrator shown in Fig. 2.2(b). For all the explored cases, a stable transition wave is formed as long as the first element snaps through to its second state, three of which are shown in Supplementary Video 1-3. Given the unidirectionality of the lattice theoretically and experimentally shown in Ref. [69], any input triggering a snap-through of any unit cell in the lattice results in the stable propagation of a transition wave. This assures the input-invariant behaviour of the response in the lattice.

Taking advantage of the response invariance at every site, each element forming the lattice can contribute to the harvesting of energy, provided that transduction mechanism is installed at every site. The minimum static force required to initiate the state transition is 0.56 N for a single bistable element (from the force-deflection curve); this value increases to 0.95 N for an array with more than three elements (see Supplementary Fig. 3). Although nearly double amount of input force (thus energy) is needed to trigger the snap-through for the array, the latter snapping force remains unchanged regardless of the size of the array, implying that it can attain a significantly higher energy output to input ratio than a single-element energy harvester does.

2.5 Harvested Energy

To calculate the total energy in the system, the governing equation is multiplied by the unit-cell velocity $\dot{u}_n$, integrated over time and summed over all elements, yielding

$$\sum_{n=1}^{N} [\underbrace{\frac{1}{2} m \dot{u}_n^2}_{\text{KE}} + \phi(u_n)] - \sum_{n=1}^{N-1} \frac{A}{p+1} (u_{n+1} - u_n + L)^{p+1} = - \sum_{n=1}^{N} \underbrace{\int b_{tot} \dot{u}_n^2 dt}_{\text{DE}}, \tag{2.4}$$

where b_{tot} is the total effective damping, and KE, $\phi(u_n)$, and DE are the kinetic, on-site potential, and dissipation energies for each unit cell, respectively. The available energy from

the motion of each unit cell may be divided into three parts: (1) the initial vibration from the phonon transmission, (2) the state transition from the high to low energy state, and (3) the oscillatory tail behind the main transition wave front. The first contribution is negligible according to the earlier discussion. The third contribution can be considered as excess energy, which does not affect the stability of the transition wave, and can be advantageously tuned to induce large oscillatory tails for optimizing the harvested energy of the lattice.

Figures 2.3(e) and 2.3(f) compare the kinetic and dissipated energies at each site under two different levels of impulse excitations. With the interaction between the stored energy (due to the asymmetry in the strain potential) and the damping of the on-site element, any deficiency or excess in input energy is self-adjusted to the level dictated by the lattice's intrinsic properties, acting as a power regulator. With a marginal input to trigger the snap-though of the first element, the stored potential continues to supply energy over the course of propagation until the state transition is eventually stabilised [Fig. 2.3(e)]; on the contrary, any excess input energy is rapidly dissipated in the first few elements until the transition motion stabilises [Fig. 2.3(f)]. For the given baseline experimental lattice setup, the stabilisation occurs in approximately four elements.

Rather than developing a specific coupling relation for each different transduction mechanism, the mechanical to electrical conversion may be represented as an additional damping d for simplicity [154]. This gives the total effective damping $b_{tot} = b^* + d$, where b^* captures the modified mechanical damping due to the added mechanism. The total harvested energy from a single element can then be calculated as $\int_0^\infty d(\dot{u}_n)^2 dt$. This is the cumulative energy that the harvester can draw from the motion of a single element. The power output, which is a more standard performance measure in harvesters under cyclic excitations, may also be obtained in the average sense by dividing the cumulative energy by the time period of the input.

The stability of the transition wave must be ensured in order to allow for the input energy to be transmitted and converted. To study the critical value of the total damping still enabling electromechanical conversion from the transition wave, we define the harvested energy factor as the converted energy from a single element divided by d and plot this value as a function of the total damping b_{tot} in Fig. 2.4(a). This shows that the transition

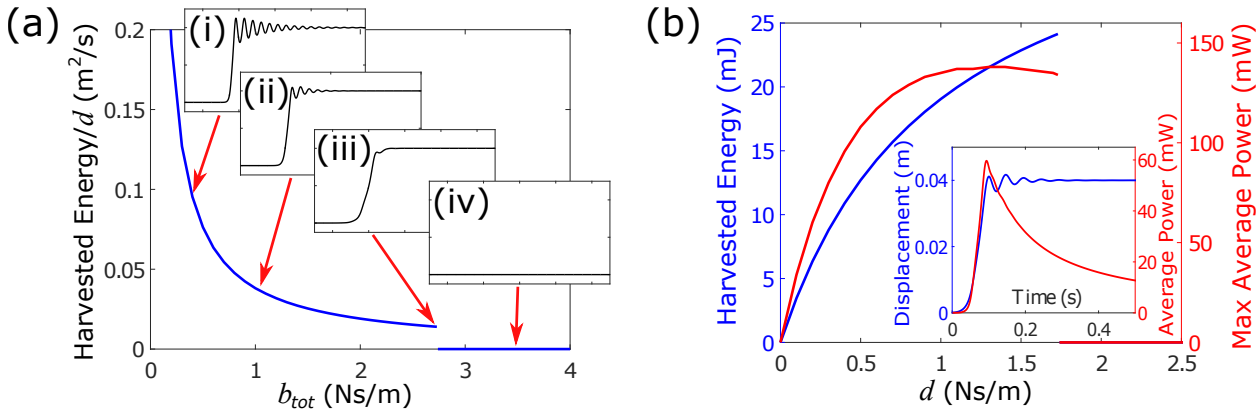

Figure 2.4. (a) Harvested energy factor at a single site of periodic lattice vs. the total damping of the lattice: corresponding responses to values (i) b_{tot}=0.4 Ns/m, (ii) b_{tot}=1.0 Ns/m, (iii) b_{tot}=2.73 Ns/m, and (iv) b_{tot}=3.5 Ns/m are plotted in the insets. (b) Total harvested energy and maximum average power for a fixed b^*=1.0 Ns/m.

waves disintegrate for $b_{tot} > 2.73$ Ns/m, resulting in no harvested energy. For the limiting case $b_{tot} = 2.73$ Ns/m, the response shows state change occurring without any oscillatory tails [inset of Fig. 2.4(a)]. For a given transduction coupling d, any reduction in structural damping results in a higher response speed and generation of the greater oscillatory tail, both of which can increase the energy harvested by the system. Assuming b^* is fixed, on the other hand, the cumulative harvested energy from a single element monotonically increases with an increasing d [blue curve in Fig. 2.4(b)]. The maximum average power occurs toward the end of the transition motion [inset of Fig. 2.4(b)]. As a result, there is a trade-off in the maximum average power that can be achieved with increasing d since such change tends to slow the transition speed. This behaviour is observed in the maximum average power plot (red curve), where the peak occurs slightly below the limiting value of d that allows stable propagation of a transition wave. In the limit, the maximum possible energy that can be converted is the strain energy stored in the lattice, implying the lattice behaves as a mechanical capacitor from which packets of energy can be drawn and transmitted as transition waves.

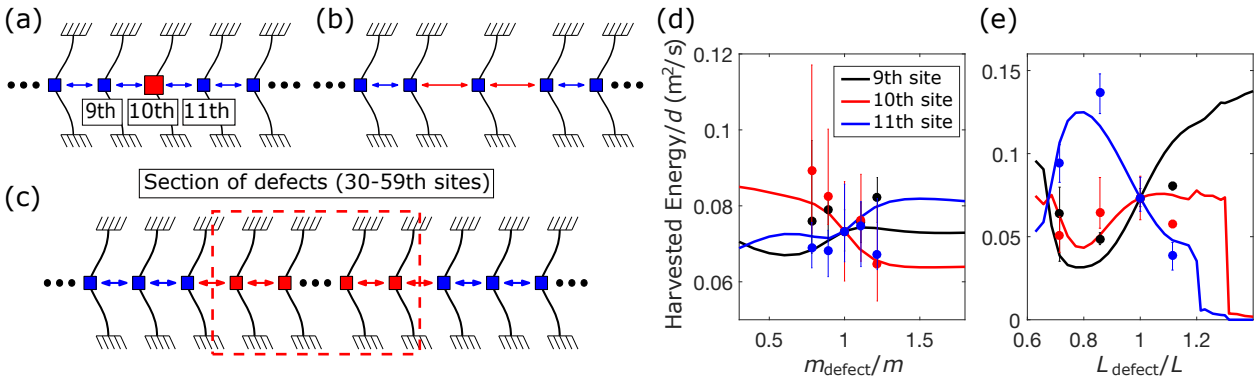

Figure 2.5. Schematic representations of (a) mass defect, (b) inter-element forcing defect applied by adjusting the local lattice spacing distance, and (c) lattice containing a section of engineered defects. (d),(e), Available energy factor for harvesting under the presence of mass and lattice spacing defects, respectively. The dots represent the experimentally obtained results, and the defect is located at the 10^{th} site.

2.6 Engineered Defects for Energy Harvesting

To best exploit the energy stored within the lattice, engineered defects can be considered as means to concentrate the conversion to a few selected elements, thereby enabling harvesting at specific sites of interest. Defects can thus serve the purpose of a graded layer or region to which energy in the lattice can be directed for efficient conversion using the transition wave as a carrier. Three types of defects are considered: single mass [Fig. 2.5(a)] and inter-element forcing [Fig. 2.5(b)] defects, both of which are applied at 10^{th} site in this study, and a region of distributed defects [Fig. 2.5(c)], which are applied between 30^{th} and 59^{th} sites. Experimentally, mass defects are created by attaching or removing additional nonmagnetic metal parts on the defect elements [red mass in Fig. 2.5(a)], and inter-element forcing defects are generated by changing the initial lattice spacing distances around the defect [red arrows in Fig. 2.5(b)].

Figures 2.5(d) and (e) show the numerical results of the harvested energy factor as a function of the ratio between the defect and the periodic lattice value for the mass (m_{defect}/m) or lattice spacing distance (L_{defect}/L): the sharp drop toward the large spacing distance in Fig. 2.5(e) represents disintegration of the stable propagation of the transition wave. For the studied case, we observe that the lighter the mass defect, the more energy can be harvested

from the defect location as less kinetic energy is required to propagate the wave through the site. Two noticeable peaks are observed for the inter-element spacing defect. The harvested energy of the element preceding the defect (9^{th} element) exhibits a non-monotonic behaviour, showing a dip for distances below the periodic baseline with a minimum at $L_{defect}/L \approx 0.77$ and subsequently reaching the maximum at the limiting spacing value for the stable wave propagation ($L_{defect}/L \approx 1.2$). On the other hand, the harvested energy available at the element after the defect (11^{th} element) features a peak value at about $L_{defect}/L \approx 0.77$, then monotonically decreases with the spacing distance. The harvested energy factors calculated from the experimental data after normalisation (see Supplementary Information) are overlaid with error bars, showing the reasonable qualitative match with those attained from the numerical calculation.

The delivery of power over longer periods of time may be created if a larger oscillatory tail is induced. This is achieved via the introduction of a distributed defect region spanning several sites. The amplitude of the tail becomes larger with increasing mass (see Supplementary Information) or decreasing damping [Fig. 2.4(a)]. In addition, constructive interference occurs from the reflected wave at the boundary from heavy to light or from stiff to soft (equivalent to large to small inter-element forcing) region [155], which can further increases the amplitude at the boundary.

Figure 2.6(a) shows the response when $m_{defect} = 8\,m$, $L_{defect} = 0.8\,L$ and $b_{tot} = 0.2$ Ns/m are used, and the defect section is selected to be long enough [30-59^{th} sites as in Fig. 2.5(c)] to stabilise its response to the lattice-intrinsic level with the modified parameters. Near the boundary of the defect section, the local reflections generate kinks traveling in opposite directions while the global unidirectionality is preserved due to the asymmetry in the strain potential. The interplay between the reflection and the natural tendency of the lattice to travel forward produces spatially localised nonlinear oscillations with several state transitions and large amplitudes, which are the characteristics of a meta-stable breather-like mode [156] (see Supplementary Video 4 and Fig. 5).

In this example, the harvested energy at the boundary of the defect section (59^{th} site) is calculated to be 80 mJ, compared to 19 mJ in the periodic counterpart, assuming $d =$ 0.1 Ns/m is used [Fig. 2.6(b)]. Recalling the input independence property of the lattice, we

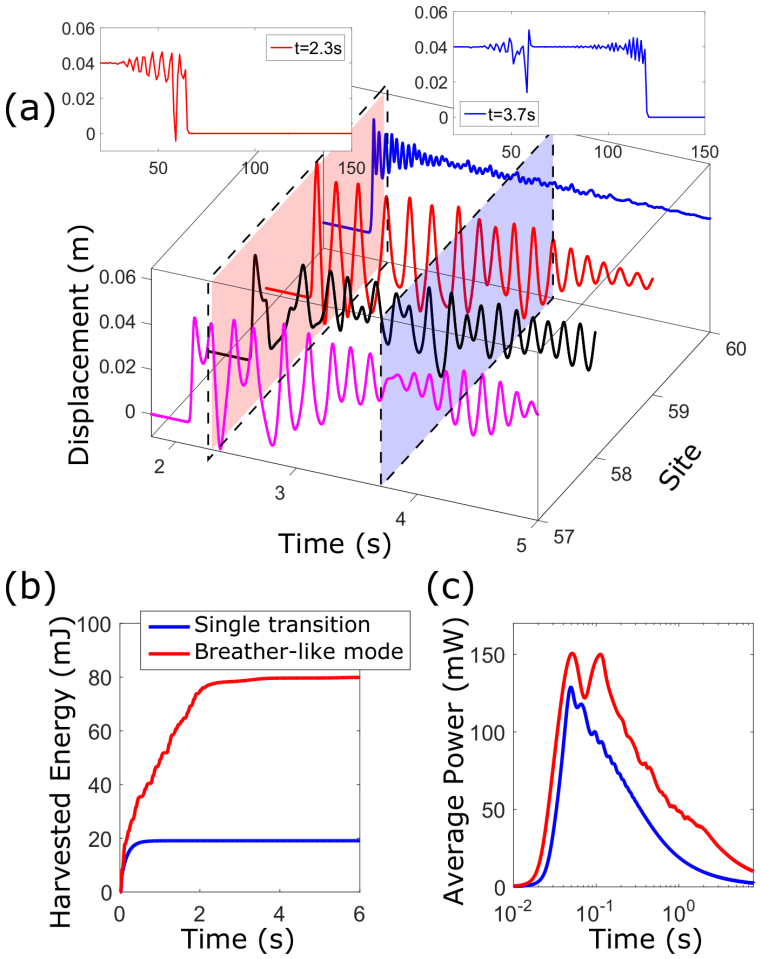

Figure 2.6. (a) Time responses of individual elements near the boundary of the defect section. In the insets are the spatial motions at t=2.3s and t=3.7s. (b),(c), Comparison of the harvested energy and average power to the periodic lattice without defects.

harvest four times more energy under the same input energy by virtue of wave localisation in the breather-like mode. The average power output shows no significant gain since its maximum value is mainly governed by the initial state transition [Fig. 2.6(c)]. However, the persistent localised transitions allow the conversion of significant power over a longer period of time in comparison with a single transition wave. For example, the second peak (150 mW at 0.113 s) occurs at about twice the period of the first peak (151 mW at 0.051 s), while the periodic counterpart experiences a significant power drop from 129 mW to 93 mW during the same time period. Therefore, substantial power output-to-input ratio improvement under cyclic excitation is achieved, rendering robust harvesting possibility.

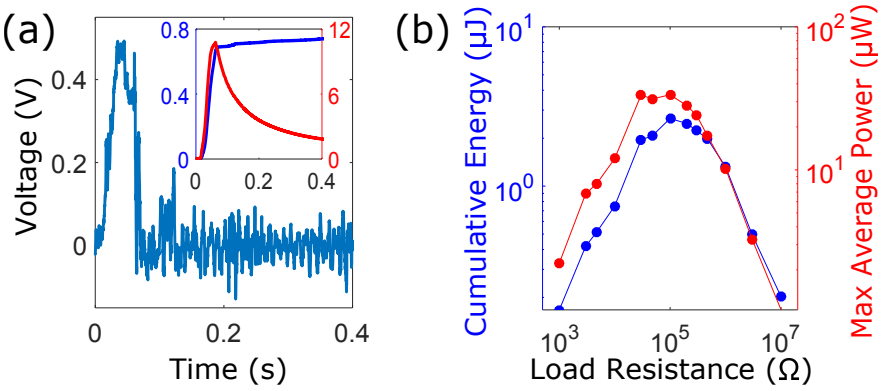

Figure 2.7. (a) Voltage response with 10 $k\Omega$ resistor and the associated cumulative energy (in blue) and average power (in red) in the inset. (b) Resistance sweep of the maximum cumulative energy (in blue) and maximum average power (in red).

2.7 Experimental Implementation

The lattice characteristics for energy harvesting are demonstrated using piezoelectric transducers, bonded to the bistable element at the 10^{th} site. The voltage responses are obtained by using the simplest resistive circuit. Following Ref. [135], the cumulative energy and the average power are used as performance measures due to the transient nature of the unit cell dynamic response: the cumulative energy is calculated from the time integral of the power V^2/R over the entire time span, and the average power is obtained by dividing the cumulative energy by the time measured from the onset of the motion.

Figure 2.7(a) shows the voltage response of the transduction unit cell for a resistance value of 10 $k\Omega$. The attachment of a piezoelectric transducer substantially increases the exhibited damping from b to $b^* + d$. As a result, the induced vibratory motion on the unit cell is highly damped and most of the harvested energy arises from the state transition. The inset shows the cumulative energy and the average power harvested at the transduction unit cell as a transition wave propagates through the cell. Even at this distant location from the boundary, substantial energy can be harvested. These results are improved further as revealed from the resistor sweep shown in Fig. 2.7(b). For the baseline values of the experimental lattice, both the cumulative energy and the maximum average power harvested measures are maximised for a value of 100 $k\Omega$, reaching peak values of 2.8 μJ and 32 μW, respectively.

2.8 Conclusion

We demonstrate that the nonlinear dynamics of a 1D lattice of bistable elements can be utilised to inherently generate invariant energy harvesting capabilities from transition waves. The stored energy from the topological strain difference allows bistable lattices to act as mechanical capacitors, where the fed energy can be harvested during the release process in the form of wave energy transmission. The lattice dynamics are further manipulated through defect inclusions resulting in the onset of breather-like modes, revealing a mechanism for delivering the stored energy over extended time periods. The input-independent dynamics, extreme directionality and topological energy harvesting characteristics of the presented system allow for producing protective metastructures that concurrently redirect and harvest surplus energy when subject to disruptive events, such as blasts, Tsunamis, or earthquakes. The proposed metastructures thus provide an ideal implementation for protecting critical systems and infrastructure, while providing an intrinsic source for local power to maintain continued operation after natural or man-made disasters.

2.9 Materials and Methods

2.9.1 Lattice Preparation

Each unit cell comprised a bistable element with a set of grade N42 neodymium magnets (Supermagnete R-19-09-06-N) attached at the center. The unit cells were arranged along the rail on an optical table in a way to exert repulsive forces between themselves, forming a lattice under uniform inter-element forces. The same force-deflection relations from the previous study [69] were used for the on-site element and the magnet (Supplementary Fig. 1); the data points were obtained in a series of quasi-static compression tests and fitted in a polynomial form and a exponential form, respectively for the bistable element and the magnet. A more detailed measurement procedure can be found in Ref. [69] and the references therein.

2.9.2 Experimental Data Acquisition

A random black and white speckled pattern was printed on a thin sticky paper and attached on the top edge of each of the bistable elements (Supplementary Fig. 6). The input excitation was triggered through repulsive magnetic force applied by pulling and releasing the elastic translating mount at the first element, and the resulting motions were captured by a set of two high-speed cameras (Photron UX100) with DSLR lenses (NIKKOR 24-85mm f/2.8-4D IF) at 1000 fps sampling rate. A commercial digital image correlation software (VIC-3D) was used for post-processing, and the displacement of each element was measured at the point closest to the center of the element (bottom of the speckled pattern) to minimise any rotational contribution. Since the snapping distances vary between elements due to the manufacturing deviation, the measured responses were adjusted for uniform comparison with those of numerical results. The details of the data adjustment can be found in Supplementary Information.

2.9.3 Voltage Response

In this study, piezoelectric transducers (MIDE qp-16n) were used as the power conversion mechanisms to convert the induced strains into electrical currents. Two such transducers were glued near the roots (where the strains of the fundamental mode shape are the largest) of the bistable element with epoxy (Loctite E-120hp) and cured for 48 hours at room temperature (Supplementary Fig. 6). To obtain the voltage response, the piezoelectric elements were connected in parallel so that their electrical outputs combine constructively at the junction, and then a closed circuit was formed by connecting a resistor. The voltage difference across the resistor was measured through dSpace data acquisition system (DS1104) with 16-bit resolution. Various resistors with different resistance values and series connections of several resistors were used for the resistance sweep.

2.10 Acknowledgments

M. Hwang and A. F. Arrieta gratefully acknowledge the support of the Purdue Research Foundation (PRF); this research was supported through start-up funds provided to Prof. A. F. Arrieta.

3. ENERGY HARVESTING CHARACTERISTICS IN METAMATERIALS BASED ON BISTABLE LATTICES

Myungwon Hwang, Andres F. Arrieta

This chapter is published in:
Proc. SPIE, 2019.
DOI: 10.1117/12.2514426

3.1 Abstract

In this study, an energy harvesting strategy that utilizes the input-independent, invariant transition waves in periodic lattices of bistable elements is explored. We observe that oscillatory tails are induced in a discrete array as transition waves propagate along the lattice. The generated tail at each unit cell vibrates predominantly at a single frequency, which indicates that the tail energy can be efficiently harvested through resonant transduction mechanisms. We introduce inertially and elastically equivalent lattice models to study the discreteness effect of the bistable lattice on the characteristic behaviors of the oscillatory tails and observe that the energy harvesting potential from transition waves can be significantly increased with growing discreteness.

3.2 Introduction

The design of mechanical metamaterials for the control of wave propagation has attracted substantial attention in the past two decades [48, 157–160]. Typically, such metamaterials are designed to produce unconventional characteristics such as extreme wave guiding [69, 70], super-lensing [102, 161–165] and broadband energy harvesting [76, 77, 89, 91–94, 96, 145]. Two main phenomena have been exploited to achieve these unconventional properties: scattering [4] and local resonance [2]. However, both mechanisms exhibit performance limitations in the low acoustic (0.4-1 kHz) and structural ($\ll$0.4 kHz) frequency ranges due to their fundamental reliance on the characteristic frequencies of the unit cells. Although unit cells can be theoretically tuned to any operating frequencies, the mismatch between the

required inertial property and geometrical feature size limits the ability to obtain the desired dynamical properties at such low frequencies. Utilization of nonlinear lattices to create metamaterials with ultra-low and ultra-wide band of operations have been proposed [166, 167]; however, their potential is yet to be fully uncovered. This is particularly relevant for the design of metamaterials capable of harvesting at the low structural frequency range.

Among these nonlinear metamaterials, lattices composed of bistable unit cells [48, 69, 70] are of a particular interest due to their ability to transmit a transition waves, which is a type of topological solitons [31, 45]. Our recent studies [97, 168] on such bistable lattices with asymmetric on-site potentials have shown weak dependence of transition waves on the input frequency that encompass very low frequency and even the quasi-static regime, thus suggesting the possibility of low-frequency energy harvesting. However, the specific strategy on how such highly concentrated traveling energy can be harvested has not been fully discussed. In this manuscript, we present a specific method to harvest energy from transition waves. In our framework, the lattice's energy harvesting capability is an intrinsic property that is supplementary to its primary functions such as high-fidelity wave guiding. Consequently, we focus on the radiated vibrations (phonons) of the transition wave, which dissipates within the lattice like typical linear waves in physical settings. This radiation of energy exists due to the inherent discreteness of the lattice structures, and we seek a strategy to amplify its contribution and to efficiently convert its energy while still allowing the transmission of transition waves. To that end, a set of equivalent lattice models that keep the same macroscopic inertial and elastic properties but with varying degree of lattice discreteness are presented, and their potentials to harvest energy are compared.

3.3 Bistable Lattices

A periodic lattice composed of bistable unit cells with asymmetric on-site potentials is implemented in this study [69, 97]. Figure 3.2(b) shows a schematic representation of the lattice, and the governing equation can be readily written as

$$mu_{n,tt} = k(u_{n-1} - 2u_n + u_{n+1}) - \mathcal{F}(u_n) - du_{n,t}\,, \tag{3.1}$$

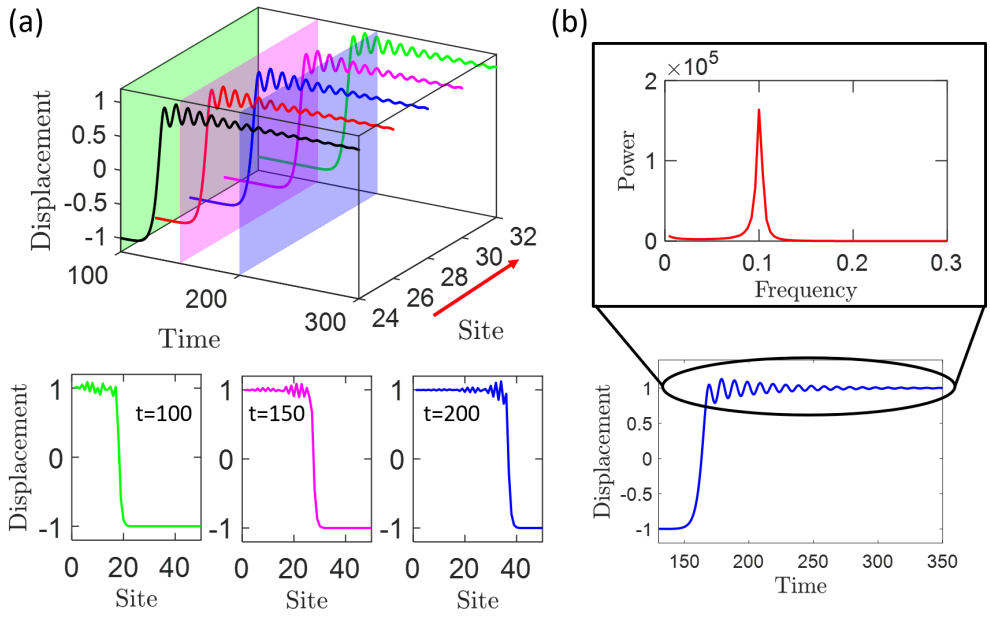

Figure 3.1. (a) Transition wave propagation in a bistable lattice with asymmetric on-site potentials. 2D plots show the time progression of wavefront in space configuration. (b) Power spectrum of the oscillatory tail contribution.

where u_n=$u_n(t)$ is the displacement of the mass at n^{th} site from its equilibrium position, m is the unit cell mass, k is the linear intersite spring stiffness, $F(u_n)$ is the on-site force due to the bistable element, and d is velocity-dependent damping coefficient. Although not shown explicitly in the governing equation, L is the lattice spacing distance between neighboring unit cells. The on-site force for a bistable element can be represented in many different ways, but one general representation is $\mathcal{F}(u_n) = \omega_0^2(\frac{u_n}{u_0} - 1)(\frac{u_n}{u_0} + 1)(\frac{u_n}{u_0} - \mathrm{e})$, where ω_0^2 controls the stiffness of the bistable element, $\pm u_0$ are the two stable equilibria, and $\mathrm{e}u_0$ is the unstable equilibrium which also indicates the degree of asymmetry between two stable states.

A closed-form solution is not available for Eq. (3.1). Instead, a numerical approach is taken to obtain the responses in the lattice. A central finite difference method [169] with a constant time step Δt=0.01 is applied to the governing equation, and a typical response in this lattice is shown Fig. 3.1(b). Although unphysical, the following simple baseline lattice parameters in a consistent unit system are used for qualitative analyses: L=4, m=4, k=0.25, ω_0^2=0.06, e=0.3. The governing equation is not nondimensionalized on purpose to facilitate the numerical comparison among macroscopically equivalent lattice models to

follow in Sec. 3.4. The 2-D plots in Fig. 3.1(a) show the still images of the unit cells in a space configuration taken at different instants of time, and the propagation of a transition wave from left to right can be clearly identified.

Different from the soliton solutions from continuous Sine-Gordon (or more general Klein-Gordon) equations, the inherent lumpiness of the lattice system induces a trailing vibration, or an oscillatory tail, as a result of a snap-through transition from one stable state to another stable state. Taking the power spectrum on the oscillatory tail only, it can be seen that the tail is dominantly vibrating at a single frequency [Fig. 3.1(b)]. As proved in the previous studies [97], the asymmetric on-site potentials allows invariant responses, and hence the tail frequencies are the same at every site sufficiently away from the lattice boundary.

The highly kinetic motion of the induced vibrations can be regarded as heat generated in the lattice. From a material point of view, it can be regarded as absorbed energy by the lattice, and this energy may be efficiently harvested through resonant transductions such as piezoelectric or electromagnetic conversions. In other words, transmission of transition waves can be an effective means to convert energy for powering small infrastructures while serving its primary functions (such as a robust transmission line and a mechanical diode), enabling energy harvesting an inherent material property. Maximizing the kinetic energy in the oscillatory tail from transition waves will be a key to increase the harvesting performance of such metamaterials.

3.4 Discreteness Effect

To see the discreteness effect without altering the macroscopic properties of the lattice, the lattice parameters are changed such that mass density and energy densities remain constant [69]. This creates a set of inertially and elastically equivalent lattices, where purely the effect of the lattice discreteness can be analyzed. Figure 3.2 schematically shows three example lattices whose composition becomes more discrete in order. As the lattice spacing distance increases, the mass of each unit cell should increase to keep the same mass density, the intersite spring stiffness should decrease, and on-site stiffness should increase to keep the globally equivalent elastic property – the decrease of intersite stiffness and increase of on-site stiffness can be considered as a series and a parallel connection of springs, respectively. The

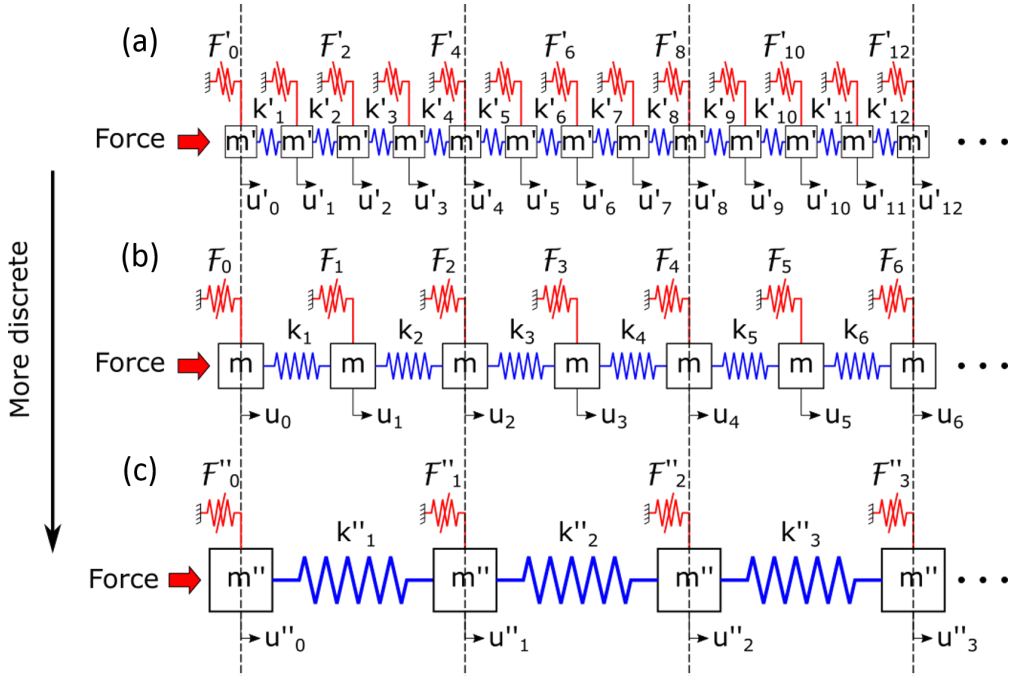

Figure 3.2. Schematic representation of macroscopically equivalent lattices. The lattice becomes more sparse as it goes from (a) to (c), indicating increased discreteness. The vertical dashed lines show the globally equivalent sites.

general conversion relations for the unit cell parameters between new and original lattice spacings are summarized as follows:

$$\begin{aligned}
\text{Mass density:} \quad & \frac{m}{L} = \frac{m}{L} \Rightarrow m = m\frac{L}{L} = rm, \\
\text{Intersite energy density:} \quad & \frac{\frac{1}{2}k(\epsilon L)^2}{L} = \frac{\frac{1}{2}k(\epsilon L)^2}{L} \Rightarrow k = k\frac{L}{L} = \frac{k}{r}, \\
\text{Onsite energy density:} \quad & \frac{\phi(u_n)}{L} = \frac{\phi(u_n)}{L} \Rightarrow \phi = \phi\frac{L}{L} = r\phi, \\
\text{Dissipated energy density:} \quad & \frac{\frac{1}{2}du_{n,t}^2}{L} = \frac{\frac{1}{2}du_{n,t}^2}{L} \Rightarrow d = d\frac{L}{L} = rd,
\end{aligned} \tag{3.2}$$

where the primed quantities represent those of the changed lattice spacing, and r is the ratio between the changed and original lattice spacing distances.

To compare the macroscopic behaviors of the lattices, the responses are compared at several globally equivalent sites (the vertical dashed lines in Fig. 3.2); for example, $u_2^{(L=8)}$, $u_4^{(L=4)}$, $u_8^{(L=2)}$ and $u_{16}^{(L=1)}$ are globally equivalent sites. Figures 3.3(a-e) show the responses of the lattices for various lattice spacing distances (equivalently, for various discreteness levels).

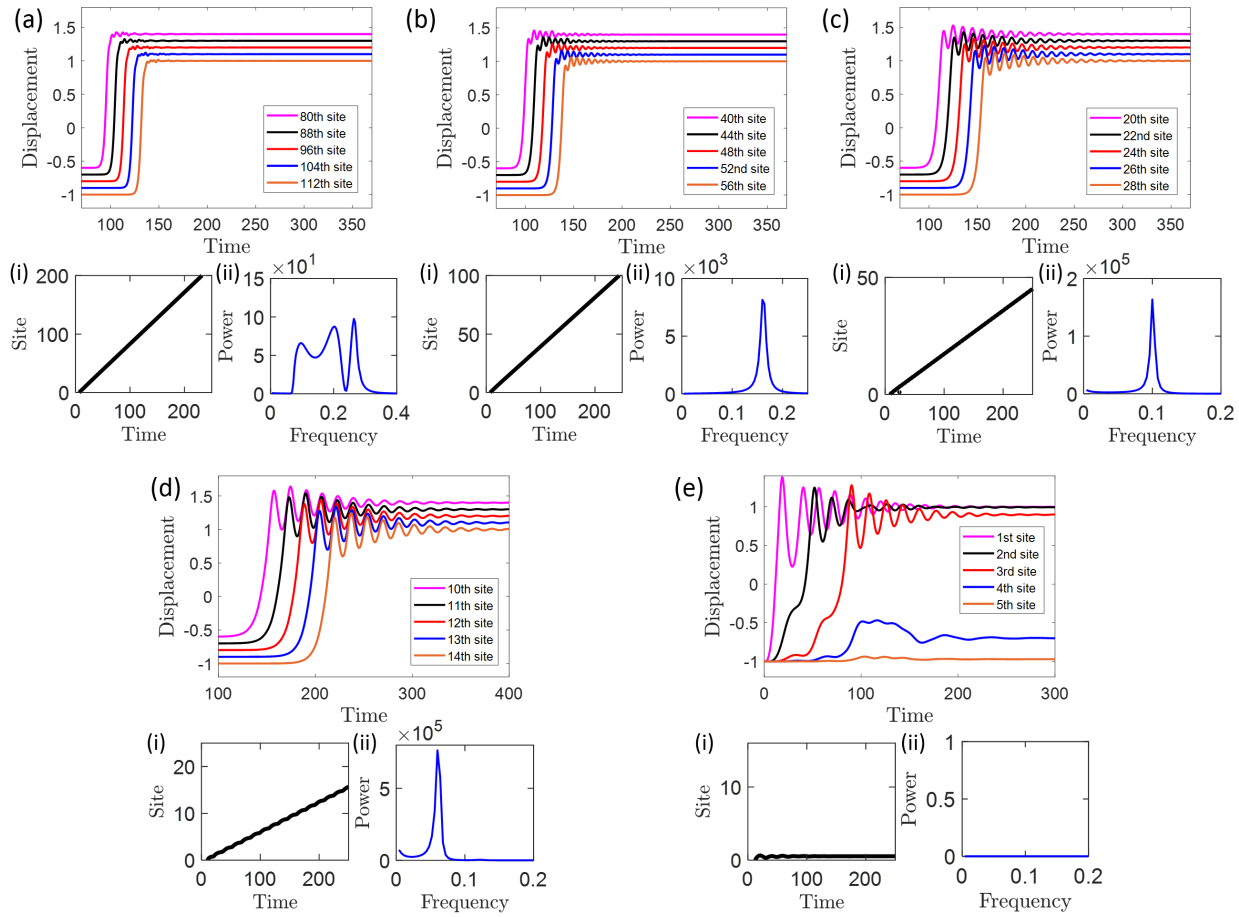

Figure 3.3. The time responses of the individual unit cells at globally equivalent sites for (a) L=1, (b) L=2, (c) L=4, (d) L=8, and (e) L=10.4. Also shown are (i) the corresponding space-time contour of the transition wave and (ii) power spectrum of the oscillatory tail. For (a-d), each individual response is displaced by 0.1 unit from the next one for visualization purpose.

At L=1, the induced vibrations after state transitions almost vanish. This result is expected since the lattice becomes a continuum in the limit $L \to 0$, at which we have the pure soliton solutions (in the form of $\tanh \frac{x-vt}{\sqrt{2}\sqrt{1-v^2}}$) predicted by the continuous Klein-Gordon equations with ϕ-4 potential [45]. On the contrary, as the discreteness gradually increases to L=8, there is a distinguishable amplification of the tail motion. The peak-to-peak amplitudes for the lattices with the selected lattice spacings are compared in Tab. 3.1. The values show the general trend of increasing amplitude. However, the oscillatory tail does not grow indefinitely. For a given amount of input excitation, there exists a critical value of the lattice spacing distance where the radiated energy through the oscillatory tails become too high to

Table 3.1. Summary of the peak-to-peak amplitude $A_{\text{p-p}}$ of the oscillatory tails and propagation speeds v_{prop} of the transition waves for different lattice spacing distances.

L	1	2	4	8	10	12
$A_{\text{p-p}}$	0.0474	0.130	0.340	0.644	0.722	0
v_{prop}	0.885	0.839	0.741	0.5102	0.3376	0

allow the propagation of the transition waves, similar to Peierls-Nabarro barrier observed in dislocation theory [156].

The insets of each response plot illustrate the space-time contour of the transition wave and the power spectrum of the oscillatory tail. The contour is drawn by tracking the zero crossings of the displacement at each site, and the slope of the contour indicates the propagation speed of the transition wave. As shown in Tab. 3.1, the propagation speed monotonically decreases with increasing discreteness. This is expected since more of the available energy is redistributed to generate a larger tail motion, thereby reducing the transport energy of the transition wave. The power spectrum confirms that the tail vibrates at a single dominant frequency even with changing lattice discreteness for a sufficiently large tail amplitude (greater than $\sim$2% of the snap-through distance).

The ability to harvest more energy from amplified tail motion comes with price that the main transition wave becomes less localized in physical space, which makes the transition wave more susceptible to external disturbances. Since the inherent power conversion property is lost with interrupted propagation of transition waves, and the harvesting capability is supplementary to the lattices' primary functions, a compromise between the extreme transport property and power conversion performance needs to be made.

3.5 Conclusions

We have investigated an energy harvesting strategy that can utilize input-independent, invariant transition waves in periodic lattices of bistable elements with asymmetric on-site potentials. The inherent discreteness at the unit-cell level generates trailing vibrations as snap-through transitions from one states to the other states are triggered. The emergence of

the oscillatory tails does not alter the lattice's ability to transmit solitary waves but radiates kinetic energy (heat) out of the lattice system. Since the tail vibration is mainly at a single dominant frequency, the kinetic energy of the tail can be efficiently harvested through resonant energy conversion mechanisms. Introducing inertially and elastically equivalent lattices that only differ in the level of lattice discreteness, we have observed that the tail motion and so the associated kinetic energy can be greatly amplified with a growing discreteness until reaching the critical point blocking the transmission of transition waves. This result suggests that higher discreteness in the lattice promotes more efficient energy harvesting.

Although the investigated periodic lattice has shown good potential as a robust waveguide with inherent energy harvesting capability, its functional effectiveness is rather limited. The high directionality of the lattice arising from the asymmetric on-site potentials allows only compressive transition waves (anti-kink), which would require integration of additional mechanisms for useful real-world applications. In our recent study [170], we have theoretically and experimentally proved that both kink and anti-kink solitons can be transmitted in the lattices with graded properties, thereby enabling continued excitations of transition waves from a single excitation site. An extended investigation will follow on the functionally graded lattices. Also, electromechanical coupling effects are not considered in this simplified harvesting performance analyses that use the tail energy only. In the future study, the actual piezoelectric model will be incorporated into the mechanical model for a more accurate assessment on the harvested capability.

3.6 Acknowledgments

M. Hwang and A. F. Arrieta gratefully acknowledge the support of the Purdue Research Foundation (PRF); this research was partly funded through start-up funds provided by Prof. A. F. Arrieta.

4. SOLITARY WAVES IN BISTABLE LATTICES WITH STIFFNESS GRADING: AUGMENTING PROPAGATION CONTROL

Myungwon Hwang, Andres F. Arrieta

This chapter is published in:
Physical Review E, 2018, 08, 042205.
DOI: 10.1103/PhysRevE.98.042205
Supplementary Information is attached as Appendix B.

4.1 Abstract

In this study, we introduce small perturbations in the forms of graded inter-site stiffnesses and graded on-site potentials to a lattice composed of bistable unit cells under elastic interactions. Based on a known soliton solution in the ϕ-4 model, we use a perturbation approach to approximate the effects of the perturbations on the propagation speeds of transition waves. Numerical validations follow on the exact discrete equations of motion, from which we observe eventual stoppage of transition waves in the periodic lattice under physical damping, unidirectional propagation of the waves in the direction of softening properties, and boomerang-like reflection of the waves in the stiffening direction. Finally, we present 3D-printed experimental lattices, confirming the theoretical and numerical results. The observed behaviors imply the extreme controllability of solitary waves through slight engineering manipulations in material-level structures. We further find that both kink (rarefaction) and anti-kink (compression) waves are allowed at any site in the lattice, extending the functionality of the lattice in engineering applications such as energy harvesting.

4.2 Introduction

The utilization of nonlinearities in lattice systems has been the focus of substantial research due to its potential to generate classes of solitary waves [31, 33, 45], which are large-amplitude, spatially localized waves exhibiting more robust transport properties than their

linear counterparts. In the context of uniform periodic lattices, a considerable number of theoretical and numerical groundworks have been laid on the dynamics and formations of such nonlinear waves, encompassing topological/non-topological solitons, envelope solitons, and breathers [36–38, 48, 156, 171–176]. To bridge gap between the idealization and physical reality, where no materials are perfect, and thus the effects of relaxed periodicity on the solitary waves are of physical importance, a series of studies on perturbed systems has followed. In particular, inhomogeneities in the forms of external force, boundaries, dissipation, substrate or mass impurities, and stochastic or harmonic variations in additive and/or multiplicative terms have been extensively analyzed in both sine-Gordon [109–111, 113, 177] and ϕ-4 [114–117] models. However, the dynamics of lattices supporting strongly nonlinear waves under the presence of graded properties have not received much attention.

In spite of the well-established theoretical and numerical studies on solitary waves, their experimental manifestations are still rare. The major experimental advances have been made in the observations and utilizations of non-topological solitary waves arising from the strong Hertzian contact forces in granular chains [65, 66, 165, 178–183]. However, the experimental demonstration of topological solitary waves had long been limited to the classical pendula model [32]. Recently, stable propagation of topological solitary waves, or state transition waves, has been successfully demonstrated in a chain of repelling magnets [184] and in a periodic lattice formed by bistable unit cells [67, 68] under magnetic interactions [69]. The latter results in extreme unidirectional wave guiding and has been further observed that its response is independent of the type and intensity of the input excitations, which suggests its potential implementation for broadband energy harvesting and protective metamaterials [97]. In an elastically-connected periodic bistable lattice made of highly dissipative soft media, Ref. [70] have also demonstrated similar transition waves for high-fidelity, controllable signal transmission. For uninterrupted propagation of transition waves, both types of bistable lattices in the previous studies utilize the stored energy between asymmetric on-site potential wells in periodic arrangements to balance out the inherent dissipation. This choice destroys one of the two soliton solutions (kink and anti-kink), limiting their functionalities in that no intrinsic repositioning mechanism is available.

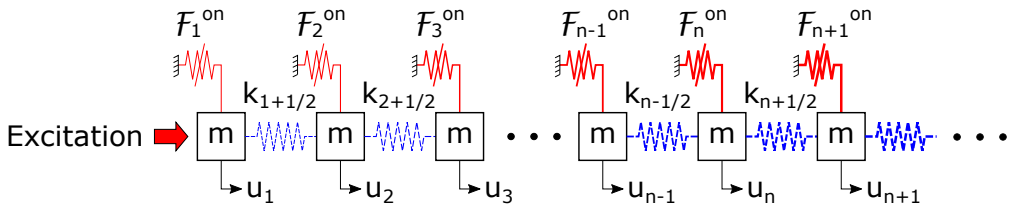

Figure 4.1. A schematic representation of the bistable lattice with elastic inter-site interactions. A unit cell is composed of a mass and an on-site bistable element (in solid red), and each unit cell is coupled with the neighboring cell by inter-site linear springs (in dashed blue). Both the inter-site and on-site elements are allowed to vary in stiffnesses.

In this manuscript, we study the dynamics of lattices of symmetric bistable elements exhibiting spatially varying properties, investigating the effects of the grading on the propagation characteristics of transition waves. To that end, we begin with linear perturbation from the known soliton solutions of the ϕ-4 model to find the approximate propagation speeds of the solitons for each case. The numerical simulations on the exact equations of motion follow to validate the theoretical predictions, and finally, we present 3D-printed lattice samples demonstrating all of the predicted behaviors in physical settings. We show that the introduction of spatial grading allows for this class of lattices to support compression and rarefaction topological solitons in contrast to periodic arrangements, thereby providing an intrinsic mechanism for resetting the states of all the elements in the arrangement. The existence of the two possible topological soliton solutions allows for the exciting nonlinear dynamics of bistable lattices to be exploited in important applications, as in energy harvesting or soft robotics.

4.3 Lattice Description

A simple one-dimensional chain of spring-mass system is used to represent the lattice model. Each unit cell is composed of a bistable element (depicted in solid red lines in Fig. 4.1) with a mass that is connected to the nearest neighbors by linear springs (in dashed blue lines in Fig. 4.1). The governing equation of motion can be written as:

$$mu_{n,tt} = k_{n+\frac{1}{2}}(u_{n+1} - u_n) - k_{n-\frac{1}{2}}(u_n - u_{n-1}) + \mathcal{F}_n^{on}(u_n) - du_{n,t}\,, \tag{4.1}$$

where u_n and $\mathcal{F}_n^{on}$ represent the displacement and on-site force of the n^{th} element, and $k_{n-\frac{1}{2}}$ and $k_{n+\frac{1}{2}}$ are spring stiffnesses to the left and right of the element. The mass m and on-site damping d remain invariant through the lattice. The masses are separated from one another by a constant lattice spacing L, although it does not explicitly appear in the equation.

For a more compact mathematical treatment, the governing equation is nondimensionalized to

$$\bar{u}_{n,\bar{t}\bar{t}} = \bar{k}_{n+\frac{1}{2}}(\bar{u}_{n+1} - \bar{u}_n) - \bar{k}_{n-\frac{1}{2}}(\bar{u}_n - \bar{u}_{n-1}) + \bar{\mathcal{F}}_n^{on}(\bar{u}_n) - \bar{d}\bar{u}_{n,\bar{t}}\,, \tag{4.2}$$

where the following nondimensionalization is used:

$$u_n = L\bar{u}_n, \quad t = \tau\bar{t}, \quad \tau = \sqrt{\frac{m}{k_1}}, \quad \bar{k}_n = \frac{k_n}{k_1}, \quad \bar{d} = \frac{d}{m}\tau, \quad \bar{\mathcal{F}}_n^{on} = \frac{\mathcal{F}_n^{on}}{k_1 L}. \tag{4.3}$$

This discrete equation is in general difficult to solve exactly, and thus we seek a continuum-limit model for an approximate solution. Expanding $\bar{u}_{n\pm1}(\bar{t}) = \bar{u}(\bar{x}\pm1,\bar{t}) = \bar{u}(\bar{x},\bar{t}) \pm \frac{\partial\bar{u}(\bar{x},\bar{t})}{\partial\bar{x}} + \frac{1}{2}\frac{\partial^2\bar{u}(\bar{x},\bar{t})}{\partial\bar{x}^2}$, $\bar{k}_{n\pm\frac{1}{2}} = \bar{k}(\bar{x}\pm\frac{1}{2}) = \bar{k}(\bar{x}) \pm \frac{1}{2}\frac{\partial\bar{k}}{\partial\bar{x}} + \frac{1}{8}\frac{\partial^2\bar{k}}{\partial\bar{x}^2}$ and letting L approach 0, we obtain:

$$\frac{\partial^2\bar{u}(\bar{x},\bar{t})}{\partial\bar{t}^2} - \bar{k}(\bar{x})\frac{\partial^2\bar{u}(\bar{x},\bar{t})}{\partial\bar{x}^2} - \frac{\partial\bar{k}(\bar{x})}{\partial\bar{x}}\frac{\partial\bar{u}(\bar{x},\bar{t})}{\partial\bar{x}} - \bar{\mathcal{F}}^{on}(\bar{u},\bar{x}) + \bar{d}\frac{\partial\bar{u}(\bar{x},\bar{t})}{\partial\bar{t}} = 0. \tag{4.4}$$

The on-site force $\bar{\mathcal{F}}^{on}(\bar{u},\bar{x})$ should represent bistability of each unit cell, providing a necessary condition for the generation of transition waves. The lowest polynomial that can represent the bistability of the on-site force is a cubic function (referred to as ϕ-4 potential in most literature); one such expression for a symmetric on-site potential is $\omega_0^2(\bar{u} - \bar{u}^3/u_0^2)$, where ω_0 and u_0 are arbitrary constants. By letting $a(\bar{x})$ and $b(\bar{x})$ be small perturbations from the reference stiffness $\bar{k}_1$ and the reference on-site force $\bar{\mathcal{F}}^{on}(\bar{u},0)$ such that $\bar{k}(\bar{x}) = 1 + a(\bar{x})$ and $\bar{\mathcal{F}}^{on}(\bar{u},\bar{x}) = [1 + b(\bar{x})]\omega_0^2(\bar{u} - \bar{u}^3/u_0^2)$, respectively, the final equation can be written without loss of generality as:

$$\frac{\partial^2\bar{u}}{\partial\bar{t}^2} - [1 + a(\bar{x})]\frac{\partial^2\bar{u}}{\partial\bar{x}^2} - \frac{\partial a(\bar{x})}{\partial\bar{x}}\frac{\partial\bar{u}}{\partial\bar{x}} - [1 + b(\bar{x})]\omega_0^2(\bar{u} - \bar{u}^3/u_0^2) + \bar{d}\frac{\partial\bar{u}}{\partial\bar{t}} = 0. \tag{4.5}$$

By setting $X = \omega_0 \bar{x}$, $T = \omega_0 \bar{t}$, $\bar{u} = u_0 F$, $a(\bar{x}) = \alpha(X)$, $b(\bar{x}) = \beta(X)$, and $\bar{d} = \omega_0 \delta$, Eq. (4.5) can further be reduced into a canonical form

$$F_{,TT} - [1 + \alpha(X)]F_{,XX} - \alpha(X)F_{,X} + [1 + \beta(X)](F^3 - F) + \delta F_{,T} = 0. \tag{4.6}$$

4.4 Theoretical Analyses

The exact solution to Eq. (4.6) is not known, and so we seek a perturbed solution from a known soliton solution in the periodic lattice without any perturbations: $\alpha(X), \beta(X), \delta = 0$. Applying a Lorentz transformation,

$$\begin{aligned} \xi = \gamma(X - vT), \quad \tau = \gamma(T - vX), \quad \gamma = \frac{1}{\sqrt{1 - v^2}}, \\ X = \gamma(\xi + v\tau), \quad T = \gamma(\tau + v\xi), \end{aligned} \tag{4.7}$$

Eq. (4.6) becomes

$$\begin{aligned} [1 - \alpha(X)\gamma^2 v^2]F_{,\tau\tau} + 2v\alpha(X)\gamma^2 F_{,\tau\xi} - [1 + \alpha(X)\gamma^2]F_{,\xi\xi} + \gamma[\alpha(X)v + \delta]F_{,\tau} \\ - \gamma[\alpha(X) + \delta v]F_{,\xi} + [1 + \beta(X)](F^3 - F) = 0. \end{aligned} \tag{4.8}$$

Since the unperturbed equation is invariant under Lorentz transformation and the velocity v is a free parameter, we can work with a static soliton in a moving frame traveling to $+\xi$ direction (to the right) with v. In the physical frame, the soliton itself can be considered to travel to the right.

Assuming a perturbed solution $F(\xi, \tau) = F_s(\xi, \tau) + f(\xi, \tau)$, where $F_s(\xi, \tau)$ is the soliton solution of the equation

$$F_{s,\tau\tau} - F_{s,\xi\xi} + F_s^3 - F_s = 0, \tag{4.9}$$

Eq. (4.8) becomes

$$\begin{aligned} [1 - \alpha(X)\gamma^2 v^2](F_{s,\tau\tau} + f_{,\tau\tau}) + 2v\alpha(X)\gamma^2(F_{s,\tau\xi} + f_{,\tau\xi}) - [1 + \alpha(X)\gamma^2](F_{s,\xi\xi} + f_{,\xi\xi}) \\ + \gamma[\alpha(X)v + \delta](F_{s,\tau} + f_{,\tau}) - \gamma[\alpha(X) + \delta v](F_{s,\xi} + f_{,\xi}) \\ + [1 + \beta(X)](F_s^3 + 3F_s^2 f + 3F_s f^2 + f^3 - F_s - f) = 0. \end{aligned} \tag{4.10}$$

Subtracting the unperturbed equation of motion [Eq. (4.9)] from Eq. (4.10) and substituting the known solution $F_s(\xi,\tau) = \tanh\frac{\xi}{\sqrt{2}}$ (kink soliton), we obtain

$$\begin{aligned}
&[1-\alpha(X)\gamma^2v^2]f_{,\tau\tau} + 2v\alpha(X)\gamma^2 f_{,\tau\xi} - [1+\alpha(X)\gamma^2]f_{,\xi\xi} + \gamma[\alpha(X)v+\delta]f_{,\tau} \\
&-\gamma[\alpha(X)+\delta v]f_{,\xi} + [1+\beta(X)](2-3\,\mathrm{sech}^2\frac{\xi}{\sqrt{2}})f + \alpha(X)\gamma^2\,\mathrm{sech}^2\frac{\xi}{\sqrt{2}}\tanh\frac{\xi}{\sqrt{2}} \\
&-\frac{1}{\sqrt{2}}\gamma[\alpha(X)+\delta v]\,\mathrm{sech}^2\frac{\xi}{\sqrt{2}} - \beta(X)\,\mathrm{sech}^2\frac{\xi}{\sqrt{2}}\tanh\frac{\xi}{\sqrt{2}} = 0,
\end{aligned} \tag{4.11}$$

where only up to the linear terms of the small perturbation $f(\xi,\tau)$ are retained. Note that $F_{s,\tau} = F_{s,\tau\tau} = 0$ since the selected soliton solution is static in the transformed coordinate.

The ϕ-4 soliton has a known set of two bound states (ψ_b and ψ_1) and scattering states (ψ_k), which form a complete set [45]. Therefore,

$$f(\xi,\tau) = \frac{1}{c_b}\phi_b(\tau)\psi_b(\xi) + \frac{1}{c_1}\phi_1(\tau)\psi_1(\xi) + \int \phi_k(\tau)\psi_k(\xi)dk, \tag{4.12}$$

where

$$\begin{aligned}
\int_{-\infty}^{+\infty} d\xi\,\psi_b^*(\xi)\psi_b(\xi) &= \frac{1}{2}\int_{-\infty}^{+\infty} d\xi\ \mathrm{sech}^4\frac{\xi}{\sqrt{2}} = c_b, \\
\int_{-\infty}^{+\infty} d\xi\,\psi_1^*(\xi)\psi_1(\xi) &= \frac{1}{2^{3/2}}\int_{-\infty}^{+\infty} d\xi\ \tanh^2\frac{\xi}{\sqrt{2}}\,\mathrm{sech}^2\frac{\xi}{\sqrt{2}} = c_1, \\
\int_{-\infty}^{+\infty} d\xi\,\psi_k^*(\xi)\psi_k(\xi) &= \underbrace{\delta(k-k)}_{\text{dirac delta function}}.
\end{aligned} \tag{4.13}$$

Since we are interested in the translation mode ψ_b of the soliton, we project Eq. (4.11) onto ϕ_b, the details of which are provided in Supplemental Material[1]. Assuming linear [$\alpha(X) = \tilde{\alpha}X$, $\beta(X) = \tilde{\beta}X$] and small ($\tilde{\alpha},\tilde{\beta} \ll 1$) variations in the perturbations, low propagation speed ($v \ll 1$), and weak coupling between different modes for a qualitative analysis, Eq. (4.11) becomes

$$\phi_{b,\tau\tau} + \gamma\delta\phi_{b,\tau} = -\frac{1}{2}\gamma^3\tilde{\alpha}c_b + \gamma\tilde{\alpha}c_b + \gamma\delta v c_b + \frac{1}{2}\gamma\tilde{\beta}c_b. \tag{4.14}$$

[1]See Supplemental Material for each term-by-term projection

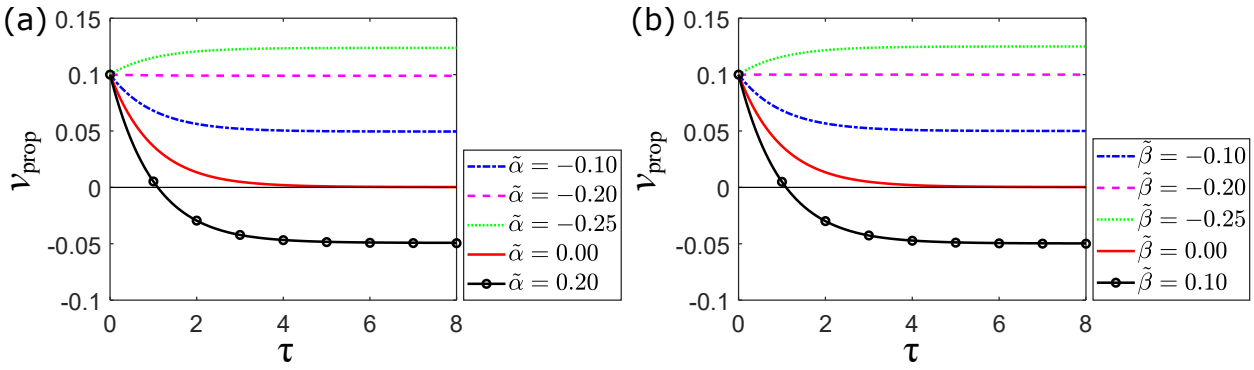

Figure 4.2. The theoretical prediction of the propagation speed of the soliton for (a) the inter-site stiffness variation $\tilde{\alpha}$ and (b) the on-site stiffness variation $\tilde{\beta}$. The same damping value $\delta = 1$ is used for every plot.

This is a second-order ordinary differential equation, and its solution yields:

$$\phi_b(\tau) = \frac{c_b[(2-\gamma^2)\tilde{\alpha} + \tilde{\beta} + 2v\delta]}{2\delta}\left[\tau + \frac{e^{-\gamma\delta\tau} - 1}{\gamma\delta}\right]. \tag{4.15}$$

Since $\phi_b(\tau)/c_b$ is the coefficient of the translating mode $\psi_b(\xi)$, its increase represents movement to the left in the spatial coordinate ξ. The presented analyses above are performed in a moving frame, implying that the actual physical velocity corresponds to $v - \phi_b(\tau)/c_b$, which asymptotically approaches to

$$v_{prop} \to v - \frac{(2-\gamma^2)\tilde{\alpha} + \tilde{\beta} + 2v\delta}{2\delta}. \tag{4.16}$$

The propagation speeds of the soliton due to inter-site stiffness changes from this approximate relation are plotted in Fig. 4.2(a). When there is damping only ($\delta = 1$), the propagation speed approaches zero, becoming a static soliton. This result is physically reasonable since there are no other sources providing energy to the system to balance out the dissipated energy, thereby resulting in the static soliton solution. With the softening inter-site interaction ($\tilde{\alpha} < 0$), the propagation speed always stays positive, indicating that the soliton can travel an arbitrary distance without ever stopping. This can be an alternative method to attain a unidirectional wave propagation. With the stiffening inter-site interaction, on the other hand, the soliton slows down to zero, eventually changes the direction of

propagation, and continues to travel in the opposite direction. Similarly, Fig. 4.2(b) shows the propagation speed variations due to the on-site stiffness changes. They have identical trends to those of the inter-site stiffness changes: a decreasing stiffness leads to a continued propagation of a soliton, and an increasing stiffness leads to a returning wave.

The obtained results are also valid for the other (anti-kink) soliton solution $F_s(\xi,\tau) = -\tanh\frac{\xi}{\sqrt{2}}$. Any of the polarity changes in Eq. (4.11) from using the anti-kink solution will be recovered upon the projection on the first bound mode ψ_b so that the final differential equation and its solution will be identical to those of the kink soliton case. Thus, a series of alternating compression and rarefaction waves can be continuously triggered anywhere in this bistable lattice model, which is a limitation in the previous studies [69, 70, 97]. Therefore, the introduction of spatially graded properties reveals new physical mechanisms for sustaining the unidirectional propagation of solitary waves, as well as for obtaining the two possible topological soliton solutions, i.e. rarefaction and compression.

The condition $(2-\gamma^2)\tilde{\alpha}+\tilde{\beta}+2v\delta=0$ appears to reveal that the soliton propagates with a constant speed (two examples are plotted in dashed magenta in Fig. 4.2); yet, care must be taken as the small perturbation assumption no longer holds as τ grows large. The results can be improved by including the coupling terms and computing through an iterative process as described in [45]. However, the process requires highly convoluted calculations and lengthy expression. Instead, the qualitative behaviors from this approximate theoretical approach will be validated by the numerical analyses in the following section.

4.5 Numerical Simulations

For the numerical simulations, a central difference method [169] with a constant time step $\Delta\bar{t}=0.01$ is directly applied to the discrete equation of motion [Eq. (4.2)]. Linear variations are applied to both inter-site stiffness and on-site force changes for simplicity as done in the theoretical analyses, such that $\frac{(\bar{k}_{n+1/2}-\bar{k}_{n-1/2})}{\bar{k}_1}$ and $\frac{(\bar{\mathcal{F}}_{n+1}-\bar{\mathcal{F}}_n)}{\bar{\mathcal{F}}_1}$ are 0.015 for the softening cases and 0.02 for the stiffening cases. A large number of elements (N=500) are used to minimize the response distortion due to the boundary effects. However, only a limited number of elements (N=60) are used for the softening lattices since an arbitrarily long lattice can yield an unphysical negative value for the stiffness. To minimize the discreteness effects,

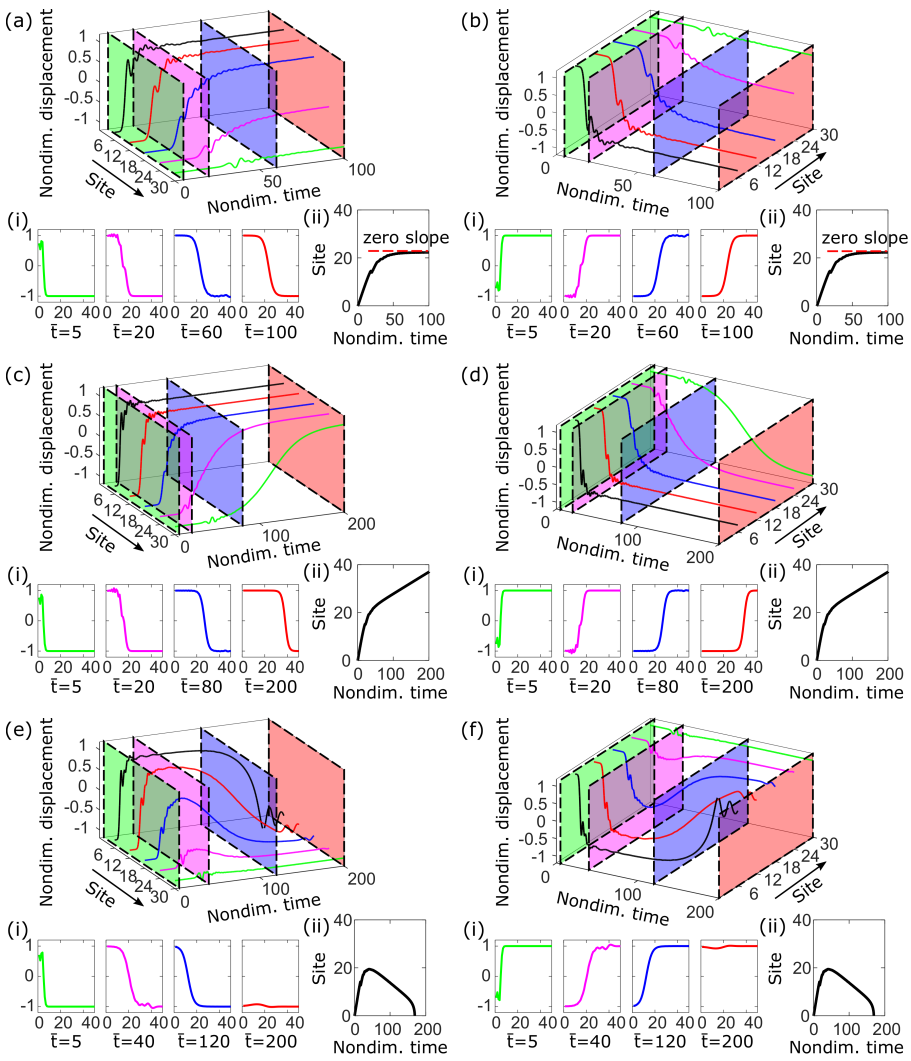

Figure 4.3. The propagation of (a) compressive and (b) rarefactional transition waves in the periodic bistable lattice, (c,d) the lattice with linearly decreasing inter-site stiffness, and (e,f) the lattice with linearly increasing inter-site stiffness. In the inset of each figure are (i) the wave profiles in the space configuration at the selected time instants of interest and (ii) the space-time contour of the transition wave.

the stiffness ratio between the inter-site and on-site members is chosen to be a large value (which assures gradual displacement changes between the neighboring sites); in this study, the reference inter-site stiffness is chosen to be 5 times higher than the reference on-site stiffness ($\omega_0^2 = 0.1$ and $u_0^2 = 1$). The input excitation is simulated by imposing an initial velocity condition ($d\bar{u}_1/d\bar{t} = \pm 2$) on the first element, and the same on-site damping $\bar{d} = 0.08$ is used throughout the simulations.

Due to the energy dissipation as a wave passes through each element, the triggered transition wave in a periodic bistable lattice is not expected to propagate indefinitely in physical settings. Figure 4.3(a) shows the time responses at the selected sites and the propagation fronts at several time instants (inset i) in a periodic lattice. The elements between the 18^{th} and 30^{th} sites cease to make complete transitions to the other states, and the wave becomes a stationary soliton after $\bar{t} \approx 60$. In the inset ii is the space-time contour of the transition wave, which is numerically obtained by measuring and plotting the time instant that crosses the zero displacement line for each site. The gradient of this contour corresponds to the propagation velocity, confirming that the speed approaches zero in a periodic bistable lattice with damping.

To allow a continued propagation of the transition wave, the total dissipated energy should not exceed the available energy in the lattice. Since the initial excitation energy is fixed and all the on-site potentials are symmetric, no additional energy can be supplied in the course of a wave transmission. One way to achieve the balance is by reducing the mechanical resistance, which is effectively done by continuously softening either the inter-site or the on-site stiffnesses. Figure 4.3(c) shows that the state transition occurs at every investigated site in the bistable lattice with softening inter-site stiffnesses. The continued translation of a transition wave in the space configuration at each successive time instant (inset i) reinforces the complete transmission of a transition wave through the lattice. The nonzero propagation speed in the inset ii is also in agreement with the theoretically predicted behavior.

A stiffening lattice may be thought of as a flipped version of a softening case. Due to the tendency of the softening lattice to discharge the signal in the softening direction, it is expected that the input signal would return to the excitation point. The time response of each element in the bistable lattice with linearly increasing inter-site stiffnesses is plotted in Fig. 4.3(e). In this case, the first few elements initially jump to the other stable states, but they return to their original states in due course. If seen in the space configuration [inset 4.3(e)-i], the main wave front shows a boomerang-like behavior; it initially moves in the direction of the excitation, changes the propagation direction at around site 20, and eventually returns to the excitation site. Again, the characteristic behavior in the space-time contour [inset 4.3(e)-ii] agrees with the theoretical result.

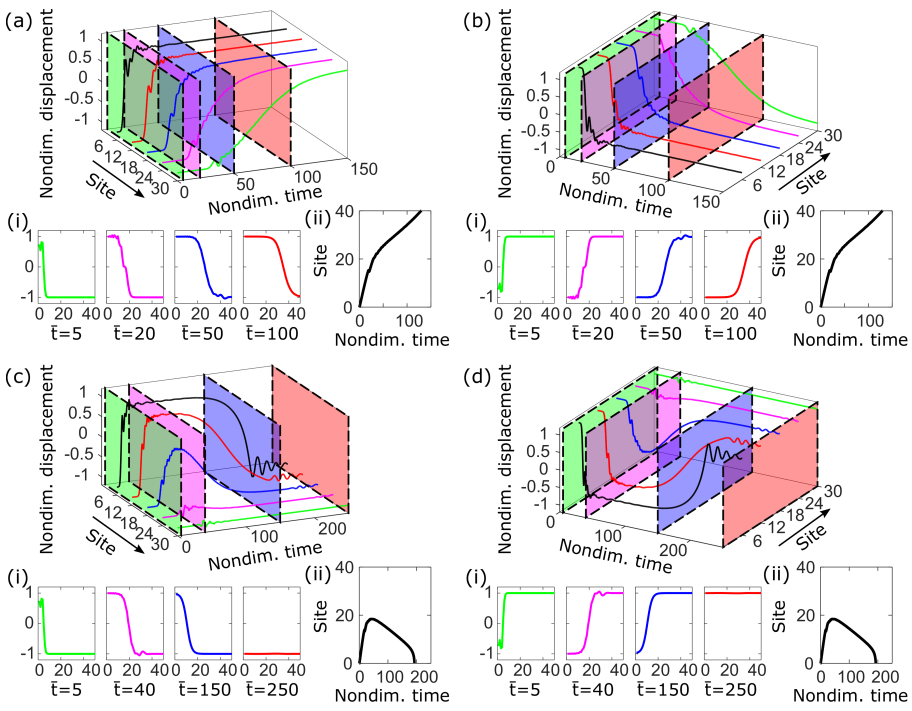

Figure 4.4. The propagation of (a) compressive and (b) rarefactional transition waves in the lattice with linearly decreasing on-site stiffness and (c,d) the lattice with linearly increasing on-site stiffness. In the inset of each figure are (i) the wave profiles in the space configuration at the selected time instants of interest and (ii) the space-time contour of the transition wave.

The observed transition waves in Figs. 4.3(a,c,e) are compressive in nature; however, the theoretical prediction implies that every compression wave is accompanied by a rarefaction wave. Figures 4.3(b,d,f) show the propagation of rarefaction waves for each type of the bistable lattices with identical parameters to those for the compression waves except that every on-site element is initially at the other stable state and that the excitation is applied in the opposite direction. It is worth noticing that the excitation is made from the same side of the lattice, enabling signals to be continuously sent from a single input site (site 1 in these examples). Furthermore, the proposed class of graded lattices allows for the rarefaction and compression waves to be triggered from any site on the lattice, remedying the limitation of previously studied periodic lattices. Other than the sign changes, the responses are exactly the same as in the cases with compression waves.

The same qualitative behaviors observed in the bistable lattice with the inter-site stiffness variations are present for the on-site stiffness variation as shown in Fig. 4.4. In the softening

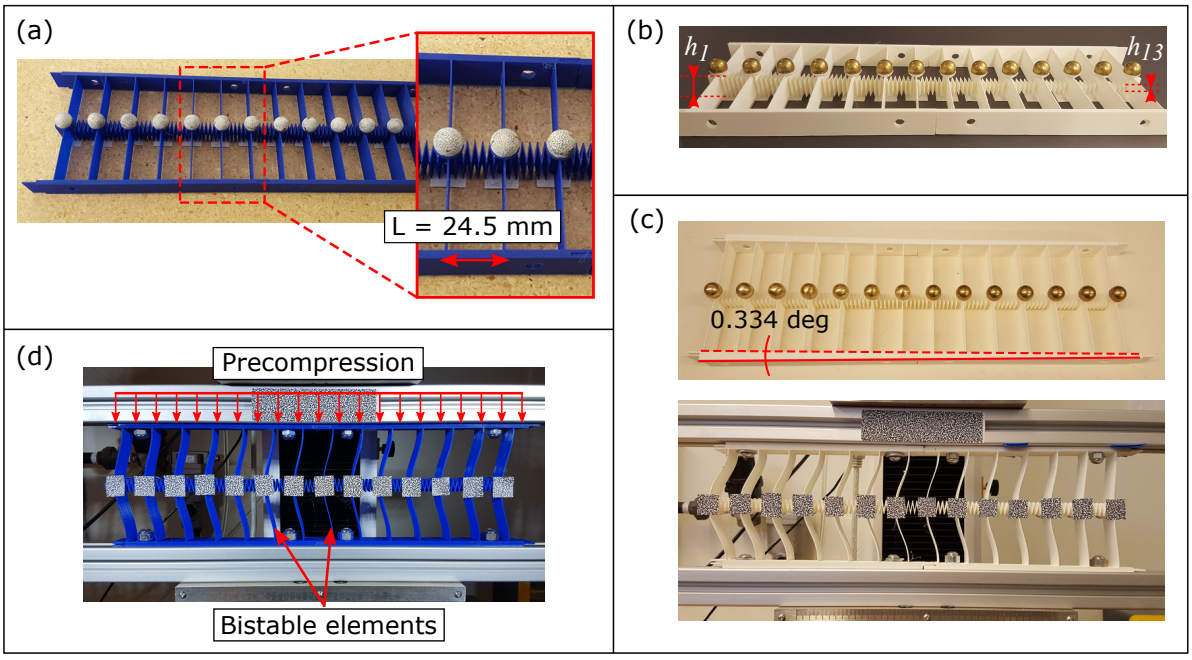

Figure 4.5. The 3D-printed samples for (a) the periodic bistable lattice, (b) the bistable lattice with inter-site stiffness grading, and (c) the bistable lattice with on-site potential grading. (d) The experimental setup, showing how to create the bistabilities in the on-site members.

direction of the on-site potentials, each successive on-site element becomes a preferred path, resulting in a complete propagation through the lattice [Fig. 4.4(a,b)]. In the stiffening direction, it acts as an increasing barrier, creating a boomerang-like wave transmission that can be observed by the returning of the wave form to the excitation site in the insets (i,ii) of Fig. 4.4(c,d). In the sense that the transition wave entering from one side propagates through the lattice, but the one entering from the opposite side does not, the bistable lattice with a monotonic stiffness variation can be viewed as a unidirectional lattice.

4.6 Experimental Validation

The experimental samples are prepared with a fused-deposition-modeling 3D printer (Ultimaker 3). Two sets of ladder-shaped lattices are 3D-printed and then glued together to form a lattice of 14 unit cells as shown in Fig. 4.5. A brass ball of diameter 12.7 mm and mass 9.36 g is glued to each web to form a unit cell, and each unit cell is connected to the

neighboring elements by spring-shaped features so that they can support both compressive and tensile forces. On the opposite side of the mass attachment, rectangular pieces of black and white speckled patterns are applied to allow for data collection with digital image correlation techniques. The bistabilities of the on-site potentials is achieved by imposing precompression controlled by a universal testing machine (Instron 3345). To collect the experimental dynamic responses, a pair of high-speed cameras (Photron UX100) are used with a frame rate of 2000 fps. The width of the analysis area is focused on the first 7 element from the excitation point to allow for sufficient picture resolution while capturing enough elements to observe the desired behaviors. The collected images are post-processed using a commercial digital image correlation software (VIC-3D).

Each unit cell is identically designed for the periodic lattice, and 1 mm of precompression is applied, resulting in a snapping distance of about 15 mm between the two stable states. Figure 4.6(a) shows the time responses of the first 7 elements of the periodic lattice from the excitation site[2]. The displacements are measured with respect to the initial stable states. It can be observed that the first two elements display complete transitions to the other stable states while the 7^{th} element remains at the same initial state after a transient motion. (The final displacements of the intermediate elements are progressively dispersed between two stable states, which is in line with the gradual variation condition for the continuum-limit approximation.) This implies that the transition wave does not propagate through the lattice. The observed stabilization as time grows indicates that the transition wave stops inside the lattice, becoming a stationary soliton just as predicted in the theoretical and numerical analyses.

The inter-site stiffness variation is controlled by gradually changing the height of the inter-element spring elements as shown in Fig. 4.5(b); the stiffest spring has h_1=17 mm, and the softest spring has h_{13}=5 mm. For the lattice with linearly decreasing inter-site stiffness [Fig. 4.6(c)][3], all of the elements transition into the other stable states, in agreement with the theoretical and numerical predictions. The slight differences in the final displacements

[2]See Supplemental Video S1 for the complete motion in the periodic lattice.
[3]See Supplemental Video S2 for the complete motion in the lattice with decreasing inter-site stiffness.

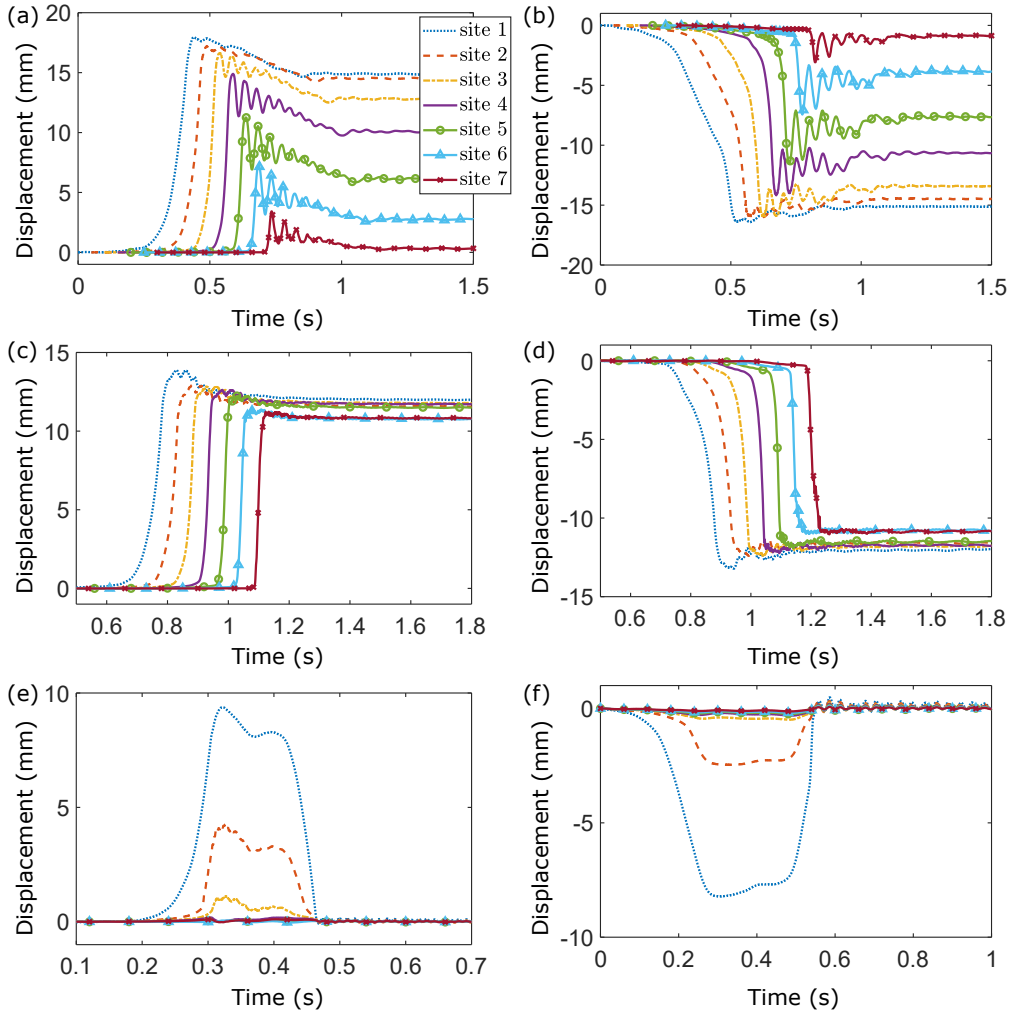

Figure 4.6. The time response of the experimental lattices at site 1-7. The propagation of (a) compression and (b) rarefaction waves in the periodic bistable lattice, (c,d) the lattice with linearly decreasing inter-site stiffness, and (e,f) the lattice with linearly increasing inter-site stiffness. Each individual displacement in (a-d) is offset in the time axis by 0.05 s for a better presentation of the results.

after the transition wave passes are due to the imperfections in the test fixtures and the manufacturing variations.

To observe the behavior in the lattice with linearly increasing inter-site stiffness, the same lattice as in the decreasing case is used except that now the excitation is made at the opposite end (where the spring stiffness is the softest). In this case, all the analyzed elements return to the initial stable states even though the first element hits the other stable state

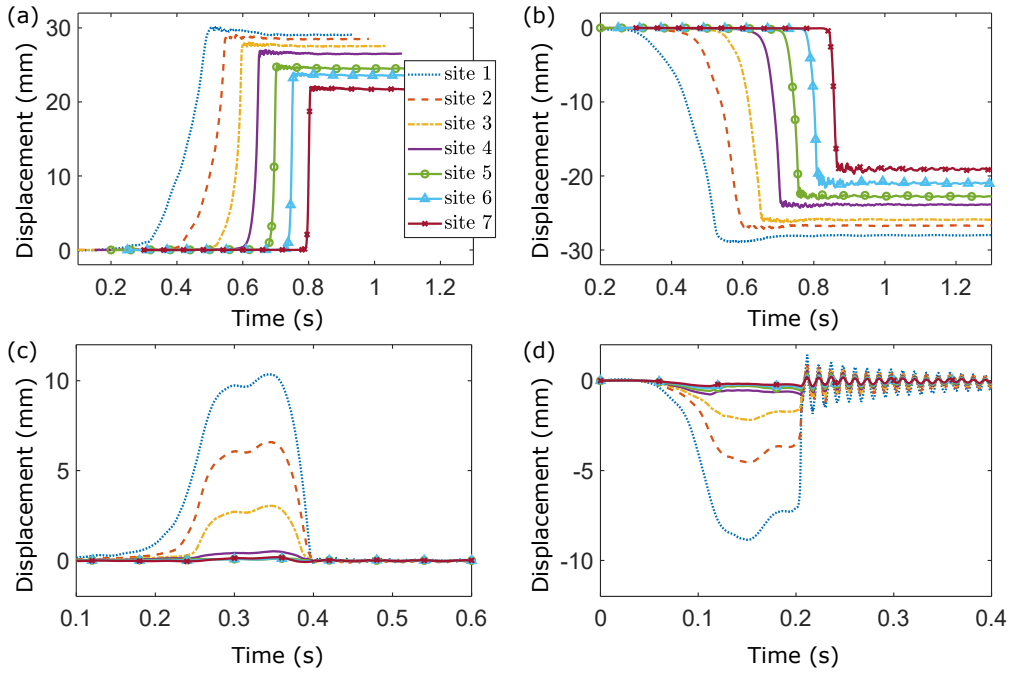

Figure 4.7. The time response of the experimental lattices with on-site stiffness grading at site 1-7. The propagation of (a) compression and (b) rarefaction wave in the lattice with decreasing on-site stiffness and (c,d) the lattice with increasing on-site stiffness. Each individual displacement in (a,b) is offset in the time axis by 0.05 s for a better presentation of the results.

briefly [Fig. 4.6(e)][4]. The limited manufacturing precision prevents us from showing the more extreme boomerang-like behavior, where the transition wave travels further in the stiffening direction before returning to the excitation point. However, such behavior is physically attainable with the higher ratio between the inter-site and on-site stiffness values as can be partially observed in Video S4[5], where the transition wave is triggered at an internal site with a greater inter-site stiffness. Figures 4.6(b,d,f) show the measured responses of the bistable lattices initially at the second stable states under tensile input excitations. The transmissions of the rarefaction transition waves exhibit the same characteristic behaviors as those of compression waves except the changed polarities and slight deviations in values due to irregularity of the test setup.

The on-site stiffnesses are controlled by applying different precompression levels. This is achieved by designing the flanges with an initial draft angle of 0.334 deg as shown in

[4]See Supplemental Video S3 for the complete motion in the lattice with increasing inter-site stiffness.
[5]See Supplemental Video S4 for internally excited motion in the lattice with increasing inter-site stiffness.

Fig. 4.5(c). Thus, as the two flanges are installed on the parallel test rigs, each individual element is compressed by a differing amount. The precompression is applied in such a way that the softest on-site member is compressed by 0.5 mm and the stiffest on-site member by 6 mm. The experimental realization for this case results in the slight deviations from the expected theoretical and numerical observations as the precompression introduces longer snapping distances, which is evident from the different displacements after the state transition occurs at each site in Fig. 4.7(a,b). Also, a linear change in compression does not necessarily mean a linear change in the stiffness. However, it is difficult to manufacture linearly-varying on-site buckled elements with constant snapping distances with the inherent nonlinear geometry, and thus we opt for qualitative comparison in this study. The overarching effects of having decreasing (increasing) on-site potentials are the same as the effects of decreasing (increasing) inter-site stiffnesses, confirming the theoretical and numerical predictions. Figures 4.7(a,b) and Video S5[6] show the complete transmission of an anti-kink and a kink from a single excitation point; Figs. 4.7(c,d) and Videos S6[7] and S7[8] show the reflections of them.

4.7 Conclusions

In this study, we have investigated the effects of introducing spatially graded properties to lattices of bistable elements. Our theoretical analysis predicts that the generated solitary waves cannot propagate completely through the lattice in a physical setting with nonzero damping, using a perturbation method. Rather, these waves become stationary solitons, meaning that the propagation of a transition wave stops inside the lattice. Either linearly decreasing inter-site or linearly decreasing on-site stiffnesses enable the continued propagation of transition waves through the lattice even under the presence of strong damping. On the other hand, an interesting boomerang-like transmission of a transition wave is predicted for such lattices with linearly increasing inter-site or on-site stiffnesses. These transmission characteristics constitute an alternative way of achieving unidirectionality. A series of

[6]See Supplemental Video S5 for the complete motion in the lattice with decreasing on-site stiffness.
[7]See Supplemental Video S6 for the complete motion in the lattice with increasing on-site stiffness.
[8]See Supplemental Video S7 for internally excited motion in the lattice with increasing on-site stiffness.

numerical simulations and experiments on the 3D-printed bistable lattice samples validate all of our theoretical predictions. The observed behaviors manifest that the directionality of transition waves can be controlled drastically through small manipulations in material-level designs. Furthermore, such architecturing enables the existence of both compression and rarefaction solitons. This allows a simple, yet effective mechanism for creating multi-functional metamaterials with built-in energy harvesting capability owing to the intrinsic resetting mechanism that enables the continued transmission of the transition wave pairs. Further technological applications exploiting the spatial grading of properties are envisioned. For example, a softening arrangement can be used as a robust signal transmission network while the integrated transducer at each unit cell converts energy from the traveling solitary waves. In the stiffening direction, the lattice can act either as a protective material that blocks any transmission of catastrophic inputs or as a phase delaying mechanism while still manipulating the solitary waves for power conversion.

4.8 Acknowledgments

M. Hwang and A. F. Arrieta gratefully acknowledge the support of the Purdue Research Foundation (PRF); this research was supported through start-up funds provided to Prof. A. F. Arrieta.

5. EXTREME FREQUENCY CONVERSION FROM SOLITON RESONANT INTERACTIONS

Myungwon Hwang, Andres F. Arrieta

This chapter is under review in:
Physical Review Letter, 2021.
DOI: TBA
Supplementary Information is attached as Appendix C.

5.1 Abstract

We present a metastructure architecture with a bistable microstructure that enables extreme broadband frequency conversion. We use numerical and experimental tools to unveil the relationship between input excitations at the unit cell level and output responses at the macrostructural level. We identify soliton-lattice mode resonances resulting in input-independent energy transfer into desired metabeam vibration modes as long as transition waves are triggered within the metastructure. We observe both low-to-high and high-to-low incommensurate frequency interactions in the metabeams, thus enabling energy exchange between bands two orders of magnitude apart. This behavior generalizes fluxon-cavity mode resonance in superconducting electronics providing a general method to extreme frequency conversion in mechanics. Importantly, the introduced architecture allows for expanding the metamaterials design paradigm by fundamentally breaking the dependence of macroscopic dynamics on the unit cell properties. The resulting input-independent nature implies potential applications in broadband frequency regulation and energy transduction.

5.2 Introduction

Solitary waves appear in various physical systems [31] playing a pivotal role in applications, including waveguiding [185], photonics [186], optical communications [187], reversible logic gates [188], lasing [189], morphing structures [190], non-destructive testing [191], and soft robotics [192]. A unique aspect of solitons is their quasi-particle characteristics. This

allows for better imaging using sonic bullets [163] or dense wavelength-division multiplexing for optical communications exploiting cavity solitons [193]. Solitons' resonant interactions with cavities have enabled the generation of lasers exhibiting frequency conversion not readily available with conventional sources exploiting fluxons – a type of transition wave or topological soliton – in Josephson junctions [194]. Such extreme frequency conversion in mechanical systems is less common and is typically achieved via subharmonic/superharmonic/combination resonances [129] and nonlinear coupling between normal modes [118]. Nonlinear multimode metamaterials can provide alternate ways to attain frequency conversion through their amplitude-dependent dispersion relations [26, 29]. Inter-modal interactions through nonlinearly generated higher harmonics have been theoretically and experimentally demonstrated, enabling energy exchange between different wave modes [132–134]. Furthermore, magnetic metamaterials featuring engineered defects have demonstrated conversion from high to low-frequency modes through resonant coupling between localized defect modes and extended lattice modes [119]. However, to excite these interaction mechanisms, the defect mode's frequency needs to be commensurate with or a combination of the system's modes, still limiting the attainable frequency bandwidth.

Lattices composed of bistable elements can support transition waves exhibiting particle-like behavior [46–48]. When the constitutive onsite members are built with asymmetric bistable elements, transition waves become unidirectional [69, 70] and exhibit unique input-independent dynamics [97], implying strong potential for broadband applications. Enabling nonlinear interactions similar to fluxon-cavity mode resonances offers the potential for extreme energy conversion currently absent in mechanical systems exploiting the input frequency-independence of transition waves. In this study, we demonstrate extreme energy exchange in mechanical systems with metabeams composed of a bistable microstructure, promoting nonlinear coupling between wave and metastructural modes in an analogous process to fluxons interacting with cavity modes in superconductors [189, 194]. Importantly, the soliton resonant interactions enable extreme frequency conversion and response manipulation without recourse to dispersion-related phenomena in mechanical systems. The unveiled dynamics are insensitive to the excitation frequency, thus laying the foundation for a new

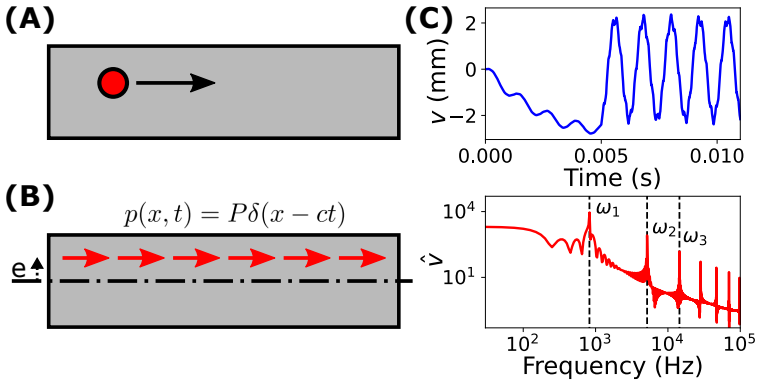

Figure 5.1. (A) Beam subjected to a moving particle and (B) its schematic representation. (C) 7-term approximation of the transverse displacement and its frequency spectrum for a fixed-free beam.

physical mechanism, the dynamics of which are independent of the metamaterial building block size.

5.3 Beam Subjected to a Moving Particle

The fundamental dynamics in soliton-metastructure interactions can be described by a beam subjected to in-plane moving particles [Fig. 5.1(A)]. The motion of a single particle traveling along the beam's length can be mathematically represented as a distributed impulse $p(x,t) = P\delta(x-ct)$ for $0 < t < \frac{L}{c}$, where P, c, L, and δ are the forcing amplitude, the particle speed, the beam's length, and Dirac-Delta function, respectively. We assume an Euler-Bernoulli beam subjected to an in-plane load applied at a distance e from the neutral axis to excite the transverse motion exploiting eccentricity [Fig. 5.1(B)]. The governing equation for the transverse displacement $v(x,t)$ is:

$$EI\frac{\partial^4 v(x,t)}{\partial x^4} + \rho A\frac{\partial^2 v(x,t)}{\partial t^2} = \mathrm{e}\frac{\partial p(x,t)}{\partial x}, \tag{5.1}$$

where the bending stiffness EI, density ρ, cross-sectional area A, e, and P are constant. Eq. (5.1) can be solved by a modal expansion $v(x,t) = \sum_{n=1}^{\infty} q_n(t)\phi_n(x)$, where $q_n(t)$'s are

the generalized Fourier coefficients corresponding to the normal modes $\phi_n(x)$'s. The solution for $q_n(t)$ is of the form:

$$q_n(t) = \begin{cases} a_n \sin\omega_n t + b_n \cos\omega_n t + c_n \phi_n(ct) & \text{for } 0 < t \leq \frac{L}{c} \\ d_n \sin\omega_n t + \mathrm{e}_n \cos\omega_n t + f_n \sin\omega_n(t - \frac{L}{c}) + g_n \cos\omega_n(t - \frac{L}{c}) & \text{for } t > \frac{L}{c}, \end{cases}$$

where a_n, b_n, c_n, d_n, e_n, f_n, and g_n are the constants determined by the system parameters, and β_n is the eigenvalue for n^{th} normal mode. There are explicit frequency components ω_n's from the natural modes of the beam and $c\beta_n$'s from the speed of the moving impulse. However, the former dominates the frequency response as the response time becomes much larger than the particle's travel time (i.e., the particle is sent intermittently). An example 7-term approximation of the tip displacement for a fixed-free beam and its response spectrum reveals that a moving impulse excites the normal modes of the beams [Fig. 5.1(C)], where the lowest mode has the greatest contribution. (See Sec. 1 of Supplemental Material [195] for details.)

5.4 Metabeams with Underlying Bistable Microstructures

Bistable lattices can support particle-like modes in the form of transition waves, potentially realizing the conceptual metabeam with moving particles. We construct a beam-like frame with an underlying bistable architecture, inspired by spring-mass constitutive cells [48], and introduce an offset from the centerline of the frame [dashed-dot line in Fig. 5.2(A)] to break the microstructure's cross-sectional symmetry and amplify the flexural motion. A fixed-free boundary condition is used; however, the ensuing dynamics are independent of the boundary conditions [195]. A force input is applied in the in-plane direction at the leftmost node of the internal bistable lattice with a sinusoidal excitation $p(t) = F \sin\Omega t$, where F is the forcing amplitude and Ω is the input angular frequency, and the output displacement is measured at the top rightmost node in the out-of-plane direction. [See Fig. 5.2(A) and Sec. 2 of Supplemental Material [195] for the full metabeam description and design parameters.]

The metabeam's dynamics are simulated using Abaqus/Standard implicit nonlinear solver and reported in *output frequency diagrams* [Fig. 5.2(C)]. These diagrams show the frequency

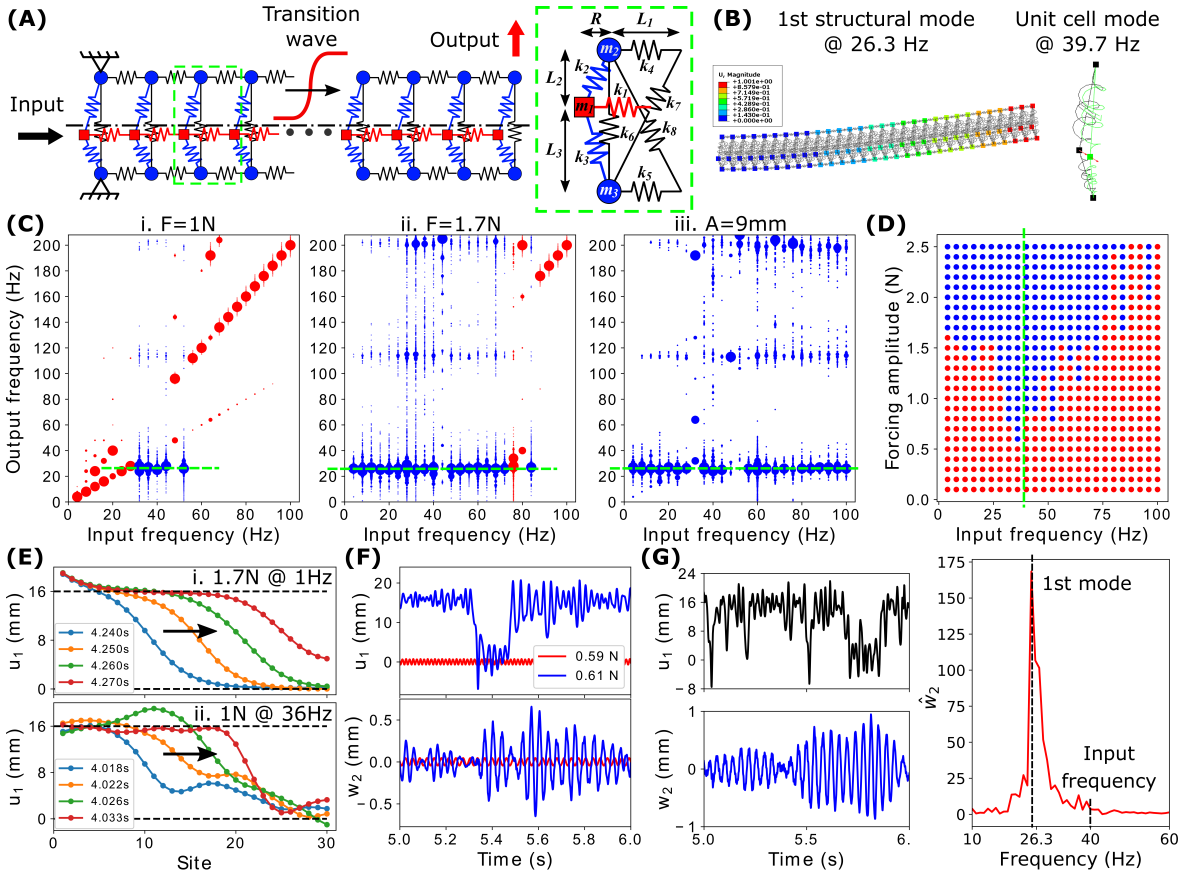

Figure 5.2. (A) Schematic representation of the metabeam. (B) Natural modes of the macroscopic structure and unit cell. (C) Output frequency diagrams for various input conditions, showing the output frequency content for each input frequency. (D) Response map in terms of input forcing amplitude and frequency, where blue dots indicate that transition waves are triggered. (E) In-plane displacements of the center masses in space configuration, showing transition wave propagation. (F) Response amplification when transition waves are triggered (in blue) compared to when they are not triggered (in red). (G) Representative response of solitonic resonance, obtained for F= 1 N at 40 Hz.

contents of the output responses as a function of the input frequency. Each dot in the diagram represents the available frequency component of the output response, while its size indicates the relative intensity [1]: larger (smaller) dots indicate higher (lower) spectral amplitudes for the shown output frequencies. Blue dots indicate the excitation of in-plane transition waves within the metabeam, while red dots represent responses involving no phase transitions.

[1]The relative intensity is calculated by $|\hat{w}_{\mathrm{i}}|/|\hat{w}|_{max} \times 100\%$, where $\hat{w}_{\mathrm{i}}$ is the Fourier amplitude of the i$^{\mathrm{th}}$ frequency component, and $|\hat{w}|_{max}$ is the maximum magnitude of the Fourier amplitudes.

The frequency spectrum is obtained when the system attains steady-state, using fftpack from Python's scipy library at 1000 Hz sampling frequency without a window function.

5.5 Solitonic Resonance

Transition waves can be viewed as traveling quasi-particles [31, 45]. As predicted from the analogy with the beam subjected to a moving particle, transition waves primarily excite the fundamental mode of the macroscopic metastructure [Fig. 5.2(B)]. This is indicated by the output frequencies collapsing to a single dominant value matching the fundamental mode's frequency independently from the excitation frequencies [dashed line in Fig. 5.2(C)-i]. The slight deviations from the fundamental mode are due to the convolution with the low spectral components of the concentrated transition waveform. Transition waves can be excited indistinctly via quasi-static or dynamic inputs but are more easily triggered around the unit cell mode, as indicated by blue dots in the response map [Fig. 5.2(D)]. The particle-like nature of the transition waves can be clearly identified by the stable propagation of the kink-shaped waveform in the in-plane direction in the space configuration [plotted for a quasi-static input of 1 Hz in Fig. 5.2(E)-i]. For higher input frequencies [36 Hz in Fig. 5.2(E)-ii], the waveform is distorted by nonlinear interactions with other lattice modes; however, the waveform starting at one stable state and ending at another is clearly identifiable. Transition wave propagation involves a drastically larger amplitude than that caused by other wave modes, and so their effects dominate the resulting motion. With only ∼3.4% increase in the forcing amplitude, the output displacement amplifies as much as ∼14 times [Fig. 5.2(F)] [195].

Figure 5.2(G) shows an in-plane displacement u_1 of the internal mass and the corresponding out-of-plane displacement w_2 of the top mass at the metabeam's free end when transition waves are triggered (F= 1 N and Ω= 40 Hz). The Fourier component $\hat{w}_2$ of w_2 clearly indicates that the dominant response frequency is near the first structural mode with negligible contribution from the input frequency. The disappearance of the input frequency contribution can be explained by the chaotic nature of the snap-through instability [130], which induces state transitions at an aperiodic rate, uncorrelated to the input frequency. Thus, the effect from the occurrence rate of transition waves disperses in the frequency spectrum, leaving their transient effect to dominate the out-of-plane response. In the sense that

generation of transition waves, topological solitons, yields a coherent output frequency, we name this phenomenon as *solitonic resonance*.

As the forcing amplitude increases, the input bandwidth yielding solitonic resonance broadens [Fig. 5.2(C)-ii and Movie S1]. Alternatively, the metastructure can be excited by a prescribed displacement input of the form $R - A\cos(\Omega t - \phi_0)$ to broaden the bandwidth, where A and ϕ_0 are the input amplitude and phase constant. This type of excitation is more relevant for application in which the inertial force of the contacting excitation source is large compared to the structure's reaction force. The system's response under prescribed displacement inputs is governed dominantly by the excitation term, resulting in transition wave generation for almost the entire frequency range [Fig. 5.2(C)-iii]. Solitonic resonance is still observed as interactions between newly generated and previously traveling transition waves occur at a non-definite rate. This behavior is valid except for very low input frequencies for which the forcing period is longer than the time required by a transition wave to traverse back and forth through the whole lattice. It is further observed that even noisy input sources can be transformed into a single coherent response mode [195]. Thus, the strongly nonlinear dynamics displayed by the proposed metastructures yield a robust mechanism for broadband frequency conversion into a coherent output frequency.

Other potentially useful nonlinear behaviors exist outside the solitonic resonance domain, such as second harmonic generation (between 12 Hz and 20 Hz) or frequency doubling (above 44 Hz) (See Sec. 7 of Supplemental Material [195]). These will be addressed in detail in a separate study.

5.6 Tuning Flexibility

The simplicity and periodicity of the proposed metastructure allow the operating bandwidth to be easily tuned to suit a vast range of applications. The unit cell design dictates the central input frequency around which the solitonic resonance emerges, while the overall metastructure topology controls the corresponding output frequency. Quadrupling k_2 and k_3 doubles the in-plane unit cell mode, resulting in shifting the input frequency band for solitonic resonance to a higher frequency region [Fig. 5.3(A)-i]. On the other hand, qua-

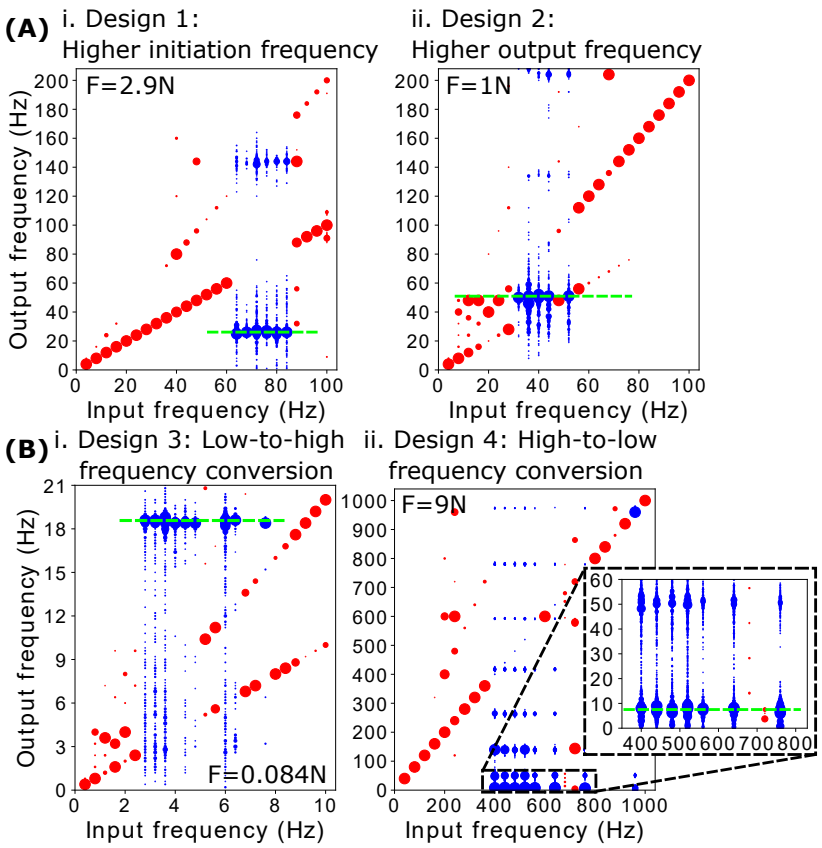

Figure 5.3. Output frequency diagrams for various unit cell and external frame design combinations, demonstrating extreme tuning flexibility. (A) Design 1 increases the initiation frequency of the solitonic resonance, and Design 2 increases the output frequency. (B) Output frequency diagrams for metabeam designs tuned to enable low-to-high and high-to-low frequency conversions, where the input and output frequencies are 1-2 orders of magnitude apart.

drupling k_4, k_5, k_6, k_7, and k_8 approximately doubles the original natural frequencies of the macrostructure, shifting solitonic resonance to a higher output frequency [Fig. 5.3(A)-ii].

The metabeam can also be tuned to display remarkable energy exchanges between incommensurate frequency bands, which can be separated by several orders of magnitude. Figure 5.3(B) shows two examples (see Supplemental Material [195] for the design parameters), where one is optimized to operate at 3-5 Hz range yielding ∼18.63 Hz solitonic resonance [2] and the other at 400-560 Hz range yielding ∼8.30 Hz solitonic resonance. The

[2]The internal bistable elements are softer to accommodate the low triggering frequencies. Thus, small contributions from these internal lattice modes coexist below the solitonic resonant frequency.

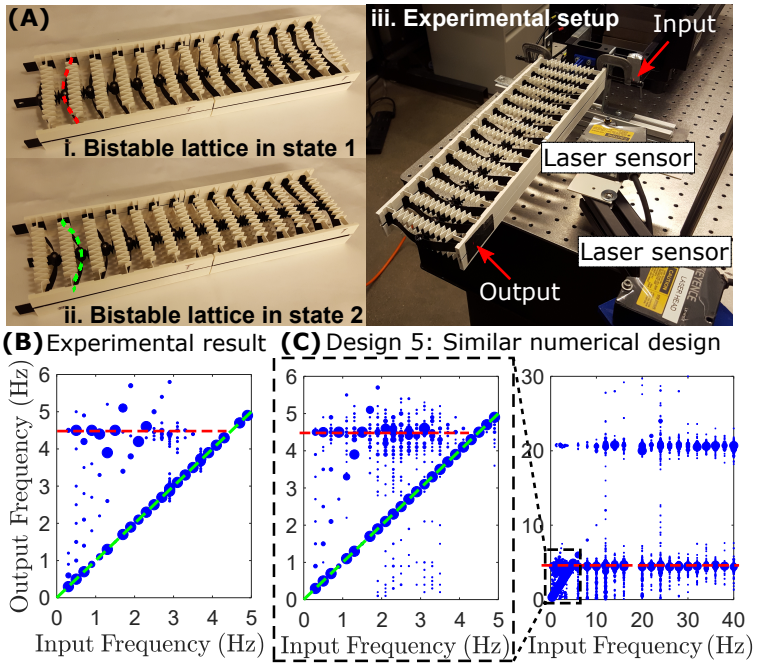

Figure 5.4. (A) Experimental demonstrator showing (i,ii) two globally stable configurations indicated by red and green lines, and (iii) shaker test setup. (B) Output frequency diagrams from the experiment. (C) Output frequency diagram for a qualitatively similar numerical design. The zoomed plot shows the low-frequency response corresponding experimental range.

tuning flexibility in the presented metastructures thus yields a blueprint for unprecedented dynamical manipulation from an intrinsically nonlinear interaction.

5.7 Experimental Results

While the spring-joined design allows for a straight-forward physical description, a post-buckled beam design as the microstructure's unit cell is more advantageous to achieve bistability in an experimental demonstrator. An experimental metabeam was built by 3D-printing a ladder-like structure [black component in Fig. 5.4(A)], the rungs of which are interconnected by spring-like features at a small offset from the metastructure's centerline. Additionally, the metastructure is fitted between a set of flexible holders [white components in Fig. 5.4(A)], providing flexibility in the transverse direction and allows two macroscopically different stable states [dash lines in Fig. 5.4(A)-i,ii]. Fixed-free boundary conditions were realized by clamping one end of the structure. Sinusoidal displacement inputs were imposed at the first

element in the in-plane direction through an electrodynamic shaker. The input and output displacements were measured by a set of laser displacement sensors, pointing at the flat surfaces of the shaker head and near the free end of the structure, respectively. The overall experimental setup is shown in Fig. 5.4(A)-iii. More detailed fabrication and experimental methods are given in Sec. 8 of Supplemental Material [195].

Increasing the imposed displacement amplitude triggers transition waves, revealing an output frequency branch close to the natural frequency (4.62 Hz [195]) of the macrostructure [red dashed line in Fig. 5.4(B) and Movie S2]. This branch corresponds to solitonic resonance in that the resulting frequencies are coherent around the macrostructural mode and different from the input frequencies. Additionally, we observe a branch corresponding to the input frequencies (green dashed line), which occurs due to the shaker's limited input frequency band. The long stroke needed to induce the snap-through at the first element (triggering the transition wave) results in a much slower rate than the transition wave's propagation. Hence, every element's inter-well oscillation takes place at the same frequency as the input frequency resulting in the observed contribution from the input in the output responses. With the low input frequency limit, the solitonic resonance's primary source is the superharmonic response of the metabeam; the output frequencies in this branch are commensurate for input frequencies below 2.3 Hz. However, for input frequencies above 2.5 Hz, the harmonics of which are not close to the structural mode, the contribution from the free vibrations becomes observable [see the spectral content around 4.5 Hz in Fig. S7(F)], resulting in the input and output frequencies becoming once more incommensurate. Regardless of the physical mechanisms, transition wave generation facilitates the solitonic resonance in the output response.

To circumvent the experimental limitations, we construct a numerical model displaying qualitatively similar dynamics to the experimental metabeam. This is achieved by matching the unit cell's natural frequency and the fundamental macrostructural mode of the numerical model to the experimental metabeam (see design parameters in Supplemental Material [195]). Its simulated output response diagram displays qualitative agreement with the experimental response, for example, capturing the coexisting solution branch [Fig. 5.4(C)]. Numerical simulations for this case are extended to a higher input frequency range, still

showing the output frequency branch concentrated at ∼4.5 Hz but almost eliminating the branch corresponding to the input frequencies, in accordance with the result in *Solitonic resonance* section. The dominance of the transient effect over the input frequency effect can be manipulated by the system damping as long as manufacturing technology allows (see Sec. 11 of Supplemental Material [195]). Although the force-controlled cases could not be confirmed experimentally, the agreement with the predicted dynamic characteristics of the qualitatively similar metabeam under displacement-controlled inputs supports the validity of the numerical results.

5.8 Conclusions

We demonstrate nonlinear interactions involving solitary wave and vibration modes, resulting in extreme frequency conversion in generic bistable metastructures. Notably, the observed phenomenon defined as *solitonic resonance* allows for a remarkably stable means to achieve input-independent frequency conversion, in which the output response is unaffected by wave dispersion. This behavior generalizes analogous fluxon-cavity mode resonance in superconducting electronics, providing an exemplary platform for frequency regulation and energy conversion applications across physical fields. The tuning flexibility of the presented metabeam also allows for extreme energy exchange between incommensurate frequencies separated by orders of magnitude. Importantly, the presented architecture provides a general model system for realizing unique properties in metamaterials at frequencies not dictated by the unit cell, opening up new avenues for attaining extreme dynamics.

5.9 Acknowledgments

The authors thank Prof. C. Scalo for supporting the development of the in-house Fortran code; The authors are grateful for Dr. E. Arrieta Diaz's help in motivating this work beyond mechanics; We acknowledge the financial support from the National Science Foundation under grant CMMI-1935137.

6. HIGH-PERFORMANCE COMPUTING ARCHITECTURE FOR PARALLELIZED COMPUTATION OF METASTRUCTURES COMPOSED OF MULTI-STABLE UNIT CELLS

Myungwon Hwang, Andres F. Arrieta, Carlo Scalo

This chapter is to be published in 2021.
Supplementary Information is attached as Appendix D.

6.1 Abstract

In this work, we use message-passing interface (MPI) to develop high-performance parallel solvers that analyze generic lattice structures composed of bi- or multi-stable elements. The codes are thoroughly validated against a commercial numerical solver (Abaqus) and well-established serial codes from the previous studies. We can achieve up to 4^{th}-order solution accuracy with the fully explicit Runge-Kutta (RK) methods, exceeding what many commercial structural analysis tools provide. With our parallel code dedicated to solving the specific problem types, the absolute computational speed can be improved by three orders of magnitude. More importantly, the in-house implementation enables an effective distribution of the computational load following the intrinsic structural periodicity, thus achieving extreme scalability as the number of processes increases. We also present an amplitude-dependent energy flow diagram in a bistable metabeam and the stability of the transition wave's propagation speed in a one-dimensional bistable lattice to showcase our code's capability to handle massively large problems. The achieved numerical and computational performance gains open up the potential to uncover new dynamics by drastically expanding the accessible analysis domains.

6.2 Introduction

In recent decades, metamaterials based on bi-stable or multi-stable microstructures have paved ways to surpass the dynamics which conventional materials can provide. Example properties include extreme wave directionality [69, 70], bandgap transmission [196, 197], input-independent dynamics [97], which can be utilized for various applications across the fields of engineering, such as energy trapping [153, 198], energy harvesting [97], and mechanologic [70, 199]. Such metamaterials are typically composed of repeating microstructures, and the resulting dynamics are best explained by the associated dispersion relations. For many simple periodic structures, the linear and weakly nonlinear [26, 29] wave dispersion relations can be readily obtained through systematic approaches on a single unit cell, such as Bloch wave theorem [136] or transfer function method [137]. Although simple mathematical designs provide an inexhaustible framework for understanding the fundamental physics behind the operating principles, more complex microstructure designs [71, 200–203] or perturbations (e.g., functional grading [170, 204]) in the lattices are typically desired for more practical applications. Obtaining the dispersion relations for such complex designs through analytical means becomes challenging, if not impossible, even with the aid of symbolic analysis tools. Furthermore, the recent work utilizing a bi-stable lattice with unconstrained transverse motion enables an input-independent energy transfer between frequencies orders of magnitude apart [205]. Since the interaction with the transition waves, which are quasi-particles traveling through the metastructure, is fundamental to the appearance of this extreme behavior, its dynamics cannot be obtained from the analyses of its unit cell only.

Due to the strong nonlinearities involved in achieving the desired dynamics, systematic analytical approaches are limited, and so numerical approaches inevitably need to be complemented. For the analyses of the complex metamaterials or metastructures, researchers use either commercial solvers, such as COMSOL [134, 201, 206, 207] and Abaqus [73, 205, 208–210], or in-house implementations in preferred programming languages [97, 132, 202, 204, 211]. However, the challenge with the general-purpose commercial softwares is that the solvers are not tailored to work optimally for a specific class of problem. For exam-

ple, it takes about half a day to obtain a single output frequency diagram for a 30-element bistable metabeam presented in Ref. [205] even with modern high-end computing systems. Even with the in-house implementations, much less focus has been on the computational performance as the analyses are limited to small finite lattices only. The metamaterial research's ultimate directions are to realize physical material through miniaturization of the microstructures or build higher-dimensional functional structures out of the metamaterial building blocks, both of which require simulations of millions of unit cells. Such a massive problem was once deemed impossible to solve from the direct computation of its microscopic components so that people have either imposed restrictions on the boundary conditions or developed separate macroscopic approaches. However, as cutting-edge computer technology becomes more affordable and accessible to the general public, a full-scale characterization of such a problem is no longer unimaginable with a dedicated solver for a specific problem type. Moreover, the recent technological advancements of the central processing units (CPU's) are more toward increasing the number of cores than increasing the clock speed, making the parallel implementation more pertinent.

The repeating building blocks of metamaterials and metastructures inherently stage for efficient parallel implementation, such that the computational load can be evenly distributed among multiple local processes. In this study, we adopt the message-passing interface (MPI) to develop a high-fidelity simulation tool that can run on millions of parallel processes for analyzing generic bi- or multi-stable metastructures. With this in-house implementation, we seek to extend the achievable numerical accuracy and achieve a significant performance boost in analysis time to enable computation of a large number of massively large problems expeditiously. The achieved performance gains allow the investigation of the previously unreachable analysis domains, hence potentially unveiling new extreme dynamics.

6.3 Metastructures of Bi-stable Unit Cells

This study's primary interest lies in unveiling the rich nonlinear dynamics associated with architectures composed of bi- or multi-stable unit cells expeditiously. To that end, we consider a metabeam composed of underlying bi-stable microstructures, a one-dimensional (1D) lattice with quartic onsite potentials (discrete ϕ-4 model), and a 1D multi-stable lattice

with coupled pendula (discrete sine-Gordon model). Although the physical interpretations differ, the governing equations of all the architectures share the same form as follows:

$$M\ddot{u}_n = \mathcal{F}_{\text{intersite}}(u_{n-1}, u_n, u_{n+1}) + \mathcal{F}_{\text{onsite}}(u_n), \tag{6.1}$$

where M is the diagonal inertial matrix, u_n is the displacement vector at n^{th} site, $\mathcal{F}_{\text{intersite}}$ and $\mathcal{F}_{\text{onsite}}$ are generic (linear or nonlinear) functions for inter-site and onsite forces, respectively, and the overdot represents the derivative with respect to time t. The detailed designs and the specific expressions for the governing equations can be found in the respective references [31, 205]. This set of governing equations is highly coupled and nonlinear, for which the closed-form solutions do not exist. Thus, implementing an efficient numerical solution tool is imperative to investigate their rich dynamics fully. Various boundary conditions (cantilevered, simply-supported, and fixed-fixed conditions) are considered to encompass a variety of applications.

6.4 Numerical and Parallelization Strategy

As the primary numerical solution method, the standard explicit 4^{th} order Runge-Kutta (RK4) method is implemented. The developed code allows to use any set of the parameters for a general RK4 method, but the classical method (c_1=1/2, c_2=1/2, c_3=1, a_{21}=1/2, a_{32}=1/2, a_{43}=1, b_1=1/6, b_2=1/3, b_3=1/3 and b_4=1/6, following Butcher's notation in Ref. [212]) has been applied for the ensuing examples in this study. The lower-order RK methods (1^{st}, 2^{nd} and 3^{rd}) are also optionally available for faster convergence at the expense of the numerical accuracy in case that prompt computation is desired. The governing equations (i.e., $6 \times N$ and N second-order differential equations for the metabeam and the 1D lattice, respectively) are recast into a state-space form (i.e., $12 \times N$ and $2 \times N$ first-order differential equations for the metabeam and the 1D lattice, respectively), where the new coordinate vector x contains pairs of the displacement and velocity vectors, $x_{2n-1} = u_n$ and $x_{2n} = \dot{u}_n$.

For better numerical stability, a 2^{nd} order implicit method is implemented as well. In this particular work, Newmark-β (NB) method with constant average acceleration (γ=1/2 ,

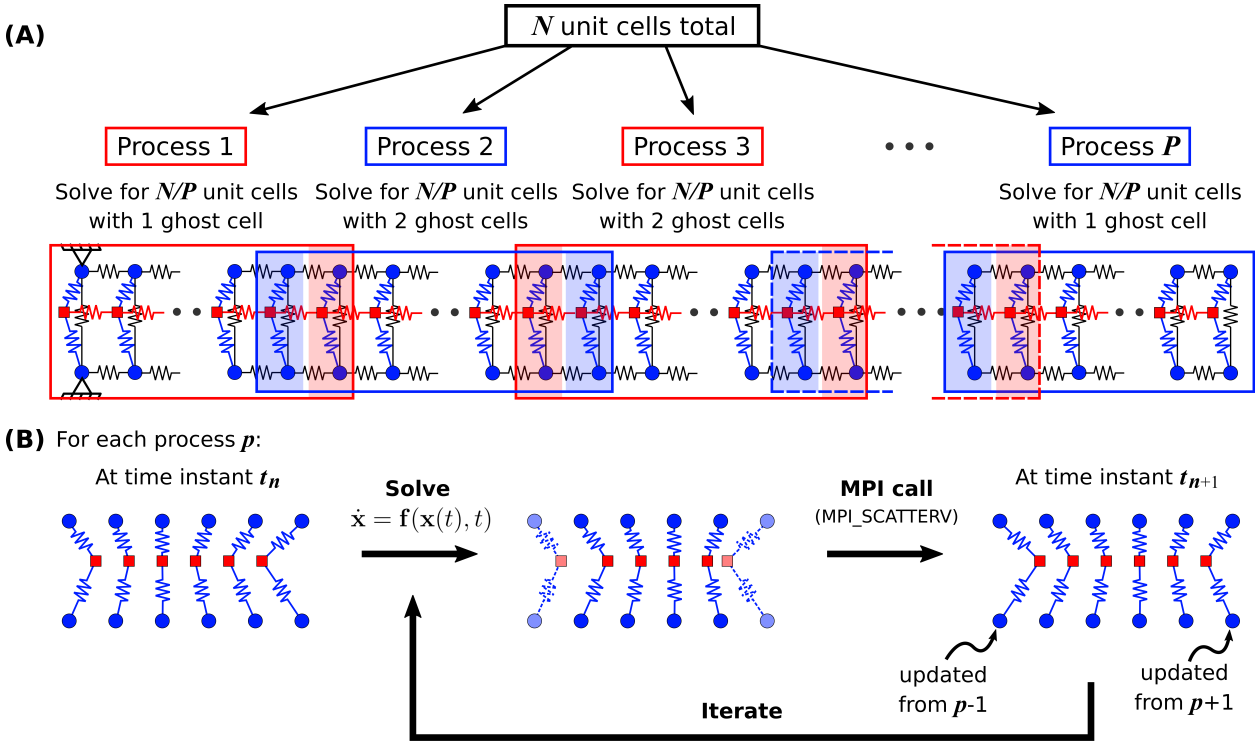

Figure 6.1. (A) Schematic representation of the domain-level parallelization scheme. Each process analyzes the elements in each boxed set only, and the elements in the shaded regions are ghost cells that need to be communicated between the neighboring processes. (B) Illustration of the solution algorithm for each process.

β=1/4) [169], which is unconditionally stable, is implemented to obtain numerical solutions. With NB method, matrix inversion operations are unavoidable during Newton-Raphson iterations. Since the tangent stiffness matrix $\hat{k} = \frac{\partial}{\partial u_n}[\mathcal{F}_{\text{intersite}}(u_{n-1}, u_n, u_{n+1}) + \mathcal{F}_{\text{onsite}}(u_n)]$ is sparse (at most 18 nonzero elements for each row) and large in its size, the conjugate gradient method is used for matrix inversion. For a parallel implementation of the conjugate gradient method, the block-decomposed vector algorithm [213] is adopted since the domain sizes are much larger than the number of the processes in most situations of interest.

The periodic repeating building blocks of the studied architectures provide an excellent framework for a parallelized computational model since the computational load can be evenly balanced. Since we deal with initial value problems, where the solutions are dependent on the previous time step(s) (single step for RK method and two steps for NB method), only the spatial-level parallelization can be achieved. To analyze problems with large numbers

of degrees of freedom, we adopt the message passing interface (MPI) standard to distribute the problem domain into multiple smaller subdomains to be handled by multiple individual processes in parallel. Starting with N unit cells of the global structure, the problem domain is divided into P smaller subdomains, where P is the number of compute processes. The unit cells are equally distributed such that each process computes N/P unit cells (assuming N is evenly divisible by P) as shown in Fig. 6.1(A). Each process, except the ones containing boundary elements, stores two additional unit cell data (ghost cells) to the left and right of the subdomain [the shaded regions in Fig. 6.1(A)] since the governing equation requires the states of the adjacent unit cells. An example algorithm for the parallel code with explicit methods is graphically illustrated in Fig. 6.1(B).

In order to reduce the latency from the overall data communications among the processes, the MPI calls are made as contiguous and invoked sparingly; for example, the number of the invoked communication calls for each iteration is twice the order of the numerical accuracy for the RK method. As the data storage format, HDF5 file format is chosen in the anticipation to use parallel I/O capability and to store extended metadata. The baseline output data structure is composed of an $Nt \times Nf$ input force array f, $Nt \times 1$ time array t, $Nt \times Nx$ displacement array u, $Nt \times Nx$ velocity array $\dot{u}$, and metadata containing the geometric and compositional information, where Nt, Nf, and Nx are the numbers of time steps, input sources, and degrees of freedom, respectively. For all the simulations to follow, the double-precision (64 bit in the tested environment) floating-point values are used for both the computation and data storage.

6.5 Code Validations

The responses of the metabeam under different levels of in-plane sinusoidal loads (applied at the leftmost unit cell) are compared with those from Abaqus simulations to validate the code. (The 1D lattices are validated with either Matlab or Python codes built for previous studies, as presented in SI.) Four example cases with different characteristic behaviors of the metabeam[205] are tested: linear behavior (0.1 N at 8 Hz), superharmonic generation (0.5 N at 76 Hz), frequency doubling (0.6 N at 96 Hz), and solitonic resonance (1.4 N at 35 Hz)

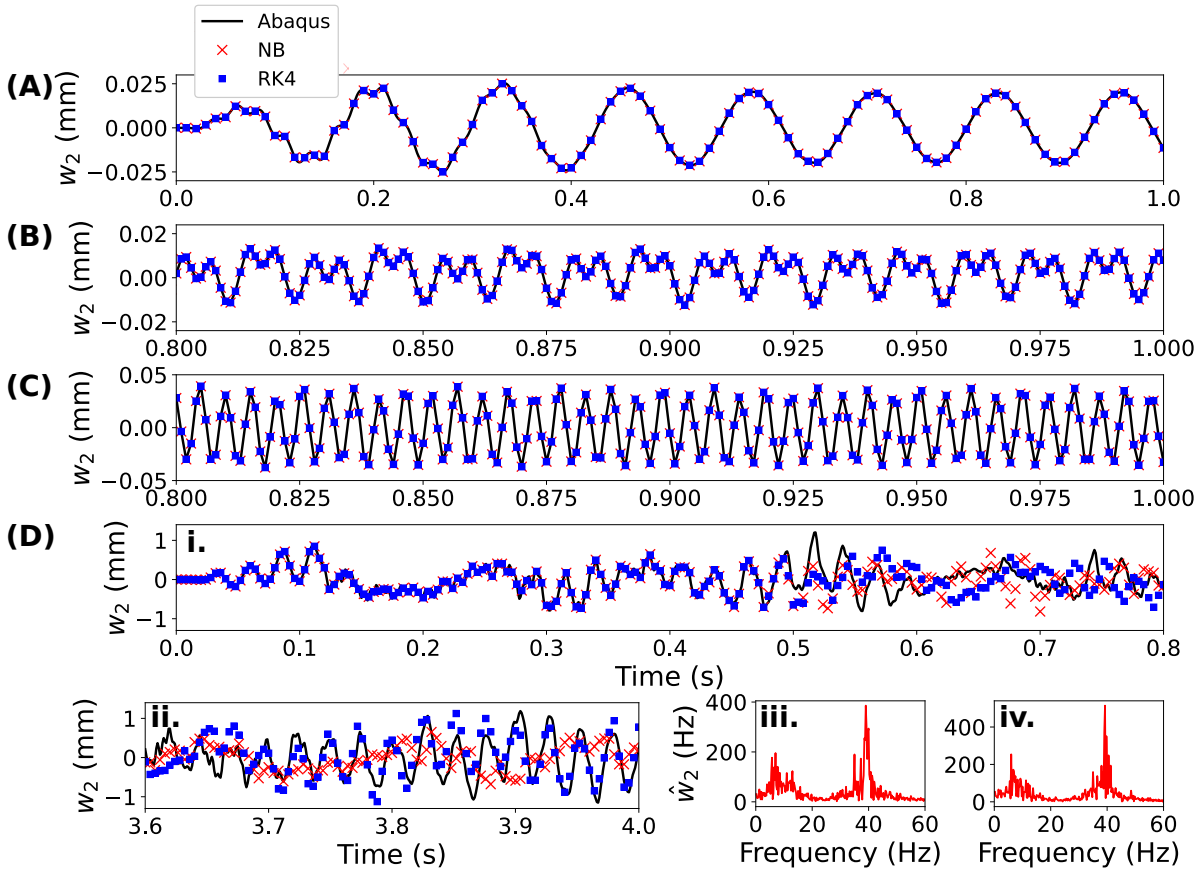

Figure 6.2. Comparison of the time responses obtained from Abaqus and the in-house code's NB and RK4 methods for representative (A) linear behavior (0.1 N at 8 Hz), (B) second harmonic generation (0.5 N at 76 Hz), (C) frequency doubling (0.6 N at 96 Hz), and (D-i) solitonic resonance (1.4 N at 35 Hz). (ii) The responses of the solitonic resonance at a later simulation time and their frequency spectra from (iii) Abaqus and (iv) RK4 method.

– see SI for the list of the design parameters. For all the example cases, the responses are simulated for 6 s at $\Delta t = 10^{-5}$ s.

Fig. 6.2 shows the transverse responses of the top mass at the rightmost unit of the metabeam. The blue dots and red crosses are the responses from RK4 and NB methods, respectively, which follow the black lines (obtained from Abaqus) almost exactly except the solitonic resonance example. The root-mean-square (RMS) errors of the time response between the solution sets from RK4 method and Abaqus are 1.206×10^{-6} mm (0.1 N at 8 Hz), 9.03×10^{-6} mm (0.5 N at 76 Hz), 3.81×10^{-5} mm (0.6 N at 96 Hz), and 4.71×10^{-1} mm (1.4 N at 35 Hz), respectively; those from NB method and Abaqus are 5.53×10^{-9}

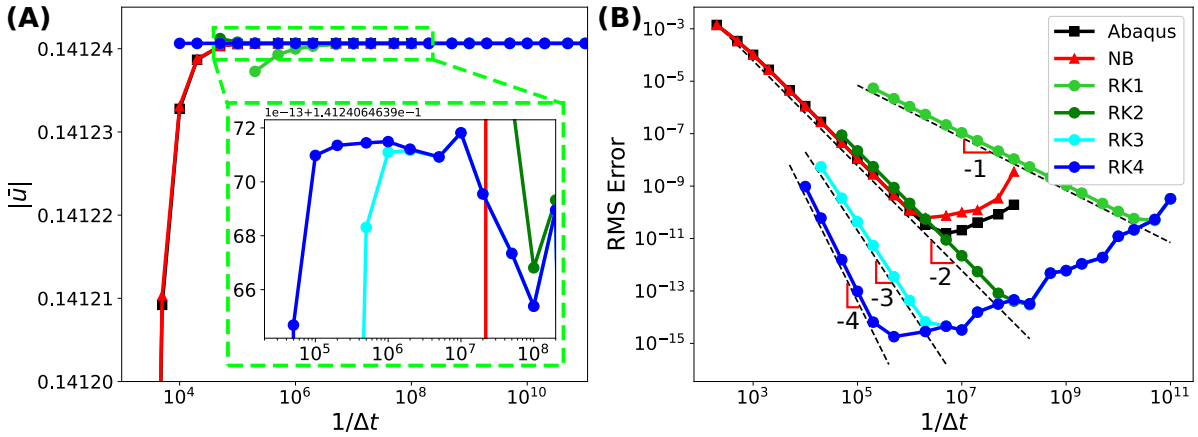

Figure 6.3. (A) Magnitude of the displacement vector, showing the solution convergence, and (B) the RMS error as a function of time step size for each of the numerical solution methods (Abaqus Implicit, NB, explicit RK1, explicit RK2, explicit RK3, explicit RK4), showing the global truncation errors.

mm (0.1 N at 8 Hz), 2.21×10^{-7} mm (0.5 N at 76 Hz), 7.50×10^{-7} mm (0.6 N at 96 Hz), and 5.18×10^{-1} mm (1.4 N at 35 Hz), respectively. The RMS errors for the three non-chaotic behaviors [Fig. D.1(A-C)] are minimal compared to the ranges of the output responses. On the other hand, the solitonic resonance [Fig. D.1(D)-i,ii] involves chaotic responses and thus the responses digress after several oscillations.[1] However, the crucial property of this metabeam is its input-independent characteristic of the output frequency when transition waves are generated within a metabeam. The frequency contents of the responses between 2-6 s are obtained using fftpack function from Python's scipy library at 1000 Hz sampling frequency without a window function. The general shapes of the output frequency spectra from Abaqus simulation [Fig. 6.2(D)-iii] and RK4 method [Fig. 6.2(D)-iv] show a good qualitative match, and the most dominant output frequencies occur at the same frequency (∼40Hz), confirming the validity of the implemented solution methods.

6.6 Numerical Performance

The default implicit Abaqus solver uses Hilber-Hughes-Taylor (HHT-alpha) method[214] to find solutions. The HHT-alpha method is a variant of the Newmark-β (NB) method and thus has the limit of the 2^{nd} order of global truncation error. With the flexibility in choosing the numerical solution methods in our in-house implementation, the solution accuracy can be extended to higher orders than the 2^{nd} order.

For each of the different numerical solution method, the various constant time steps between 5×10^{-3} and 10^{-11} are used to obtain the solutions for the example linear case in **Validation** section at the same time instant t=0.01 s. Since the exact theoretical solution is not available for this type of problem, the numerical solution obtained at one of the small time steps is assumed to be close to the exact solution set and used as a reference set to be compared. Due to the accumulation of round-off errors as approaching the machine's numerical precision limit, the time step cannot be reduced indefinitely to improve the solution accuracy. Since the implicit methods involve higher dimensional matrix operations (i.e. the matrix inversions during the Newton-Raphson iterations) and rely on the residual tolerance, the implicit methods is expected to be more susceptible to the machine's precision limit and thus ruled out from the choice. Hence, the reference solution set is selected by checking the convergence of the solutions from the RK methods as the time step is reduced. Figure 6.3(A) shows the magnitudes of the output displacement vectors at t=0.01 s, obtained with various time steps Δt's. The choice is made where the rate of the change of the magnitude is minimum, which is at $\Delta t = 10^{-6}$ with RK4 method [see the zoomed region of Fig. 6.3(A)].

The RMS errors between the solution sets obtained with the trial Δt and the reference solution set are plotted in a log-log scale in Fig. 6.3(B) for different solution methods (Abaqus Implicit, NB, explicit RK1, explicit RK2, explicit RK3, explicit RK4). The negative of the slope of the curve corresponds to the logarithm of the rate of decrease in the error with respect to decrease in the time step, hence mathematically indicating the global truncation error. The black dashed lines are the reference lines indicating the slopes of 1, 2, 3, and 4 in order,

[1]The chaotic motion is highly sensitive to any slight perturbations in the initial condition or intermediate values. The different numerical solution algorithms and parameters make it improbable to yield identical responses.

confirming the desired global truncation errors of the implemented solution methods. The accuracy of the in-house implementation of the NB method stays the same as that of Abaqus since the NB method is essentially the same as the default solution method that Abaqus uses. The small discrepancy in the achievable error is due to the different specification of the residual tolerance. With RK4 method, we observe a very fast convergence to the accurate solution as expected. A similar accuracy level that requires Abaqus simulation to be run with $\Delta t = 2 \times 10^{-7}$ can be achieved only with Δt greater than 5×10^{-5} for RK4 method. The resulting numerical accuracy plot confirms the extension of the solution accuracy to higher orders than what a commercial solver offers. The fast approach to the exact solution allows the solver to use a larger time step, making it less susceptible to the hardware precision error, which can be useful when solving stiff problems.

6.7 Computational Performance

The computational performance of our parallelized solver for bi-stable architectures is demonstrated by comparing the measured wallclock times obtained from the in-house solvers and Abaqus solver in solving both fixed-size problems (showing strong scaling) and scaled-size problems (showing weak scaling) with respect to the number of processes. For the analyses in this section, the same unit cell design as the linear behavior example in **Validation** section is used, and the responses are simulated for 0.1 s at Δt=0.0001 s. When measuring the wallclock times, file I/O statements have been disabled since the complete file I/O may not be necessary depending on the applications of the program (e.g., FFT of a single point), and one scheme can be faster than the others depending on the problem sizes (e.g., serial vs. parallel I/O schemes). Both for the NB and RK4 methods, the wallclock times are measured by comparing the time stamps from the MPI-intrinsic subroutine MPI_WTIME() placed before and after the main computation loop while all the hdf5 calls are commented out. For Abaqus simulations, the frequencies for the field and history output and restart request have been set to zeros, and the output diagnostics feature is disabled. The wallclock times from Abaqus simulations are directly read off from the generated .dat (or .msg) files. All the simulations are tested on dedicated compute nodes (Two Sky Lake CPUs at 2.6 GHz with

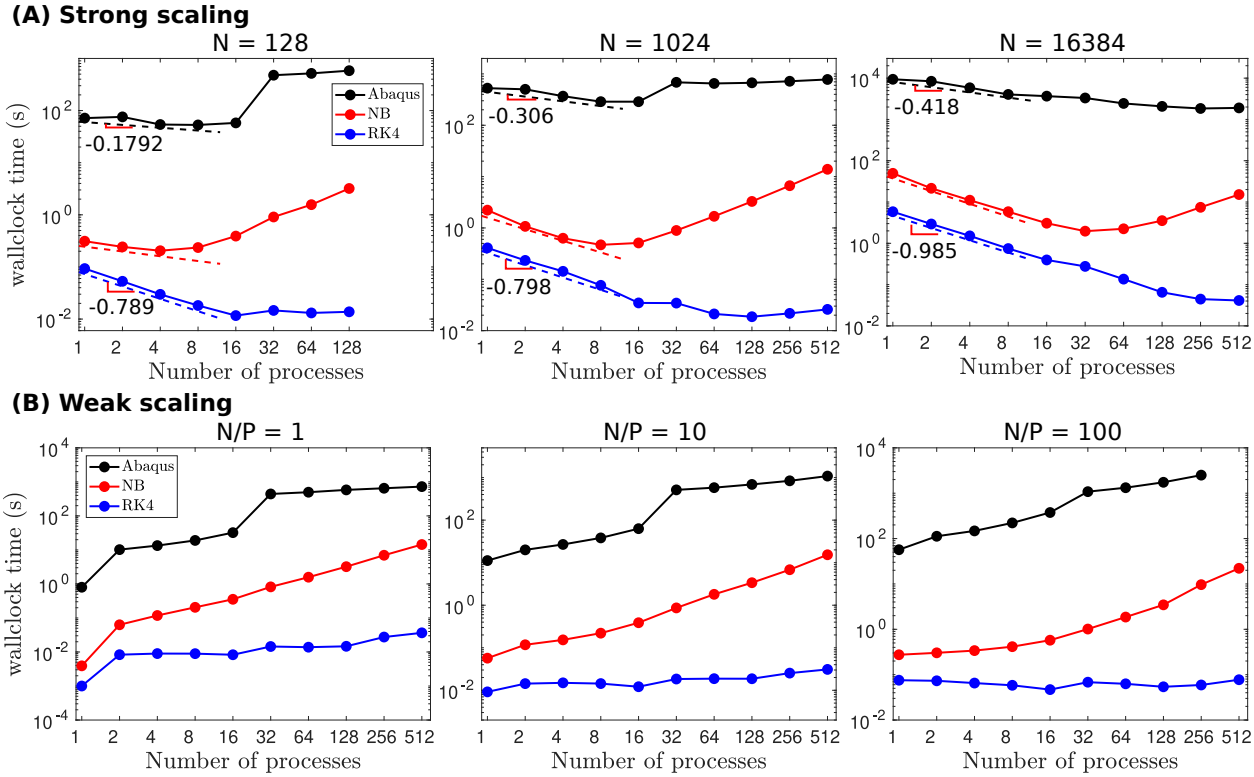

Figure 6.4. Wallclock time comparison among Abaqus Implicit solver and in-house code's NB and RK4 methods, showing the (A) strong and (B) weak scalings with the number of processes.

24 cores and 96 GB memory per node) at Purdue University, where no other user programs are running.

For the strong scaling analysis [215], three differently sized (128, 1024, and 16384 unit cells, each) metabeam problems are simulated with a varying number of processes. (To avoid any MPI load balancing issue, only the metabeams composed of power of 2 unit cells are tested for the power of 2 number of processes.) The wallclock times are measured three times for each solution method and each number of processes for a statistical purpose,[2] and their averages are plotted with respect to the number of processes in Fig. 6.4(A) on a log-log scale. Throughout all three problem sizes, the in-house RK4 solver exhibits absolute computation times about three orders of magnitude faster than those of the Abaqus solver. Since the code is streamlined to solve the particular type of problem, the absolute computation times

[2]Since the absolute time it takes for RK4 method is in general very quick (in ms scale), these results are more susceptible to hardware and software conditions, such as CPU temperature and background system processes.

from NB method are also faster than those from the Abaqus simulations. These results are by no means a fair comparison since Abaqus is a general-purpose commercial solver, which performs many cross-checks and other useful tasks nontransparent to the end-users. Moreover, Abaqus is not aware of the specific periodic arrangement of the structure, so that its native partitioning scheme may not be such that the best load balance is achieved. Hence, a better comparison measure is how the wallclock time scales with the increased number of the processes. To that end, the linear regression of the first three or four data points of the wallclock times for each method is plotted with the dashed line slightly beneath the corresponding curve. The slopes of the regressed lines [indicated by the dashed lines in Fig. 6.4(A)] immediately show that the computation times of the in-house code scales much better with the number of processes and more consistently throughout the problem sizes than those of Abaqus.

The weak scaling exhibits the best utilization of the available resources rather than a reduction in the absolute computation times with the increased number of processes [216]. For the weak scaling analysis, the problem size is proportionally scaled with the number of processes. For example, if we desire each process to compute 10 unit cells, we measure the wallclock times for a 10-unit cell metabeam with one process, a 20-unit cell metabeam with two processes, a 40-unit cell metabeam with four processes, and so forth. Figure 6.4(B) shows the weak scalings for the problem densities (N/P) of 1, 10, and 100 unit cells. The implementation of the explicit solution schemes do not contain inherently sequential tasks if the input processing is disregarded. Thus, the measured wallclock times from RK4 method for the scaled problem sizes remain nearly constant throughout the number processes. The slight increase is deemed to be from the latency of the underlying computer architecture's interconnection network scheme. For the implicit methods (Abaqus and NB), parallel implementation of matrix inversion is required, which is dependent on the global problem size (e.g., data communications need to be made among all the processes for the calculation of the residual sums), hence their weak scalabilities are not as balanced as that of RK4 method.

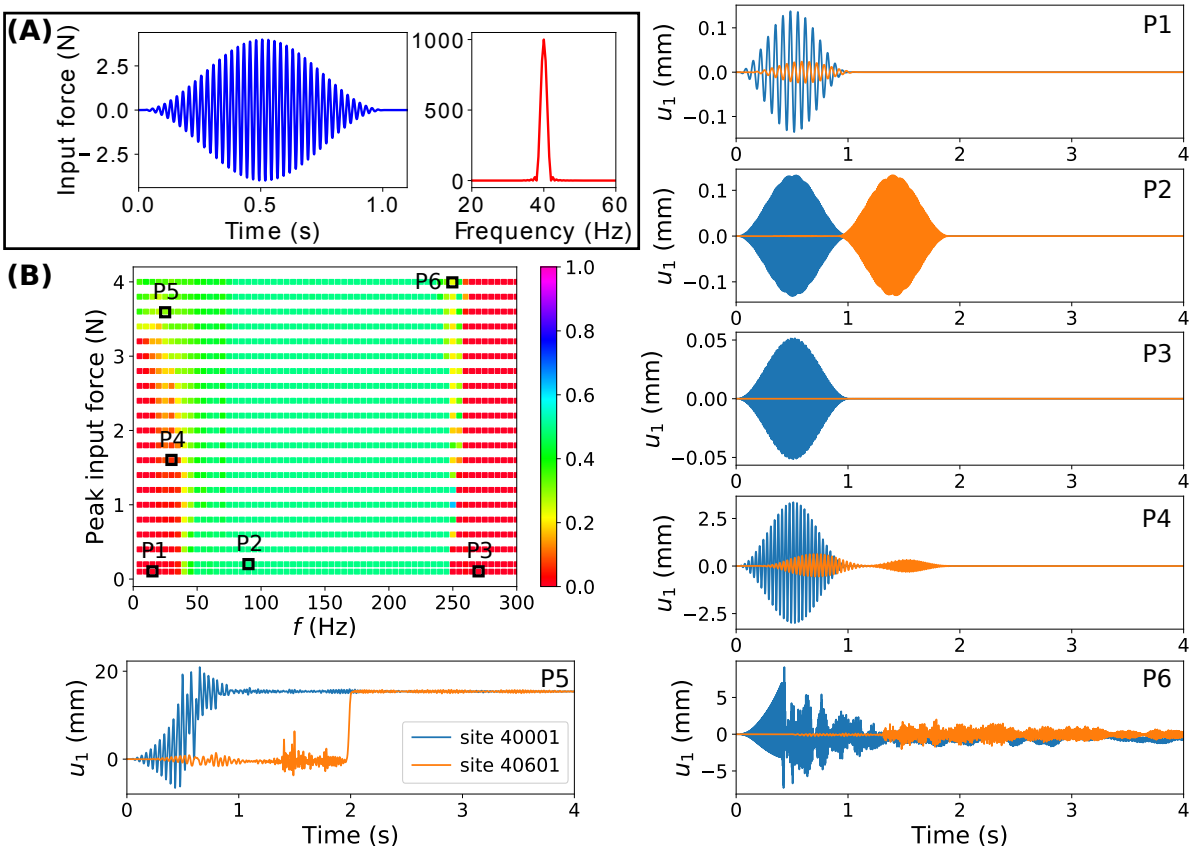

Figure 6.5. (A) Representative input force, localized both in temporal and spatial domains. (B) Energy flow diagram, showing the ratio between the transmitted energy to a distant site and the input energy. Around the diagram are the in-plane displacements at the excitation site (40,001$^{\text{st}}$ unit cell) and the measuring site (40,601$^{\text{st}}$ unit cell) for the selected forcing conditions.

6.8 Nonlinear Energy Flow Diagram of Bi-stable Metabeam

The improved computational capability from the massively parallelized spatial domain is especially useful to explore the nonlinear behaviors of periodic structures, for which the theoretical solutions are in general not available, enabling the previously unreachable analysis regime. As such an example, amplitude-dependent[3] energy propagation in a metabeam of bi-stable element is investigated. (An example case study on a 1D lattice can be found in SI.) To that end, a very long metabeam (N= 80,001) with a fixed-fixed boundary[4] is excited by a

[3]Although the constituting elements (springs) are linear, the unit cell geometry involves angular dependence, and thus the structural responses are dictated by the amplitude-dependent dynamics.
[4]The choice of boundary condition is irrelevant since we are only interested in the propagation characteristics. The simulation time is limited such that major reflections are yet to occur.

modulated sinusoidal force of the form $f_{in} = F\sin(\omega t + \phi_0)\sin^2(\frac{t-c_1}{c_2-c_1})$ for $c_1 \leq t \leq c_2$ at the center mass of 40,001st unit cell of the metabeam in the in-plane direction. A representative input signal is shown in Fig. 6.5(A), where the values for c_1 (10 ms) and c_2 (1010 ms) are chosen such that the signal is localized in both time and frequency domains of interest. Small mass proportional damping that gradually increases from 6.61×10^{-8} s^{-1} to 2.64×10^{-4} s^{-1} is applied at both the leftmost and rightmost 2000 unit cells to eliminate unphysically fast low-frequency waves reflecting back toward the origin.

To quantify the energy propagation in the metabeam, we define energy transmissibility[5] as the ratio between the energy transmitted to the measuring site (a distant location from the input site) and the input energy into the system with – see *Method* section for the details of calculating the transmissibility. Figure 6.5(B) summarizes the energy transmissibility for various combinations of the input force and frequency. Note that the transmissibility, in general, does not exceed 50% since the metabeam is symmetrically excited at the midpoint, making the waves travel both to the left and right. Thus, the closer the color is to green (red), the more (less) input energy survives through the measuring site. In the sense that the transmissibility shows how much of the original energy can be transferred to a distant location, it can be regarded as a practical measure of the pass or stop bands. Several representative time responses of the waves at the excitation and measuring sites are plotted as well. Case P1 shows the spatial attenuation, a typical characteristic when the associated wavenumber has a nonzero imaginary part. P2 exhibits the undisturbed transmission of the input pulse through the metabeam, while P3 exhibits the stop band behavior. P4 shows the separation into two pulse groups, the details of which is addressed shortly. For a large enough forcing amplitude, we observe the formation of transition waves (P5) or transformation into nondefinite waveforms (P6).

From the energy transmission diagram, We can immediately observe the overall effect of the amplitude dependence on the energy propagation: the pass band expands with the increased forcing amplitude. What is more incredible than the observed dynamics is that the

[5]The reason why the energy flow is considered as the wave propagation measure rather than the shape of the wave pulse itself is that the characteristics of the waves change depending on the forcing amplitude; for example, the propagated pulse does not retain the original modulated sinusoidal input for cases P4, P5, and P6 in Fig. 6.5(B).

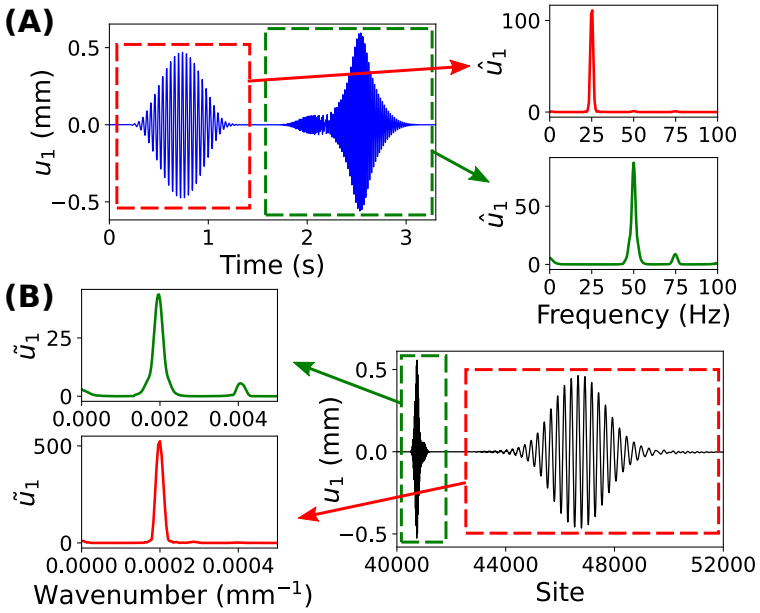

Figure 6.6. Separation of the input pulse into multiple pulses under F=1.8 N at 25 Hz. In-plane responses u_1 are plotted both in (A) time domain and (B) spatial domain along with the corresponding temporal frequency $\hat{u}_1$ and spatial frequency $\tilde{u}_1$ of each pulse group.

obtained diagram is an epitome of what a massively parallelized numerical solver enables. Every square in the energy flow diagram represents the individual simulation of a metabeam with 80,001 unit cells (480,006 DoF's). In generating a single set of the energy flow diagram, 1,260 simulations of such models are performed, a scale of which has not been previously conceivable with a serial implementation or with commercial solvers.

Strictly speaking, a very large spatial domain is not a necessity to obtain the energy flow diagram above. The same diagram can be obtained for a structure long enough to cover the measuring site with proper terminating conditions (e.g., artificial damping) at the boundaries since only the time data passing through the specific point of interest is required to calculate the transmitted energy. However, we can obtain information about the associated waves in its entirety with the additional solution dimension in the spatial domain. When the forcing amplitude is moderately high,[6] we observe that the input pulse separates into multiple pulses near the boundary of the low-frequency stop band and the pass band

[6]The term moderate in this context is used to describe the large enough force to exhibit nonlinear behaviors but not large enough to trigger transition waves.

[e.g., the case P4 in Fig. 6.5(B)]. One such phenomenon occurs under F=1.8 N at 25Hz, and the corresponding time response at 41001st site is plotted in Fig. 6.6(A). We can identify two main pulse groups.[7] The dominant frequency of the former is the same as the carrier frequency, and the dominant frequency of the latter is twice the carrier frequency, showing the generation of the harmonic contributions to the main input frequency.

Since our parallel solver allows for efficient analyses of very large spatial domains, the corresponding wavenumber to each pulse group can also be identified from the analysis of waveform in the space configuration. Fig. 6.6(B) shows the responses in the space configuration, obtained at t=2 s. The same pulse groups are indicated by the same colors in Figs. 6.6(A,B) (red dashed box for the fast-moving pulse and green dashed box for the slow-moving pulse). We take FFT on each pulse in the space configuration to extract spatial frequency spectrum, yielding ν=$\sim$0.0002 m^{-1} for 25 Hz pulse and ν=$\sim$0.002 m^{-1} for 50 Hz pulse. By collecting the wavefrequency-wavenumber pairs for each input excitation, it is potentially possible to construct numerically a nonlinear dispersion relation, which fundamentally governs most of the dynamic behaviors yet is deemed impossible to obtain analytically for this kind of complex metastructure designs.

6.9 Conclusions

In summary, we adopt a message-passing model to achieve massively parallelized computation for dynamics in bi-stable architectures. The implemented solution tools are thoroughly validated against the existing solvers. The freedom of choice on the numerical solution schemes allows the global truncation error to be extended to higher orders, surpassing the 2nd order accuracy limit posed by implicit Abaqus solver. The increased accuracy opens up a possibility for the code to be readily coupled with the existing high-fidelity solvers in other dynamical systems (e.g., hypersonic flow analysis tools), providing solutions to more complex problems. Since the code is dedicated to solving the multi-stable architectures, the computation time can be reduced to as much as three orders of magnitude compared to that of

[7] To be precise, the second group itself is composed of two separate identifiable subgroups. Since one of the subgroups dominates the other, we disregard such a detailed description of the pulses for analytical simplicity.

the commercial solver. Additionally, the studied architectures' inherent periodicity provides an excellent framework for balanced computational loads among the processes, achieving a strong scaling with the number of processes. The improved computational performance makes the code suitable for analyzing a large number of large-scale problems expeditiously as well as investigating previously unreachable analysis regimes – the generated nonlinear energy transmissibility diagram showcases one such example. The presented case studies are only a small fraction of what this parallel implementation can potentially enable. Typically, more practical designs require a higher level of design complexity, for which analytical means to investigate their dynamics become unmanageable. The implemented computational design is generally applicable to and thus easily extendable to any dynamical systems with the structural dimensionality of 1 as long as the governing equations and their Jacobians (for implicit numerical methods) are available. Hence, our code can provide an excellent numerical alternative to investigate such previously unreachable analysis regimes.

6.10 Methods

6.10.1 Running MPI Jobs

The parallel Fortran script is first compiled with an MPI Fortran wrapper compiler (Intel MPI library 2017 Update 1 is used throughout the examples in this study). The input parameters for the numerical solution method and the bi-stable architecture design are then stored in a python script. Running the python script generates two input files (one defining the numerical solution method and the other defining the structural design), which can be read by the Fortran program. This entire process is automated through GNU make; a single analysis is typically performed by executing a sequence of commands "make" and "make run np=(number of processes) inp=(input generation file name)" in a command line interface. All the scripts are available in the supplemented .zip file.

6.10.2 Energy Flow Diagram

The energy transmissibility in this study is defined as the ratio between the transmitted energy to a distant site and the input energy to the system; that is, TR = $E_{\mathrm{tr}}/E_{\mathrm{in}}$. For

the energy flow example in the main manuscript, only the vector component in the in-plane direction is considered to investigate the pass/stop band characteristics in the in-plane direction. Hence, the input energy E_{in} is obtained from the time integration of the instantaneous power supplied to the excitation site in the in-plane direction: $E_{\text{in}} = \int_0^\infty f_{\text{in}} \dot{u}_{\text{in}} dt$, where f_{in} is the input force, $\dot{u}_{\text{in}}$ is the velocity of the excited mass in the in-plane direction, and the integrand is assumed to well-behave.

Similarly, the transmitted energy to the mass of interest is obtained by integrating the power supplied to the mass of the interest from the left (for a right-propagating wave). The force transmitted through the inter-site spring left of the mass of interest is

$$f_{\text{left}} = \frac{\partial}{\partial u_{1,\text{out}}} \left(\frac{1}{2} k_1 \Delta_{1,\text{out}}^2 \right), \tag{6.2}$$

where $u_{1,\text{out}}$ is the in-plane displacement of the center mass at the measuring site, and $\Delta_{1,\text{out}}$ is the deflection of the inter-site spring (with the stiffness k_1) connected to the left of the mass – the full expression for the spring defection can be found in Ref. [205]. Thus, the transmitted energy can be calculated as $E_{\text{tr}} = \int_0^\infty f_{\text{left}} \dot{u}_{\text{out}} dt$.

6.10.3 Linear Regression

The approximate slopes of the wallclock time curves in Fig. 6.4 are obtained by finding the linear fits of the first four data points. Since the plots are in log-log scales, the approximate relationship is in the form $\log t_{\text{WC},p} = a_0 + a_1 \log p$ (equivalent to $t_{\text{WC},p} = 10^{a_0} p^{a_1}$), where $t_{\text{WC},p}$ is the wallclock time corresponding to the number of the processes p. To solve for a set of the approximate values for constants a_0 and a_1, an overdetermined system of equations can be formed as follows:

$$\underbrace{\begin{pmatrix} 1 & \log 1 \\ 1 & \log 2 \\ 1 & \log 4 \\ 1 & \log 8 \end{pmatrix}}_{A} \begin{pmatrix} a_0 \\ a_1 \end{pmatrix} = \begin{pmatrix} \log t_{\text{WC},1} \\ \log t_{\text{WC},2} \\ \log t_{\text{WC},4} \\ \log t_{\text{WC},8} \end{pmatrix}. \tag{6.3}$$

By premultiplying both sides of Eq. (6.3) by A, we can find a_0 and a_1 that best fit the measured time data.

7. CONCLUSION

In this thesis, we study rich nonlinear dynamics in generic architectures composed of bistable unit cells. In particular, the strong nonlinearities of the bistable building blocks yield highly stable propagation of energy in the form of transition waves. The particle-like nature of the transition waves provides a fundamentally different route to realizing dynamic properties, breaking their strong dependence on the unit cell size. Therefore, metamaterials based on bistable unit cells can potentially address the existing performance limits of the linear counterparts. The uncovered metamaterial properties are not limited to specific designs or implementation and thus can be applied to various fields of physics and engineering.

To leverage the quasi-particle nature of the transition waves, we investigate the dynamic responses of the lattices composed of asymmetric bistable unit cells, which support unidirectional transition waves. We observe numerically and experimentally that invariant transition waves are generated regardless of the type and the intensity of the input excitations as long as any unit cells undergo snap-through state transitions. Due to the inherent lattice discreteness, there is a radiation of energy in the form of small vibrations tailing the main transition waves. The fact that these tailing vibrations are dominantly at single frequencies ensures resonant transduction of the mechanical energy into electrical energy, providing means to utilize the highly concentrated energy of the transition waves. Therefore, combined with the input-independent characteristics, the studied bistable lattices can provide a solution to the current challenges of broadband energy harvesting.

To improve the power conversion potential in energy harvesters based on bistable lattices, we introduce engineered defects and lattice discreteness. Perturbations in the forms of mass and stiffness defects are incorporated, exhibiting wave energy concentration at specific sites within the lattice. With a section of defects, we observe a breather-like mode having a long-lived, large oscillatory motion between two stable states, which can further improve the harvesting performance. Alternatively, the motion of the transducible tails resulting from the passage of transition waves can be enhanced as a whole across the lattice by manipulating the lattice discreteness. To that end, a set of inertially and elastically equivalent bistable lattices that only differs in lattice discreteness are prepared. We observe the lower

and upper energy harvesting gaps, arising from the vanishing tails and transition wave disintegration, respectively. In between is the pass band, where the available kinetic energy of the transducible tail amplifies with the level of the lattice discreteness.

Despite the unique dynamics in the bistable lattices, the asymmetry in the bistable onsite potentials hinders continuous operations without proper resetting mechanisms. To address this challenge, we impose graded stiffness on either the onsite or inter-site elements of the bistable lattices with symmetric onsite potentials. With gradually decreasing stiffness, the generated transition waves still travel unidirectionally. However, they can now be triggered in both directions since the system supports both compression and rarefaction transition waves. With gradually increasing stiffness, a boomerang-like transition wave reversal occurs, which can be useful for energy harvesting applications that require impulsive input sources, such as human walks and blasts. This added operational degree of freedom helps expand the utility of transition waves in real-world applications.

The input-independent dynamics exist at the unit cell level in the one-dimensional bistable lattices. By allowing macroscopic extensional and flexural motions of the lattices, we can translate the input-independent behaviors to occur at the macroscopic structural level. To that end, a metabeam is formed by integrating a spring-joined bistable lattice into a flexible macroscopic frame. The metabeam is excited by a unit cell level disturbance, and the responses are measured at the macrostructural level. We obtain an output frequency diagram, showing that the dominant output frequencies are coherent around the macroscopic structural modes regardless of input excitations as long as transition waves are generated by any means. This extreme energy transfer not only implies potential applications in broadband operations but also provides a transformative route to metamaterial design by breaking the dependence on the constitutive units. Furthermore, the simple metamaterial building blocks allow the input and output frequency ranges to be easily tailored by manipulating the mass and spring constants of the unit cells; we demonstrate energy transfer between frequencies up to two orders of magnitude apart.

Finally, we develop a dedicated Fortran code that utilizes the message-passing interface (MPI) for parallel computation of generic problems involving bistable unit cells. The code is thoroughly validated with the results from Abaqus and well-established computer codes.

The implemented fully explicit 4^{th}-order Runge-Kutta method outperforms the commercial solvers both in numerical accuracy and computational speed. In particular, the intrinsic periodicity of a lattice structure guarantees the optimal computational load balance among the processes, achieving extreme computational scaling with the increased number of processes. The resulting performance gain enables the simulations of massively large problems and opens up the possibility to uncover interesting dynamics in previously inaccessible analysis regimes.

In summary, the presented results in this thesis demonstrate transition wave generations in metamaterial architectures of bistable units and their extreme dynamic properties. In particular, this work introduces a new design paradigm for metamaterials and metastructures by exploiting the quasi-particle nature of the strongly nonlinear waves as a fundamental mechanism to dictate the macroscopic dynamics. The established dynamics and mechanisms in this work can address many of the current challenges with engineering materials and provide the potential to reveal even more interesting new dynamics.

REFERENCES

[1] R. Martínez-Sala, J. Sancho, J. V. Sánchez, V. Gómez, J. Llinares, and F. Meseguer, "Sound attenuation by sculpture," *Nature*, vol. 378, no. 6554, pp. 241–241, Nov. 1995. DOI: 10.1038/378241a0.

[2] Z. Liu, X. Zhang, Y. Mao, Y. Y. Zhu, Z. Yang, C. T. Chan, and P. Sheng, "Locally resonant sonic materials," *Science (New York, N.Y.)*, vol. 289, no. 5485, pp. 1734–6, 2000. DOI: 10.1126/science.289.5485.1734.

[3] N. I. Zheludev, "The Road Ahead for Metamaterials," *Science*, vol. 328, no. 5978, pp. 582–583, Apr. 2010. DOI: 10.1126/science.1186756.

[4] M. I. Hussein, M. J. Leamy, and M. Ruzzene, "Dynamics of Phononic Materials and Structures: Historical Origins, Recent Progress, and Future Outlook," *Applied Mechanics Reviews*, vol. 66, no. 4, p. 040 802, Jul. 2014. DOI: 10.1115/1.4026911.

[5] G. Ma and P. Sheng, "Acoustic metamaterials: From local resonances to broad horizons," *Science Advances*, vol. 2, no. 2, e1501595, Feb. 2016. DOI: 10.1126/sciadv.1501595.

[6] M. Ashby, *Materials selection in mechanical design: Fourth edition*. 2010.

[7] R. Lakes, "Foam Structures with a Negative Poisson's Ratio," *Science*, vol. 235, no. 4792, pp. 1038–1040, Feb. 1987. DOI: 10.1126/science.235.4792.1038.

[8] K. E. Evan, M. A. Nkansah, I. J. Hutchinson, and S. C. Rogers, "Molecular network design," *Nature*, vol. 353, no. 6340, pp. 124–124, Sep. 1991. DOI: 10.1038/353124a0.

[9] X. Ren, R. Das, P. Tran, T. D. Ngo, and Y. M. Xie, "Auxetic metamaterials and structures: A review," *Smart Materials and Structures*, vol. 27, no. 2, 2018. DOI: 10.1088/1361-665X/aaa61c.

[10] R. Lakes, "Cellular solids with tunable positive or negative thermal expansion of unbounded magnitude," *Applied Physics Letters*, vol. 90, no. 22, p. 221 905, May 2007. DOI: 10.1063/1.2743951.

[11] Q. Wang, J. A. Jackson, Q. Ge, J. B. Hopkins, C. M. Spadaccini, and N. X. Fang, "Lightweight Mechanical Metamaterials with Tunable Negative Thermal Expansion," *Physical Review Letters*, vol. 117, no. 17, p. 175 901, Oct. 2016. DOI: 10.1103/PhysRevLett.117.175901.

[12] J. Qu, M. Kadic, A. Naber, and M. Wegener, "Micro-Structured Two-Component 3D Metamaterials with Negative Thermal-Expansion Coefficient from Positive Con-

stituents," *Scientific Reports*, vol. 7, no. 1, p. 40 643, Feb. 2017. DOI: 10.1038/srep40643.

[13] W. J. Padilla, D. N. Basov, and D. R. Smith, "Negative refractive index metamaterials," *Materials Today*, vol. 9, no. 7-8, pp. 28–35, Jul. 2006. DOI: 10.1016/S1369-7021(06)71573-5.

[14] H. H. Huang, C. T. Sun, and G. L. Huang, "On the negative effective mass density in acoustic metamaterials," *International Journal of Engineering Science*, vol. 47, no. 4, pp. 610–617, 2009. DOI: 10.1016/j.ijengsci.2008.12.007.

[15] D. R. Smith, W. J. Padilla, D. C. Vier, S. C. Nemat-Nasser, and S. Schultz, "Composite medium with simultaneously negative permeability and permittivity," *Physical Review Letters*, 2000. DOI: 10.1103/PhysRevLett.84.4184.

[16] M. Sigalas and E. Economou, "Elastic and acoustic wave band structure," *Journal of Sound and Vibration*, vol. 158, no. 2, pp. 377–382, Oct. 1992. DOI: 10.1016/0022-460X(92)90059-7.

[17] M. S. Kushwaha, "Classical Band Structure of Periodic Elastic Composites," *International Journal of Modern Physics B*, vol. 10, no. 09, pp. 977–1094, Apr. 1996. DOI: 10.1142/S0217979296000398.

[18] N. Fang, "Sub-Diffraction-Limited Optical Imaging with a Silver Superlens," *Science*, vol. 308, no. 5721, pp. 534–537, Apr. 2005. DOI: 10.1126/science.1108759.

[19] J. B. Pendry, D. Schurig, and D. R. Smith, "Controlling electromagnetic fields," *Science*, 2006. DOI: 10.1126/science.1125907.

[20] D. A. B. Miller, "On perfect cloaking," *Optics Express*, vol. 14, no. 25, p. 12 457, Dec. 2006. DOI: 10.1364/OE.14.012457.

[21] G. W. Milton, M. Briane, and J. R. Willis, "On cloaking for elasticity and physical equations with a transformation invariant form," *New Journal of Physics*, vol. 8, no. 10, pp. 248–248, Oct. 2006. DOI: 10.1088/1367-2630/8/10/248.

[22] S. H. Simon, *The Oxford Solid State Basics*. OUP Oxford, 2013.

[23] Z. Liu, C. T. Chan, and P. Sheng, "Three-component elastic wave band-gap material," *Physical Review B - Condensed Matter and Materials Physics*, vol. 65, no. 16, pp. 1 651 161–1 651 166, 2002. DOI: 10.1103/PhysRevB.65.165116.

[24] M. S. Kushwaha, "Stop-bands for periodic metallic rods: Sculptures that can filter the noise," *Applied Physics Letters*, vol. 70, no. 24, pp. 3218–3220, 1997. DOI: 10.1063/1.119130.

[25] A. Ludu and P. Kevrekidis, "Nonlinear dispersion relations," *Mathematics and Computers in Simulation*, vol. 74, no. 2-3, pp. 229–236, Mar. 2007. DOI: 10.1016/j.matcom.2006.10.003.

[26] R. K. Narisetti, M. J. Leamy, and M. Ruzzene, "A perturbation approach for predicting wave propagation in one-dimensional nonlinear periodic structures," *Journal of Vibration and Acoustics, Transactions of the ASME*, vol. 132, no. 3, pp. 0 310 011–03 100 111, 2010. DOI: 10.1115/1.4000775.

[27] R. K. Narisetti, M. Ruzzene, and M. J. Leamy, "A Perturbation Approach for Analyzing Dispersion and Group Velocities in Two-Dimensional Nonlinear Periodic Lattices," *Journal of Vibration and Acoustics*, vol. 133, no. 6, pp. 1–12, Dec. 2011. DOI: 10.1115/1.4004661.

[28] M. H. Abedinnasab and M. I. Hussein, "Wave dispersion under finite deformation," *Wave Motion*, vol. 50, no. 3, pp. 374–388, 2013. DOI: 10.1016/j.wavemoti.2012.10.008.

[29] R. Khajehtourian and M. I. Hussein, "Dispersion characteristics of a nonlinear elastic metamaterial," *AIP Advances*, vol. 4, no. 12, 2014. DOI: 10.1063/1.4905051.

[30] Y. Xia, M. Ruzzene, and A. Erturk, "Dramatic bandwidth enhancement in nonlinear metastructures via bistable attachments," *Applied Physics Letters*, vol. 114, no. 9, p. 093 501, Mar. 2019. DOI: 10.1063/1.5066329.

[31] M. Remoissenet, *Waves Called Solitons*, 3rd ed., ser. Advanced Texts in Physics. Berlin, Heidelberg: Springer Berlin Heidelberg, 1999. DOI: 10.1007/978-3-662-03790-4.

[32] A. C. Scott, "A Nonlinear Klein-Gordon Equation," *American Journal of Physics*, vol. 37, no. 1, pp. 52–61, 1969. DOI: 10.1119/1.1975404.

[33] N. J. Zabusky and M. D. Kruskal, "Interaction of "Solitons" in a Collisionless Plasma and the Recurrence of Initial States," *Physical Review Letters*, vol. 15, no. 6, pp. 240–243, Aug. 1965. DOI: 10.1103/PhysRevLett.15.240.

[34] J. W. Miles, "The Korteweg-de Vries equation: A historical essay," *Journal of Fluid Mechanics*, vol. 106, no. 2, pp. 131–147, 1981. DOI: 10.1017/S0022112081001559.

[35] I. G. Main, *Vibrations and Waves in Physics*. Cambridge University Press, Jul. 1993. DOI: 10.1017/CBO9781139170567.

[36] M. J. Ablowitz, D. J. Kaup, A. C. Newell, and H. Segur, "Method for Solving the Sine-Gordon Equation," *Physical Review Letters*, vol. 30, no. 25, pp. 1262–1264, Jun. 1973. DOI: 10.1103/PhysRevLett.30.1262.

[37] R. Hirota, "Exact envelope-soliton solutions of a nonlinear wave equation," *Journal of Mathematical Physics*, vol. 14, no. 7, pp. 805–809, Jul. 1973. DOI: 10.1063/1.1666399.

[38] J. Weiss, "The sine-Gordon equations: Complete and partial integrability," *J. Math. Phys.*, vol. 25, no. 7, pp. 2226–2235, 1984. DOI: 10.1063/1.526415.

[39] G. B. Whitham, *Linear and Nonlinear Waves*. Hoboken, NJ, USA: John Wiley & Sons, Inc., Jun. 1999. DOI: 10.1002/9781118032954.

[40] T. Aktosun, F. Demontis, and C. van der Mee, "Exact solutions to the sine-Gordon equation," *Journal of Mathematical Physics*, vol. 51, no. 12, 2010. DOI: 10.1063/1.3520596.

[41] A. Hasegawa and F. Tappert, "Transmission of stationary nonlinear optical pulses in dispersive dielectric fibers. II. Normal dispersion," *Applied Physics Letters*, vol. 23, no. 4, pp. 171–172, 1973. DOI: 10.1063/1.1654847.

[42] L. F. Mollenauer, R. H. Stolen, and J. P. Gordon, "Experimental Observation of Picosecond Pulse Narrowing and Solitons in Optical Fibers," *Physical Review Letters*, vol. 45, no. 13, pp. 1095–1098, Sep. 1980. DOI: 10.1103/PhysRevLett.45.1095.

[43] D. Cutting, M. Hindmarsh, and D. J. Weir, "Gravitational waves from vacuum first-order phase transitions: From the envelope to the lattice," *Physical Review D*, vol. 97, no. 12, p. 123 513, 2018. DOI: 10.1103/PhysRevD.97.123513.

[44] S. Yomosa, "Soliton excitations in deoxyribonucleic acid (DNA) double helices," *Physical Review A*, vol. 27, no. 4, pp. 2120–2125, 1983. DOI: 10.1103/PhysRevA.27.2120.

[45] T. Dauxois and M. Peyrard, *Physics of Solitons*. Cambridge University Press, 2006.

[46] L. I. Manevich, A. V. Savin, V. V. Smirnov, and S. Volkov, "Solitons in nondegenerate bistable systems," *Uspekhi Fizicheskih Nauk*, vol. 164, no. 9, p. 937, 1994. DOI: 10.3367/UFNr.0164.199409b.0937.

[47] A. Cherkaev, E. Cherkaev, and L. Slepyan, "Transition waves in bistable structures. I. Delocalization of damage," *Journal of the Mechanics and Physics of Solids*, vol. 53, no. 2, pp. 383–405, Feb. 2005. DOI: 10.1016/j.jmps.2004.08.002.

[48] N. Nadkarni, C. Daraio, and D. M. Kochmann, "Dynamics of periodic mechanical structures containing bistable elastic elements: From elastic to solitary wave propagation," *Physical Review E*, vol. 90, no. 2, p. 023 204, Aug. 2014. DOI: 10.1103/PhysRevE.90.023204.

[49] S. Katz and S. Givli, "Solitary waves in a bistable lattice," *Extreme Mechanics Letters*, vol. 22, pp. 106–111, Jul. 2018. DOI: 10.1016/j.eml.2018.06.003.

[50] T. Kontorova and J. Frenkel, "On the theory of plastic deformation and twinning. II.," *Zh. Eksp. Teor. Fiz.*, 1938.

[51] R. Peierls, "The size of a dislocation," *Proceedings of the Physical Society*, vol. 52, no. 1, pp. 34–37, 1940. DOI: 10.1088/0959-5309/52/1/305.

[52] F. R. N. Nabarro, "Dislocations in a simple cubic lattice," *Proceedings of the Physical Society*, vol. 59, no. 2, pp. 256–272, Mar. 1947. DOI: 10.1088/0959-5309/59/2/309.

[53] R. Hobart and V. Celli, "A solution to the frenkel-kontorova dislocation model," *Journal of Applied Physics*, vol. 33, no. 1, pp. 60–62, 1962. DOI: 10.1063/1.1728528.

[54] R. Hobart, "Peierls-barrier minima," *Journal of Applied Physics*, vol. 36, no. 6, pp. 1948–1952, 1965. DOI: 10.1063/1.1714380.

[55] R. Hobart, "Peierls barrier analysis," *Journal of Applied Physics*, vol. 37, no. 9, pp. 3573–3576, 1966. DOI: 10.1063/1.1708904.

[56] J. A. Krumhansl and J. R. Schrieffer, "Dynamics and statistical mechanics of a one-dimensional model Hamiltonian for structural phase transitions," *Physical Review B*, vol. 11, no. 9, pp. 3535–3545, 1975. DOI: 10.1103/PhysRevB.11.3535.

[57] S. Burger, K. Bongs, S. Dettmer, W. Ertmer, K. Sengstock, A. Sanpera, G. V. Shlyapnikov, and M. Lewenstein, "Dark solitons in bose-einstein condensates," *Physical Review Letters*, vol. 83, no. 25, pp. 5198–5201, 1999. DOI: 10.1103/PhysRevLett.83.5198.

[58] J. Denschlag, "Generating Solitons by Phase Engineering of a Bose-Einstein Condensate," *Science*, vol. 287, no. 5450, pp. 97–101, Jan. 2000. DOI: 10.1126/science.287.5450.97.

[59] J. L. Hammack and H. Segur, "The Korteweg-de Vries equation and water waves. Part 2. Comparison with experiments," *Journal of Fluid Mechanics*, vol. 65, no. 2, pp. 289–314, 1974. DOI: 10.1017/S002211207400139X.

[60] A. Bettini, T. A. Minelli, and D. Pascoli, "Solitons in undergraduate laboratory," *American Journal of Physics*, vol. 51, no. 11, pp. 977–984, 1983. DOI: 10.1119/1.13453.

[61] M. Olsen, H. Smith, and A. C. Scott, "Solitons in a wave tank," *American Journal of Physics*, vol. 52, no. 9, pp. 826–830, 1984. DOI: 10.1119/1.13542.

[62] A. M. Weiner, J. P. Heritage, R. J. Hawkins, R. N. Thurston, E. M. Kirschner, D. E. Leaird, and W. J. Tomlinson, "Experimental Observation of the Fundamental Dark Soliton in Optical Fibers," *Physical Review Letters*, vol. 61, no. 21, pp. 2445–2448, Nov. 1988. DOI: 10.1103/PhysRevLett.61.2445.

[63] J. S. Aitchison, A. M. Weiner, Y. Silberberg, D. E. Leaird, M. K. Oliver, J. L. Jackel, and P. W. E. Smith, "Experimental observation of spatial soliton interactions," *Optics Letters*, vol. 16, no. 1, p. 15, 1991. DOI: 10.1364/ol.16.000015.

[64] S. Minardi, F. Eilenberger, Y. V. Kartashov, A. Szameit, U. Röpke, J. Kobelke, K. Schuster, H. Bartelt, S. Nolte, L. Torner, F. Lederer, A. Tünnermann, and T. Pertsch, "Three-Dimensional Light Bullets in Arrays of Waveguides," *Physical Review Letters*, vol. 105, no. 26, p. 263 901, Dec. 2010. DOI: 10.1103/PhysRevLett.105.263901.

[65] V. F. Nesterenko, *Dynamics of Heterogeneous Materials*. New York, NY: Springer New York, 2001, pp. 65–81. DOI: 10.1007/978-1-4757-3524-6.

[66] C. Daraio, V. F. Nesterenko, E. B. Herbold, and S. Jin, "Tunability of solitary wave properties in one-dimensional strongly nonlinear phononic crystals," *Physical Review E - Statistical, Nonlinear, and Soft Matter Physics*, vol. 73, no. 2, pp. 1–10, 2006. DOI: 10.1103/PhysRevE.73.026610.

[67] A. F. Arrieta, I. K. Kuder, T. Waeber, and P. Ermanni, "Variable stiffness characteristics of embeddable multi-stable composites," *Composites Science and Technology*, vol. 97, pp. 12–18, 2014. DOI: 10.1016/j.compscitech.2014.03.017.

[68] S. A. Emam and D. J. Inman, "A Review on Bistable Composite Laminates for Morphing and Energy Harvesting," *Applied Mechanics Reviews*, vol. 67, no. 6, p. 060 803, 2015. DOI: 10.1115/1.4032037.

[69] N. Nadkarni, A. F. Arrieta, C. Chong, D. M. Kochmann, and C. Daraio, "Unidirectional Transition Waves in Bistable Lattices," *Physical Review Letters*, vol. 116, no. 24, p. 244 501, Jun. 2016. DOI: 10.1103/PhysRevLett.116.244501.

[70] J. R. Raney, N. Nadkarni, C. Daraio, D. M. Kochmann, J. A. Lewis, and K. Bertoldi, "Stable propagation of mechanical signals in soft media using stored elastic energy," *Proceedings of the National Academy of Sciences*, vol. 113, no. 35, pp. 9722–9727, 2016. DOI: 10.1073/pnas.1604838113.

[71] B. Deng, P. Wang, Q. He, V. Tournat, and K. Bertoldi, "Metamaterials with amplitude gaps for elastic solitons," *Nature Communications*, vol. 9, no. 1, p. 3410, Dec. 2018. DOI: 10.1038/s41467-018-05908-9.

[72] B. Deng, Y. Zhang, Q. He, V. Tournat, P. Wang, and K. Bertoldi, "Propagation of elastic solitons in chains of pre-deformed beams," *New Journal of Physics*, vol. 21, no. 7, 2019. DOI: 10.1088/1367-2630/ab2810.

[73] L. Jin, R. Khajehtourian, J. Mueller, A. Rafsanjani, V. Tournat, K. Bertoldi, and D. M. Kochmann, "Guided transition waves in multistable mechanical metamaterials," *Proceedings of the National Academy of Sciences*, vol. 117, no. 5, pp. 2319–2325, Feb. 2020. DOI: 10.1073/pnas.1913228117.

[74] M. F. Daqaq, R. Masana, A. Erturk, and D. Dane Quinn, "On the Role of Nonlinearities in Vibratory Energy Harvesting: A Critical Review and Discussion," *Applied Mechanics Reviews*, vol. 66, no. 4, p. 040 801, 2014. DOI: 10.1115/1.4026278.

[75] a. Erturk and D. J. Inman, "Broadband piezoelectric power generation on high-energy orbits of the bistable Duffing oscillator with electromechanical coupling," *Journal of Sound and Vibration*, vol. 330, no. 10, pp. 2339–2353, 2011. DOI: 10.1016/j.jsv.2010.11.018.

[76] K. Mikoshiba, J. M. Manimala, and C. Sun, "Energy harvesting using an array of multifunctional resonators," *Journal of Intelligent Material Systems and Structures*, vol. 24, no. 2, pp. 168–179, 2013. DOI: 10.1177/1045389X12460335.

[77] Z. Chen, Y. Yang, Z. Lu, and Y. Luo, "Broadband characteristics of vibration energy harvesting using one-dimensional phononic piezoelectric cantilever beams," *Physica B: Condensed Matter*, vol. 410, no. 1, pp. 5–12, 2013. DOI: 10.1016/j.physb.2012.10.029.

[78] S. Meninger, J. Mur-Miranda, R. Amirtharajah, A. Chandrakasan, and J. Lang, "Vibration-to-electric energy conversion," *IEEE Transactions on Very Large Scale Integration (VLSI) Systems*, vol. 9, no. 1, pp. 64–76, Feb. 2001. DOI: 10.1109/92.920820.

[79] S. Roundy, P. K. Wright, and J. Rabaey, "A study of low level vibrations as a power source for wireless sensor nodes," *Computer Communications*, vol. 26, no. 11, pp. 1131–1144, 2003. DOI: 10.1016/S0140-3664(02)00248-7.

[80] P. D. Mitcheson, E. M. Yeatman, G. K. Rao, A. S. Holmes, and T. C. Green, "Energy harvesting from human and machine motion for wireless electronic devices," *Proceedings of the IEEE*, vol. 96, no. 9, pp. 1457–1486, 2008. DOI: 10.1109/JPROC.2008.927494.

[81] C. Wei and X. Jing, "A comprehensive review on vibration energy harvesting: Modelling and realization," *Renewable and Sustainable Energy Reviews*, vol. 74, no. November 2016, pp. 1–18, 2017. DOI: 10.1016/j.rser.2017.01.073.

[82] P. Alevras, S. Theodossiades, and H. Rahnejat, "On the dynamics of a nonlinear energy harvester with multiple resonant zones," *Nonlinear Dynamics*, vol. 92, no. 3, pp. 1271–1286, May 2018. DOI: 10.1007/s11071-018-4124-2.

[83] J. Cao, S. Zhou, W. Wang, and J. Lin, "Influence of potential well depth on nonlinear tristable energy harvesting," *Applied Physics Letters*, vol. 106, no. 17, 2015. DOI: 10.1063/1.4919532.

[84] P. Kim and J. Seok, "A multi-stable energy harvester: Dynamic modeling and bifurcation analysis," *Journal of Sound and Vibration*, vol. 333, no. 21, pp. 5525–5547, 2014. DOI: 10.1016/j.jsv.2014.05.054.

[85] G. Scarselli, F. Nicassio, F. Pinto, F. Ciampa, O. Iervolino, and M. Meo, "A novel bistable energy harvesting concept," *Smart Materials and Structures*, vol. 25, no. 5, 2016. DOI: 10.1088/0964-1726/25/5/055001.

[86] S. Zhou, J. Cao, A. Erturk, J. Lin, S. Zhou, J. Cao, A. Erturk, and J. Lin, "Enhanced broadband piezoelectric energy harvesting using rotatable magnets Enhanced broadband piezoelectric energy harvesting using rotatable magnets," *Applied physics letters*, vol. 173901, no. May, pp. 1–5, 2013. DOI: 10.1063/1.4803445.

[87] S. Zhou, J. Cao, W. Wang, S. Liu, and J. Lin, "Modeling and experimental verification of doubly nonlinear magnet-coupled piezoelectric energy harvesting from ambient vibration," *Smart Materials and Structures*, vol. 24, no. 5, p. 55 008, 2015. DOI: 10.1088/0964-1726/24/5/055008.

[88] F. Cottone, H. Vocca, and L. Gammaitoni, "Nonlinear energy harvesting," *Physical Review Letters*, vol. 102, no. 8, pp. 1–4, 2009. DOI: 10.1103/PhysRevLett.102.080601.

[89] S. Gonella, A. C. To, and W. K. Liu, "Interplay between phononic bandgaps and piezoelectric microstructures for energy harvesting," *Journal of the Mechanics and Physics of Solids*, vol. 57, no. 3, pp. 621–633, 2009. DOI: 10.1016/j.jmps.2008.11.002.

[90] H. Lv, X. Tian, M. Y. Wang, and D. Li, "Vibration energy harvesting using a phononic crystal with point defect states," *Applied Physics Letters*, vol. 102, no. 3, pp. 14–17, 2013. DOI: 10.1063/1.4788810.

[91] L.-Y. Wu, L.-W. Chen, and C.-M. Liu, "Acoustic energy harvesting using resonant cavity of a sonic crystal," *Applied Physics Letters*, vol. 95, no. 1, p. 013 506, 2009. DOI: 10.1063/1.3176019.

[92] M. Carrara, M. R. Cacan, M. J. Leamy, M. Ruzzene, and A. Erturk, "Dramatic enhancement of structure-borne wave energy harvesting using an elliptical acoustic mirror," *Applied Physics Letters*, vol. 100, no. 20, 2012. DOI: 10.1063/1.4719098.

[93] M. Carrara, M. R. Cacan, J. Toussaint, M. J. Leamy, M. Ruzzene, and A. Erturk, "Metamaterial-inspired structures and concepts for elastoacoustic wave energy harvesting," *Smart Materials and Structures*, vol. 22, no. 6, p. 065 004, 2013. DOI: 10.1088/0964-1726/22/6/065004.

[94] R. U. Ahmed and S. Banerjee, "Low frequency energy scavenging using sub-wave length scale acousto-elastic metamaterial," *AIP Advances*, vol. 4, no. 11, 2014. DOI: 10.1063/1.4901915.

[95] G. Ma, M. Yang, S. Xiao, Z. Yang, and P. Sheng, "Acoustic metasurface with hybrid resonances," *Nature Materials*, vol. 13, no. 9, pp. 873–878, 2014. DOI: 10.1038/nmat3994.

[96] S. Qi, M. Oudich, Y. Li, and B. Assouar, "Acoustic energy harvesting based on a planar acoustic metamaterial," *Applied Physics Letters*, vol. 108, no. 26, p. 263 501, Jun. 2016. DOI: 10.1063/1.4954987.

[97] M. Hwang and A. F. Arrieta, "Input-Independent Energy Harvesting in Bistable Lattices from Transition Waves," *Scientific Reports*, vol. 8, no. 1, p. 3630, Dec. 2018. DOI: 10.1038/s41598-018-22003-7.

[98] E. W. Montroll and R. B. Potts, "Effect of defects on lattice vibrations: Interaction of defects and an analogy with meson pair theory," *Physical Review*, vol. 102, no. 1, pp. 72–84, 1956. DOI: 10.1103/PhysRev.102.72.

[99] S. Takeno, S. Kashiwamura, and E. Teramoto, "Frequencies of Localized Lattice Vibrations in One- and Three-Dimensional Lattices," *Progress of Theoretical Physics Supplement*, vol. 23, no. 23, pp. 124–140, 1962. DOI: 10.1143/PTPS.23.124.

[100] J. Hong and A. Xu, "Nondestructive identification of impurities in granular medium," *Applied Physics Letters*, vol. 81, no. 25, pp. 4868–4870, 2003. DOI: 10.1063/1.1522829.

[101] Y. Man, N. Boechler, G. Theocharis, P. G. Kevrekidis, and C. Daraio, "Defect modes in one-dimensional granular crystals," *Physical Review E - Statistical, Nonlinear, and Soft Matter Physics*, vol. 85, no. 3, pp. 3–7, 2012. DOI: 10.1103/PhysRevE.85.037601.

[102] S. Job, F. Santibanez, F. Tapia, and F. Melo, "Wave localization in strongly nonlinear Hertzian chains with mass defect," *Physical Review E - Statistical, Nonlinear, and Soft Matter Physics*, vol. 80, no. 2, pp. 3–6, 2009. DOI: 10.1103/PhysRevE.80.025602.

[103] G. Theocharis, M. Kavousanakis, P. G. Kevrekidis, C. Daraio, M. A. Porter, and I. G. Kevrekidis, "Localized breathing modes in granular crystals with defects," *Physical Review E - Statistical, Nonlinear, and Soft Matter Physics*, vol. 80, no. 6, pp. 1–11, 2009. DOI: 10.1103/PhysRevE.80.066601.

[104] Y. Ishimori and T. Munakata, "Kink Dynamics in the Discrete Sine-Gordon System A Perturbational Approach," *Journal of the Physical Society of Japan*, 1982. DOI: 10.1143/JPSJ.51.3367.

[105] M. Peyrard and M. D. Kruskal, "Kink dynamics in the highly discrete sine-Gordon system," *Physica D: Nonlinear Phenomena*, vol. 14, no. 1, pp. 88–102, Dec. 1984. DOI: 10.1016/0167-2789(84)90006-X.

[106] A. Kwaśniewski, P. Machnikowski, and P. Magnuszewski, "Kink dynamics in finite discrete sine-Gordon chains," *Physical Review E*, vol. 59, no. 2, pp. 2347–2354, Feb. 1999. DOI: 10.1103/PhysRevE.59.2347.

[107] C. Kunz and J. A. Combs, "Discrete theory of kink diffusion in the $\phi 4$ lattice with comparison to the continuum approximation," *Physical Review B*, vol. 31, no. 1, pp. 527–535, Jan. 1985. DOI: 10.1103/PhysRevB.31.527.

[108] A. P. Browning, F. G. Woodhouse, and M. J. Simpson, "Reversible signal transmission in an active mechanical metamaterial," *Proceedings of the Royal Society A: Mathematical, Physical and Engineering Sciences*, 2019. DOI: 10.1098/rspa.2019.0146.

[109] M. B. Fogel, S. E. Trullinger, A. R. Bishop, and J. A. Krumhansl, "Dynamics of sine-Gordon solitons in the presence of perturbations," *Physical Review B*, vol. 15, no. 3, pp. 1578–1592, Feb. 1977. DOI: 10.1103/PhysRevB.15.1578.

[110] P. J. Pascual and L. Vázquez, "Sine-Gordon solitons under weak stochastic perturbations," *Physical Review B*, vol. 32, no. 12, pp. 8305–8311, Dec. 1985. DOI: 10.1103/PhysRevB.32.8305.

[111] P. Biller and F. Petruccione, "Dynamics of sine-Gordon solitons under random perturbations: Weak additive large-scale white noise," *Physical Review B*, vol. 41, no. 4, pp. 2139–2144, Feb. 1990. DOI: 10.1103/PhysRevB.41.2139.

[112] S. A. Gredeskul and Y. S. Kivshar, "Propagation and scattering of nonlinear waves in disordered systems," *Physics Reports*, vol. 216, no. 1, pp. 1–61, 1992. DOI: 10.1016/0370-1573(92)90023-S.

[113] Zhang Fei, Y. S. Kivshar, and L. Vázquez, "Resonant kink-impurity interactions in the sine-Gordon model," *Physical Review A*, vol. 45, no. 8, pp. 6019–6030, Apr. 1992. DOI: 10.1103/PhysRevA.45.6019.

[114] M. J. Rodrguez-Plaza and L. Vázquez, "Additive and multiplicative perturbations on $\phi 4$ kinks," *Physical Review B*, vol. 41, no. 16, pp. 11 437–11 448, Jun. 1990. DOI: 10.1103/PhysRevB.41.11437.

[115] V. V. Konotop, A. Sánchez, and L. Vázquez, "Kink dynamics in the weakly stochastic $\phi 4$ model," *Physical Review B*, vol. 44, no. 6, pp. 2554–2566, Aug. 1991. DOI: 10.1103/PhysRevB.44.2554.

[116] A. Sánchez, L. Vázquez, and V. V. Konotop, "Dynamics of a $\phi 4$ kink in the presence of strong potential fluctuations, dissipation, and boundaries," *Physical Review A*, vol. 44, no. 2, pp. 1086–1103, Jul. 1991. DOI: 10.1103/PhysRevA.44.1086.

[117] Zhang Fei, V. V. Konotop, M. Peyrard, and L. Vázquez, "Kink dynamics in the periodically modulated $\phi 4$ model," *Physical Review E*, vol. 48, no. 1, pp. 548–554, Jul. 1993. DOI: 10.1103/PhysRevE.48.548.

[118] P. Malatkar and A. H. Nayfeh, "On the transfer of energy between widely spaced modes in structures," *Nonlinear Dynamics*, 2003. DOI: 10.1023/A:1022072808880.

[119] M. Serra-Garcia, M. Molerón, and C. Daraio, "Tunable, synchronized frequency down-conversion in magnetic lattices with defects," *Philosophical Transactions of the Royal Society A: Mathematical, Physical and Engineering Sciences*, vol. 376, no. 2127, p. 20 170 137, Aug. 2018. DOI: 10.1098/rsta.2017.0137.

[120] J. M. Mauricio, A. Marano, A. Gómez-Expósito, and J. L. M. Ramos, "Frequency regulation contribution through variable-speed wind energy conversion systems," *IEEE Transactions on Power Systems*, 2009. DOI: 10.1109/TPWRS.2008.2009398.

[121] H. Kulah and K. Najafi, "Energy Scavenging from Low-Frequency Vibrations by Using Frequency Up-Conversion for Wireless Sensor Applications," *IEEE Sensors Journal*, vol. 8, no. 3, pp. 261–268, 2008. DOI: 10.1109/JSEN.2008.917125.

[122] S.-M. Jung and K.-S. Yun, "Energy-harvesting device with mechanical frequency-up conversion mechanism for increased power efficiency and wideband operation," *Applied Physics Letters*, vol. 96, no. 11, p. 111 906, Mar. 2010. DOI: 10.1063/1.3360219.

[123] P. A. Franken, A. E. Hill, C. W. Peters, and G. Weinreich, "Generation of Optical Harmonics," *Physical Review Letters*, vol. 7, no. 4, pp. 118–119, Aug. 1961. DOI: 10.1103/PhysRevLett.7.118.

[124] R. H. Stolen, J. E. Bjorkholm, and A. Ashkin, "Phase-matched three-wave mixing in silica fiber optical waveguides," *Applied Physics Letters*, vol. 24, no. 7, pp. 308–310, Apr. 1974. DOI: 10.1063/1.1655195.

[125] Y. C. Chen, H. G. Winful, and J. M. Liu, "Subharmonic bifurcations and irregular pulsing behavior of modulated semiconductor lasers," *Applied Physics Letters*, vol. 47, no. 3, pp. 208–210, 1985. DOI: 10.1063/1.96219.

[126] Y. R. Chen, "Surface properties probed by second-harmonic and sum-frequency generation," *Nature*, vol. 337, no. 9, p. 519, 1989.

[127] J. G. Rarity, P. R. Tapster, E. Jakeman, T. Larchuk, R. A. Campos, M. C. Teich, and B. E. Saleh, "Two-photon interference in a Mach-Zehnder interferometer," *Physical Review Letters*, 1990. DOI: 10.1103/PhysRevLett.65.1348.

[128] M. M. Fejer, "Nonlinear Optical Frequency Conversion," *Physics Today*, vol. 47, no. 5, pp. 25–32, May 1994. DOI: 10.1063/1.881430.

[129] A. H. Nayfeh and D. T. Mook, *Nonlinear Oscillations*. Wiley, May 1995. DOI: 10.1002/9783527617586.

[130] L. N. Virgin, *Introduction to Experimental Nonlinear Dynamics*. Cambridge University Press, Mar. 2000. DOI: 10.1017/9781139175227.

[131] T. J. Anderson, A. H. Nayfeh, and B. Balachandran, "Coupling between high-frequency modes and a low-frequency mode: Theory and experiment," *Nonlinear Dynamics*, vol. 11, no. 1, pp. 17–36, 1996. DOI: 10.1007/BF00045049.

[132] R. Ganesh and S. Gonella, "Nonlinear waves in lattice materials: Adaptively augmented directivity and functionality enhancement by modal mixing," *Journal of the Mechanics and Physics of Solids*, vol. 99, no. November 2016, pp. 272–288, Feb. 2017. DOI: 10.1016/j.jmps.2016.11.001.

[133] R. Ganesh and S. Gonella, "Experimental evidence of directivity-enhancing mechanisms in nonlinear lattices," *Applied Physics Letters*, vol. 110, no. 8, pp. 1–6, 2017. DOI: 10.1063/1.4976805.

[134] X. Fang, J. Wen, D. Yu, G. Huang, and J. Yin, "Wave propagation in a nonlinear acoustic metamaterial beam considering third harmonic generation," *New Journal of Physics*, vol. 20, no. 12, p. 123 028, Dec. 2018. DOI: 10.1088/1367-2630/aaf65e.

[135] M. Pozzi, "Impulse excitation of piezoelectric bimorphs for energy harvesting: a dimensionless model," *Smart Materials and Structures*, vol. 23, no. 4, p. 045 044, Apr. 2014. DOI: 10.1088/0964-1726/23/4/045044.

[136] F. Bloch, "Über die Quantenmechanik der Elektronen in Kristallgittern," *Zeitschrift für Physik*, 1929. DOI: 10.1007/BF01339455.

[137] W. T. Thomson, "Transmission of elastic waves through a stratified solid medium," *Journal of Applied Physics*, vol. 21, no. 2, pp. 89–93, 1950. DOI: 10.1063/1.1699629.

[138] A. Erturk, J. Hoffmann, and D. J. Inman, "A piezomagnetoelastic structure for broadband vibration energy harvesting," *Applied Physics Letters*, vol. 94, no. 25, pp. 92–95, 2009. DOI: 10.1063/1.3159815.

[139] A. Hajati and S. G. Kim, "Ultra-wide bandwidth piezoelectric energy harvesting," *Applied Physics Letters*, vol. 99, no. 8, pp. 10–13, 2011. DOI: 10.1063/1.3629551.

[140] S. P. Pellegrini, N. Tolou, M. Schenk, and J. L. Herder, "Bistable vibration energy harvesters: A review," *Journal of Intelligent Material Systems and Structures*, vol. 24, no. 11, pp. 1303–1312, 2013. DOI: 10.1177/1045389X12444940.

[141] A. F. Arrieta, T. Delpero, A. E. Bergamini, and P. Ermanni, "Broadband vibration energy harvesting based on cantilevered piezoelectric bi-stable composites," *Applied Physics Letters*, vol. 102, no. 17, p. 173 904, 2013. DOI: 10.1063/1.4803918.

[142] R. L. Harne and K. W. Wang, "A review of the recent research on vibration energy harvesting via bistable systems," *Smart Materials and Structures*, vol. 22, no. 2, p. 023 001, 2013. DOI: 10.1088/0964-1726/22/2/023001.

[143] S. Zhou, J. Cao, W. Wang, S. Liu, and J. Lin, "Modeling and experimental verification of doubly nonlinear magnet-coupled piezoelectric energy harvesting from ambient vibration," *Smart Materials and Structures*, vol. 24, no. 5, p. 55 008, 2015. DOI: 10.1088/0964-1726/24/5/055008.

[144] L. Fok, M. Ambati, and X. Zhang, "Acoustic Metamaterials," *MRS Bulletin*, vol. 33, no. 10, pp. 931–934, 2008.

[145] J. Li, X. Zhou, G. Huang, and G. Hu, "Acoustic metamaterials capable of both sound insulation and energy harvesting," *Smart Materials and Structures*, vol. 25, no. 4, p. 045 013, 2016. DOI: 10.1088/0964-1726/25/4/045013.

[146] N. E. DuToit, B. L. Wardle, and S.-G. Kim, "Design considerations for mems-scale piezoelectric mechanical vibration energy harvesters," *Integrated Ferroelectrics*, vol. 71, no. 1, pp. 121–160, 2005. DOI: 10.1080/10584580590964574.

[147] Z. Chen, B. Guo, Y. Yang, and C. Cheng, "Metamaterials-based enhanced energy harvesting: A review," *Physica B: Condensed Matter*, vol. 438, pp. 1–8, 2014. DOI: 10.1016/j.physb.2013.12.040.

[148] K. Li and P. Rizzo, "Energy harvesting using arrays of granular chains and solid rods," *Journal of Applied Physics*, vol. 117, no. 21, p. 215 101, 2015. DOI: 10.1063/1.4921856.

[149] C. Chong, E. Kim, E. G. Charalampidis, H. Kim, F. Li, P. G. Kevrekidis, J. Lydon, C. Daraio, and J. Yang, "Nonlinear vibrational-state excitation and piezoelectric energy conversion in harmonically driven granular chains," *Physical Review E - Statistical, Nonlinear, and Soft Matter Physics*, vol. 93, no. 5, pp. 1–10, 2016. DOI: 10.1103/PhysRevE.93.052203.

[150] T. Chen, J. Mueller, and K. Shea, "Integrated design and simulation of tunable, multi-state structures fabricated monolithically with multi-material 3d printing," *Scientific Reports*, vol. 7, p. 45 671, 2017. DOI: 10.1038/srep45671.

[151] B. Haghpanah, L. Salari-Sharif, P. Pourrajab, J. Hopkins, and L. Valdevit, "Architected materials: Multistable shape-reconfigurable architected materials," *Advanced Materials*, vol. 28, no. 36, p. 8065, 2016. DOI: 10.1002/adma.201670255.

[152] R. L. Harne, Z. Wu, and K. W. Wang, "Designing and harnessing the metastable states of a modular metastructure for programmable mechanical properties adaptation," *Journal of Mechanical Design*, vol. 138, no. 2, p. 021 402, 2015. DOI: 10.1115/1.4032093.

[153] S. Shan, S. H. Kang, J. R. Raney, P. Wang, L. Fang, F. Candido, J. A. Lewis, and K. Bertoldi, "Multistable architected materials for trapping elastic strain energy," *Advanced Materials*, vol. 27, no. 29, pp. 4296–4301, 2015. DOI: 10.1002/adma.201501708.

[154] C. Williams and R. Yates, "Analysis of a micro-electric generator for microsystems," *Sensors and Actuators A: Physical*, vol. 52, no. 1-3, pp. 8–11, 1996. DOI: 10.1016/0924-4247(96)80118-X.

[155] J. Doyle, *Wave Propagation in Structures: Spectral Analysis Using Fast Discrete Fourier Transforms*. Springer New York, 1997.

[156] O. M. Braun and Y. S. Kivshar, "Nonlinear dynamics of the Frenkel-Kontorova model with impurities," *Physical Review B*, vol. 43, no. 1, pp. 1060–1073, Jan. 1991. DOI: 10.1103/PhysRevB.43.1060.

[157] M. Ruzzene, F. Scarpa, and F. Soranna, "Wave beaming effects in two-dimensional cellular structures," *Smart Materials and Structures*, vol. 12, no. 3, pp. 363–372, 2003. DOI: 10.1088/0964-1726/12/3/307.

[158] A. Khelif, A. Choujaa, S. Benchabane, B. Djafari-Rouhani, and V. Laude, "Guiding and bending of acoustic waves in highly confined phononic crystal waveguides," *Applied Physics Letters*, vol. 84, no. 22, pp. 4400–4402, May 2004. DOI: 10.1063/1.1757642.

[159] M. Oudich, M. B. Assouar, and Z. Hou, "Propagation of acoustic waves and waveguiding in a two-dimensional locally resonant phononic crystal plate," *Applied Physics Letters*, vol. 97, no. 19, 2010. DOI: 10.1063/1.3513218.

[160] L. Y. Wu, T. Y. Chiang, C. N. Tsai, M. L. Wu, and L. W. Chen, "Design of an acoustic bending waveguide with acoustic metamaterials via transformation acoustics," *Applied Physics A: Materials Science and Processing*, vol. 109, no. 3, pp. 523–533, 2012. DOI: 10.1007/s00339-012-7296-5.

[161] A. Hkansson, F. Cervera, and J. Sánchez-Dehesa, "Sound focusing by flat acoustic lenses without negative refraction," *Applied Physics Letters*, vol. 86, no. 5, pp. 1–3, 2005. DOI: 10.1063/1.1852719.

[162] S. Guenneau, A. Movchan, G. P??tursson, and S. A. Ramakrishna, "Acoustic metamaterials for sound focusing and confinement," *New Journal of Physics*, vol. 9, 2007. DOI: 10.1088/1367-2630/9/11/399.

[163] A. Spadoni and C. Daraio, "Generation and control of sound bullets with a nonlinear acoustic lens.," *Proceedings of the National Academy of Sciences of the United States of America*, vol. 107, no. 16, pp. 7230–4, 2010. DOI: 10.1073/pnas.1001514107.

[164] D. Bigoni, S. Guenneau, A. B. Movchan, and M. Brun, "Elastic metamaterials with inertial locally resonant structures: Application to lensing and localization," *Physical Review B - Condensed Matter and Materials Physics*, vol. 87, no. 17, pp. 1–6, 2013. DOI: 10.1103/PhysRevB.87.174303.

[165] K. Li, P. Rizzo, and X. Ni, "Alternative Designs of Acoustic Lenses Based on Nonlinear Solitary Waves," *Journal of Applied Mechanics*, vol. 81, no. 7, p. 071 011, Apr. 2014. DOI: 10.1115/1.4027327.

[166] E. N. Chatzi, V. K. Dertimanis, I. A. Antoniadis, and P. R. Wagner, "On the feasibility of structural metamaterials for seismic-induced vibration mitigation," *International Journal of Earthquake and Impact Engineering*, vol. 1, no. 1/2, p. 20, 2016. DOI: 10.1504/IJEIE.2016.10000957.

[167] S. Brûlé, B. Ungureanu, Y. Achaoui, A. Diatta, R. Aznavourian, T. Antonakakis, R. Craster, S. Enoch, and S. Guenneau, "Metamaterial-like transformed urbanism," *Innovative Infrastructure Solutions*, vol. 2, no. 1, p. 20, Dec. 2017. DOI: 10.1007/s41062-017-0063-x.

[168] A. F. Arrieta and M. Hwang, "Response invariance in a lattice of bistable elements with elastic interactions," in *Active and Passive Smart Structures and Integrated Systems XII*, A. Erturk, Ed., SPIE, Mar. 2018, p. 32. DOI: 10.1117/12.2303422.

[169] A. Chopra, *Dynamics of Structures: Theory and Applications to Earthquake Engineering*. Prentice Hall, 2012, pp. 683–686.

[170] M. Hwang and A. F. Arrieta, "Solitary waves in bistable lattices with stiffness grading: Augmenting propagation control," *Physical Review E*, 2018. DOI: 10.1103/PhysRevE.98.042205.

[171] J. Rubinstein, "Sine-Gordon Equation," *Journal of Mathematical Physics*, vol. 11, no. 1, pp. 258–266, Jan. 1970. DOI: 10.1063/1.1665057.

[172] F. M. Russell, Y. Zolotaryuk, J. C. Eilbeck, and T. Dauxois, "Moving breathers in a chain of magnetic pendulums," *Physical Review B*, vol. 55, no. 10, pp. 6304–6308, 1997. DOI: 10.1103/PhysRevB.55.6304.

[173] L. Slepyan, A. Cherkaev, and E. Cherkaev, "Transition waves in bistable structures. II. Analytical solution: Wave speed and energy dissipation," *Journal of the Mechanics and Physics of Solids*, vol. 53, no. 2, pp. 407–436, 2005. DOI: 10.1016/j.jmps.2004.08.001.

[174] S. Flach and A. V. Gorbach, "Discrete breathers - Advances in theory and applications," *Physics Reports*, vol. 467, no. 1-3, pp. 1–116, 2008. DOI: 10.1016/j.physrep.2008.05.002.

[175] S. Sen, J. Hong, J. Bang, E. Avalos, and R. Doney, "Solitary waves in the granular chain," *Physics Reports*, vol. 462, no. 2, pp. 21–66, 2008. DOI: 10.1016/j.physrep.2007.10.007.

[176] G. Theocharis, N. Boechler, and C. Daraio, "Nonlinear Periodic Phononic Structures and Granular Crystals," in, 2013, pp. 217–251. DOI: 10.1007/978-3-642-31232-8_7.

[177] S. A. Gredeskul, Y. S. Kivshar, L. K. Maslov, A. Sánchez, and L. Vázquez, "Kink propagation through disordered media," *Physical Review A*, vol. 45, no. 12, pp. 8867–8873, Jun. 1992. DOI: 10.1103/PhysRevA.45.8867.

[178] V. F. Nesterenko, C. Daraio, E. B. Herbold, and S. Jin, "Anomalous Wave Reflection at the Interface of Two Strongly Nonlinear Granular Media," *Physical Review Letters*, vol. 95, no. 15, p. 158 702, Oct. 2005. DOI: 10.1103/PhysRevLett.95.158702.

[179] C. Daraio, V. F. Nesterenko, E. B. Herbold, and S. Jin, "Energy trapping and shock disintegration in a composite granular medium," *Physical Review Letters*, vol. 96, no. 5, p. 058 002, 2006. DOI: 10.1103/PhysRevLett.96.058002.

[180] M. A. Porter, C. Daraio, I. Szelengowicz, E. B. Herbold, and P. Kevrekidis, "Highly nonlinear solitary waves in heterogeneous periodic granular media," *Physica D: Non-*

linear Phenomena, vol. 238, no. 6, pp. 666–676, Apr. 2009. DOI: 10.1016/j.physd.2008.12.010.

[181] F. Li, L. Zhao, Z. Tian, L. Yu, and J. Yang, "Visualization of solitary waves via laser Doppler vibrometry for heavy impurity identification in a granular chain," DOI: 10.1088/0964-1726/22/3/035016.

[182] R. Potekin, K. R. Jayaprakash, D. M. McFarland, K. Remick, L. A. Bergman, and A. F. Vakakis, "Experimental Study of Strongly Nonlinear Resonances and Anti-Resonances in Granular Dimer Chains," *Experimental Mechanics*, vol. 53, no. 5, pp. 861–870, Jun. 2013. DOI: 10.1007/s11340-012-9673-6.

[183] J. Yang, M. Gonzalez, E. Kim, C. Agbasi, and M. Sutton, "Attenuation of Solitary Waves and Localization of Breathers in 1D Granular Crystals Visualized via High Speed Photography," *Experimental Mechanics*, vol. 54, no. 6, pp. 1043–1057, 2014. DOI: 10.1007/s11340-014-9866-2.

[184] M. Molerón, A. Leonard, and C. Daraio, "Solitary waves in a chain of repelling magnets," *Journal of Applied Physics*, vol. 115, no. 18, p. 184 901, May 2014. DOI: 10.1063/1.4872252.

[185] D. N. Christodoulides and E. D. Eugenieva, "Blocking and Routing Discrete Solitons in Two-Dimensional Networks of Nonlinear Waveguide Arrays," *Physical Review Letters*, vol. 87, no. 23, p. 233 901, Nov. 2001. DOI: 10.1103/PhysRevLett.87.233901.

[186] D. N. Christodoulides, F. Lederer, and Y. Silberberg, "Discretizing light behaviour in linear and nonlinear waveguide lattices," *Nature*, vol. 424, no. 6950, pp. 817–823, Aug. 2003. DOI: 10.1038/nature01936.

[187] P. Marin-Palomo, J. N. Kemal, M. Karpov, A. Kordts, J. Pfeifle, M. H. P. Pfeiffer, P. Trocha, S. Wolf, V. Brasch, M. H. Anderson, R. Rosenberger, K. Vijayan, W. Freude, T. J. Kippenberg, and C. Koos, "Microresonator-based solitons for massively parallel coherent optical communications," *Nature*, vol. 546, no. 7657, pp. 274–279, Jun. 2017. DOI: 10.1038/nature22387.

[188] W. Wustmann and K. D. Osborn, "Reversible fluxon logic: Topological particles allow ballistic gates along one-dimensional paths," *Physical Review B*, vol. 101, no. 1, p. 14 516, 2020. DOI: 10.1103/PhysRevB.101.014516.

[189] M. C. Cassidy, A. Bruno, S. Rubbert, M. Irfan, J. Kammhuber, R. N. Schouten, A. R. Akhmerov, and L. P. Kouwenhoven, "Demonstration of an ac Josephson junction laser," *Science*, vol. 355, no. 6328, pp. 939–942, Mar. 2017. DOI: 10.1126/science.aah6640.

[190] A. Zareei, B. Deng, and K. Bertoldi, "Harnessing transition waves to realize deployable structures," *Proceedings of the National Academy of Sciences*, vol. 117, no. 8, pp. 4015–4020, Feb. 2020. DOI: 10.1073/pnas.1917887117.

[191] T. Singhal, E. Kim, T.-Y. Kim, and J. Yang, "Weak bond detection in composites using highly nonlinear solitary waves," *Smart Materials and Structures*, vol. 26, no. 5, p. 055 011, May 2017. DOI: 10.1088/1361-665X/aa6823.

[192] T. Chen, O. R. Bilal, K. Shea, and C. Daraio, "Harnessing bistability for directional propulsion of untethered, soft robots," *Proceedings of the National Academy of Sciences*, no. 00386, 2018. DOI: https://doi.org/10.1073/pnas.1800386115.

[193] A. M. Weiner, "Cavity solitons come of age," *Nature Photonics*, vol. 11, no. 9, pp. 533–535, Sep. 2017. DOI: 10.1038/nphoton.2017.149.

[194] L. Ozyuzer, A. E. Koshelev, C. Kurter, N. Gopalsami, Q. Li, M. Tachiki, K. Kadowaki, T. Yamamoto, H. Minami, H. Yamaguchi, T. Tachiki, K. E. Gray, W. K. Kwok, and U. Welp, "Emission of Coherent THz Radiation from Superconductors," *Science*, vol. 318, no. 5854, pp. 1291–1293, Nov. 2007. DOI: 10.1126/science.1149802.

[195] *See Supplemental Material at [URL will be inserted by publisher] for additional details about metabeam designs, numerical results, and experimental method. Movie S1 and S2 show the numerical and experimental demonstrations of solitonic resonance.*

[196] J. Leon, "Nonlinear supratransmission as a fundamental instability," *Physics Letters, Section A: General, Atomic and Solid State Physics*, vol. 319, no. 1-2, pp. 130–136, 2003. DOI: 10.1016/j.physleta.2003.10.012.

[197] M. J. Frazier and D. M. Kochmann, "Band gap transmission in periodic bistable mechanical systems," *Journal of Sound and Vibration*, vol. 388, pp. 315–326, 2017. DOI: 10.1016/j.jsv.2016.10.041.

[198] D. Restrepo, N. D. Mankame, and P. D. Zavattieri, "Phase transforming cellular materials," *Extreme Mechanics Letters*, vol. 4, pp. 52–60, 2015. DOI: 10.1016/j.eml.2015.08.001.

[199] Y. Song, R. M. Panas, S. Chizari, L. A. Shaw, J. A. Jackson, J. B. Hopkins, and A. J. Pascall, "Additively manufacturable micro-mechanical logic gates," *Nature Communications*, vol. 10, no. 1, pp. 1–6, 2019. DOI: 10.1038/s41467-019-08678-0.

[200] B. G.-g. Chen, N. Upadhyaya, and V. Vitelli, "Nonlinear conduction via solitons in a topological mechanical insulator," *Proceedings of the National Academy of Sciences*, vol. 111, no. 36, pp. 13 004–13 009, Sep. 2014. DOI: 10.1073/pnas.1405969111.

[201] I. Arretche and K. H. Matlack, "On the interrelationship between static and vibration mitigation properties of architected metastructures," *Frontiers in Materials*, vol. 5, no. November, pp. 1–16, 2018. DOI: 10.3389/fmats.2018.00068.

[202] B. Deng, C. Mo, V. Tournat, K. Bertoldi, and J. R. Raney, "Focusing and Mode Separation of Elastic Vector Solitons in a 2D Soft Mechanical Metamaterial," *Physical Review Letters*, vol. 123, no. 2, p. 024 101, Jul. 2019. DOI: 10.1103/PhysRevLett.123.024101.

[203] J. Meaud, "Nonlinear wave propagation and dynamic reconfiguration in two-dimensional lattices with bistable elements," *Journal of Sound and Vibration*, vol. 473, 2020. DOI: 10.1016/j.jsv.2020.115239.

[204] R. Chaunsali, E. Kim, and J. Yang, "Demonstration of accelerating and decelerating nonlinear impulse waves in functionally graded granular chains," *Philosophical Transactions of the Royal Society A: Mathematical, Physical and Engineering Sciences*, 2018. DOI: 10.1098/rsta.2017.0136.

[205] M. Hwang and F. A. Arrieta, "Extreme frequency conversion from soliton resonant interactions," *In review*, 2020.

[206] K. H. Matlack, A. Bauhofer, S. Krödel, A. Palermo, and C. Daraio, "Composite 3D-printed meta-structures for low frequency and broadband vibration absorption," pp. 1–10, 2015. DOI: 10.1073/pnas.1600171113.

[207] S. Krödel and C. Daraio, "Microlattice Metamaterials for Tailoring Ultrasonic Transmission with Elastoacoustic Hybridization," *Physical Review Applied*, vol. 6, no. 6, p. 064 005, Dec. 2016. DOI: 10.1103/PhysRevApplied.6.064005.

[208] P. Wang, F. Casadei, S. Shan, J. C. Weaver, and K. Bertoldi, "Harnessing Buckling to Design Tunable Locally Resonant Acoustic Metamaterials," *Physical Review Letters*, vol. 113, no. 1, p. 014 301, Jul. 2014. DOI: 10.1103/PhysRevLett.113.014301.

[209] J. Meaud and K. Che, "Tuning elastic wave propagation in multistable architected materials," *International Journal of Solids and Structures*, vol. 122-123, pp. 69–80, 2017. DOI: 10.1016/j.ijsolstr.2017.05.042.

[210] B. Luo, S. Gao, J. Liu, Y. Mao, Y. Li, and X. Liu, "Non-reciprocal wave propagation in one-dimensional nonlinear periodic structures," *AIP Advances*, vol. 8, no. 1, 2018. DOI: 10.1063/1.5010990.

[211] D. Bitar, N. Kacem, and N. Bouhaddi, "Investigation of modal interactions and their effects on the nonlinear dynamics of a periodic coupled pendulums chain," *International Journal of Mechanical Sciences*, vol. 127, no. December 2016, pp. 130–141, 2017. DOI: 10.1016/j.ijmecsci.2016.11.030.

[212] J. D. Lambert, *Numerical Methods for Ordinary Differential Systems: The Initial Value Problem*. USA: John Wiley & Sons, Inc., 1991.

[213] M. J. Quinn, *Parallel Programming in C with MPI and OpenMP*. McGraw-Hill Education Group, 2003.

[214] H. M. Hilber, T. J. R. Hughes, and R. L. Taylor, "Improved numerical dissipation for time integration algorithms in structural dynamics," *Earthquake Engineering & Structural Dynamics*, vol. 5, no. 3, pp. 283–292, Jul. 1977. DOI: 10.1002/eqe.4290050306.

[215] G. M. Amdahl, "Validity of the single processor approach to achieving large scale computing capabilities," in *Proceedings of the April 18-20, 1967, spring joint computer conference on - AFIPS '67 (Spring)*, New York, New York, USA: ACM Press, 1967, p. 483. DOI: 10.1145/1465482.1465560.

[216] J. L. Gustafson, "Reevaluating Amdahl's law," *Communications of the ACM*, vol. 31, no. 5, pp. 532–533, May 1988. DOI: 10.1145/42411.42415.

[217] M. Hwang and A. F. Arrieta, "Energy harvesting characteristics in metamaterials based on bistable lattices," in *Active and Passive Smart Structures and Integrated Systems XIII*, A. Erturk, Ed., SPIE, Mar. 2019, p. 13. DOI: 10.1117/12.2514426.

A. SUPPLEMENTARY INFORMATION FOR INPUT-INDEPENDENT ENERGY HARVESTING IN BISTABLE LATTICES FROM TRANSITION WAVES

Measured Force-Deflection Curves

Figure A.1 shows the experimentally-fitted force-displacement curves for the bistable element with 0.225 m of rail distance and for magnetic interaction from the previous study, and the corresponding parameters are summarised in Tab. A.1. Refer to the Supplemental Material of Ref. [33] in the manuscript for how these curves are obtained.

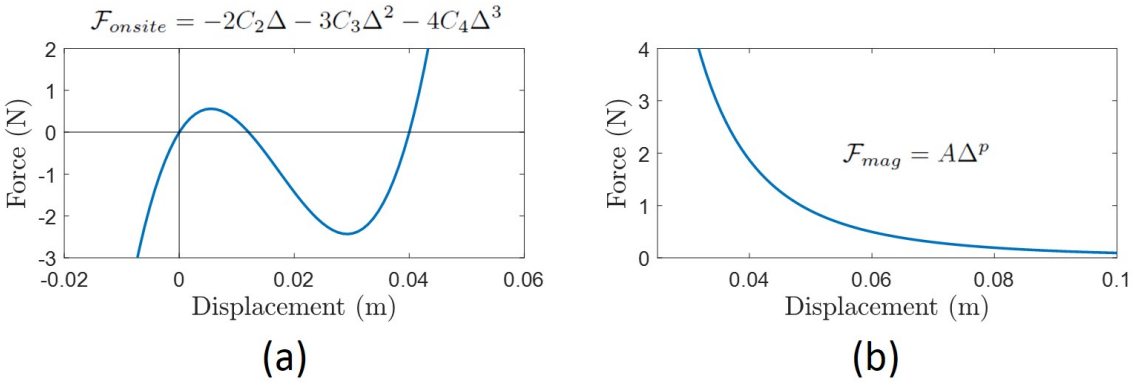

Figure A.1. (a) Experimental force-deflection curves for the bistable element with the rail distance $R = 0.225$ m and (b) inter-element magnetic force.

Table A.1. System parameters for the baseline lattice

A	p	C_2	C_3	C_4
4.95×10^{-5}	-3.274	217.101	-23,426	449,961

Phonon Transmission

Phonon transmission is obtained by linearising the governing equation about the stable equilibria, assuming a traveling wave solution of the form $\bar{u}_n = \bar{U}e^{i(\bar{k}n-\bar{\omega}\bar{t})}$, where $\bar{k}$ and $\bar{\omega}$ are

the nondimensionalised wave number and frequency. The dispersion relation in the linear regime is obtained as

$$\bar{k} = \pm 2 \arcsin \sqrt{\frac{-\bar{\omega}^2 - \mathrm{i}\bar{\omega}\bar{b} - \bar{\mathcal{F}}_{onsite}(\bar{u}_n^*)}{4p}}, \tag{A.1}$$

where $\bar{u}_n^*$ represents a static equilibrium position, and the following nondimensionalisation is used:

$$\bar{k} = kL, \quad \bar{\omega} = \omega T, \quad \bar{b} = \frac{bT}{m}, \quad \bar{\mathcal{F}}_{onsite} = \frac{\mathcal{F}_{onsite}}{AL^p}, \quad T^2 = \frac{m}{AL^{p-1}}. \tag{A.2}$$

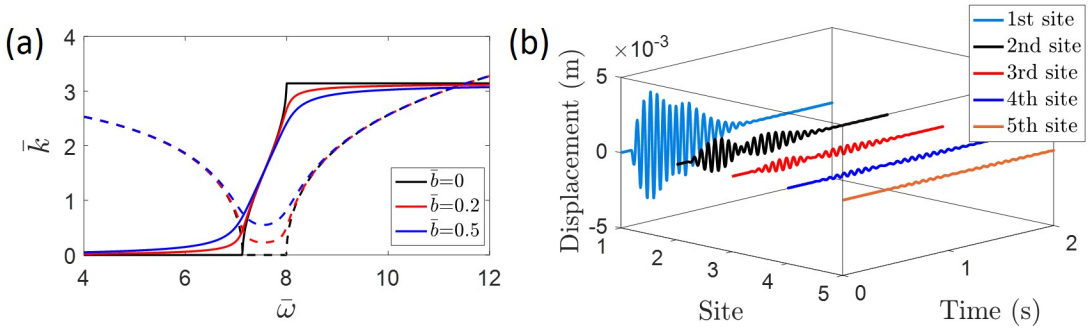

Figure A.2. (a) Dispersion relation of the linearised equation: real (solid line) and imaginary (dashed line) parts of the nondimensionalised wave number. (b) Analytical solution of the phonon transmission in a lightly damped (b=0.2 Ns/m) lattice under sinusoidal input with a frequency (ω=105 rad/s) within the pass band.

In Fig. A.2(a), this relation is plotted for different values of damping. For a conservative lattice ($\bar{b}$=0), the presence of the on-site potential acts as distributed elastic surroundings, resulting in a pass band between the low ($\bar{\omega}$=7.13) and high cutoff frequencies ($\bar{\omega}$=7.99). For dissipative systems ($\bar{b}$>0), $\bar{k}$ exhibits an imaginary part (dashed lines) which contributes to wave attenuation. Hence, phonons can never be stably transmitted in a physical setup. Figure A.2(b) shows the responses of the first five elements in this small-amplitude regime of the lattice system with a low damping (b=0.2 Ns/m). The phonon transmission is almost completely disintegrated after passing through only a few elements.

Minimum Snapping Force in a Lattice

The force-deflection curve for a lattice of multiple unit cells is obtained numerically by applying a load quasi-statically to the first element and measuring the corresponding deflection at the same site. The minimum snapping force is defined as the smallest static force that triggers the state change. The numerical simulation shows the same force-deflection relation for the lattices with more than three unit cells.

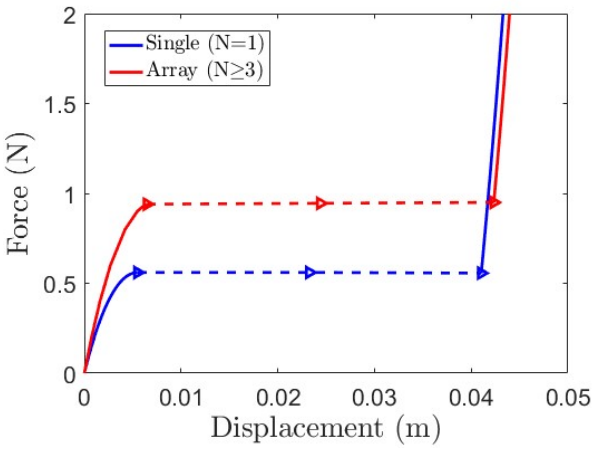

Figure A.3. Minimum snapping force required to induce the state transition for a single bistable element and an array of bistable elements.

Experimental Responses

The experimental (dashed lines) and numerical responses (solid lines) for two selected cases (periodic lattice and $L_{defect}/L = 0.857$) are plotted in Figs. A.4(a) and (b), respectively. To account for the manufacturing variability of the bistable elements, the experimental results are adjusted such that the snapping distances match those of numerical results. Although the details of the motion, such as the propagation velocity and the frequency of the free vibration after the completion of the state transition, do not match exactly, they still undergo qualitatively similar changes. Possible reasons for the discrepancy are the limited order of the quartic potential approximation to describe the on-site dynamics produced by the bistable elements and the presence of coupled rotational motion. Nevertheless, the

simplicity of the model used in this study captures the qualitative behaviour of the lattice, fulfilling the objectives of this investigation.

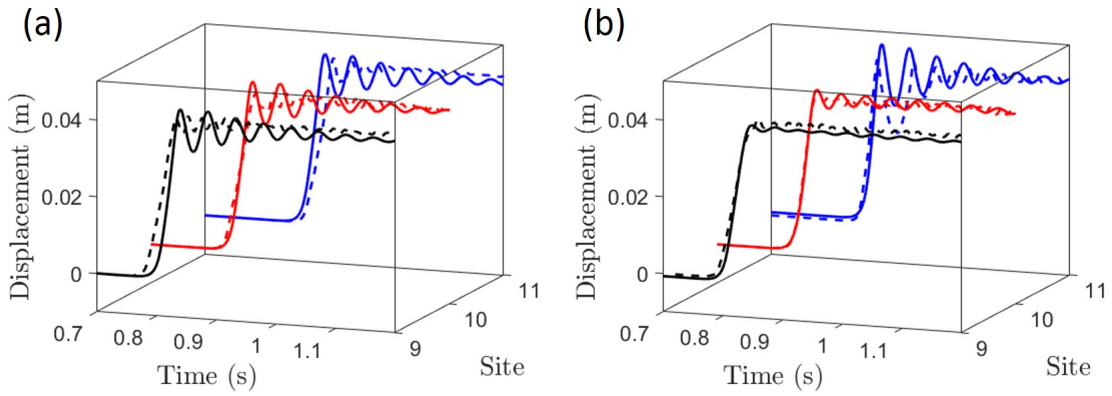

Figure A.4. Numerical (solid lines) and experimental (dashed lines) responses around the control site for (a) the periodic lattice and (b) the lattice spacing defect ratio of 0.857.

Energy Analysis

Consider an enclosed system of an infinitely long lattice of bistable elements. At the instant t_0 a wave enters the system, the total available energy in the system is $E_{tot}|_{t_0} = E_{\text{in}} + N\Delta\phi$, where E_{in}, $\Delta\phi$, and N are the wave energy transmitted from outside the system, difference between two stable states of the bistable element, and the number of elements in the system. From the infiniteness of the selected section, $E_{\text{in}} \ll N\Delta\phi$ and thus $E_{tot}|_{t_0} \approx N\Delta\phi$. After all the wave train passed by (so that all the elements in the system reach the steady states at the lower equilibria), the total energy at this instant can be written as $E_{tot}|_{t_\infty} = N\text{e}_{tot}|_{t_\infty}$ from periodicity of the lattice. e_{tot} is the total energy per unit element which can be expresses as $\text{e}_{tot} = k\text{e} + p\text{e}_{onsite} + p\text{e}_{mag} + d\text{e}$, where $k\text{e}$, $p\text{e}_{onsite}$, $p\text{e}_{mag}$, and $d\text{e}$ are kinetic energy, on-site potential, potential due to magnetic interaction, and dissipated energy per unit element, respectively. $E_{tot}|_{t_0}$ should remain constant for the same set of bistable elements, and therefore $E_{tot}|_{t_\infty}$ also remain unaltered even if any other lattice parameters than the on-site potential change. In addition, e_{tot} should be conserved at any time instant from the conservation of total energy in an enclosed system.

Effect of Mass Change

From the above argument, e_{tot}'s of two different lattices with the same on-site elements are conserved:

$$k\mathrm{e}^{(1)} + p\mathrm{e}^{(1)}_{onsite} + p\mathrm{e}^{(1)}_{mag} + d\mathrm{e}^{(1)} = k\mathrm{e}^{(2)} + p\mathrm{e}^{(2)}_{onsite} + p\mathrm{e}^{(2)}_{mag} + d\mathrm{e}^{(2)}, \tag{A.3}$$

where superscript indicates a lattice with a different set of parameters. During the displacement of mass from zero to an arbitrary deflection Δ, it is reasonable to assume $|p\mathrm{e}^{(2)}_{mag} - p\mathrm{e}^{(1)}_{mag}| \ll 1$ from the compactness of the transition wave (can span as small as a single element according to Ref. [33]). This leads to

$$\begin{aligned}(\frac{1}{2}mv^2)^{(1)} + \cancel{p\mathrm{e}_{onsite}|_{x=\Delta}} + (\int_{t(x=0)}^{t(x=\Delta)} bv^2dt)^{(1)} = (\frac{1}{2}mv^2)^{(2)} + \cancel{p\mathrm{e}_{onsite}|_{x=\Delta}} + (\int_{t(x=0)}^{t(x=\Delta)} bv^2dt)^{(2)} \\ \Rightarrow (\frac{1}{2}mv^2)^{(1)} + (\int_0^{\Delta} bvdx)^{(1)} = (\frac{1}{2}mv^2)^{(2)} + (\int_0^{\Delta} bvdx)^{(2)}.\end{aligned} \tag{A.4}$$

Letting $m^{(1)} > m^{(2)}$ and assuming a fixed b, it can be easily concluded that $v^{(1)} < v^{(2)}$ for all Δ. Now, dissecting the energy components when the element reaches its maximum potential (therefore $k\mathrm{e} = 0$),

$$p\mathrm{e}_{onsite}|_{x=\Delta_1} + \int_0^{\Delta_1} bv^{(1)}dx = p\mathrm{e}_{onsite}|_{x=\Delta_2} + \int_0^{\Delta_2} bv^{(2)}dx. \tag{A.5}$$

If $\Delta_1 < \Delta_2$, then $p\mathrm{e}_{onsite}|_{x=\Delta_1} < p\mathrm{e}_{onsite}|_{x=\Delta_2}$. The equality (A.5) can never hold since $v^{(1)}$ is always less than $v^{(2)}$ ($\int_0^{\Delta_1} bv^{(1)}dx < \int_0^{\Delta_2} bv^{(2)}dx$). On the other hand, the equality can satisfy for $\Delta_1 > \Delta_2$, which conclude that the a larger mass yields a larger amplitude.

Effect of Inter-element Forcing Change

As derived in the manuscript, $pe_{mag}^{(1,2)} = -\frac{A}{p+1}(x_2 - x_1 + L^{(1,2)})^{p+1}$. Since $p+1$ is in general negative, $pe_{mag}^{(1)} < pe_{mag}^{(2)}$ for $L^{(1)} > L^{(2)}$. Substituting this relation into Eq. (A.3), we obtain the following inequality:

$$(\frac{1}{2}mv^2)^{(1)} + \cancel{pe_{onsite}|_{x=\Delta}} + (\int_0^{\Delta} bvdx)^{(1)} < (\frac{1}{2}mv^2)^{(2)} + \cancel{pe_{onsite}|_{x=\Delta}} + (\int_0^{\Delta} bvdx)^{(2)}. \quad \text{(A.6)}$$

Similar to the case of mass change, it can be shown that $v^{(1)} < v^{(2)}$ for all Δ if $L^{(1)} > L^{(2)}$. At the instant that pe becomes maximum, the inequality becomes

$$pe_{onsite}|_{x=\Delta_1} + \int_0^{\Delta_1} bv^{(1)}dx < pe_{onsite}|_{x=\Delta_2} + \int_0^{\Delta_2} bv^{(2)}dx. \quad \text{(A.7)}$$

Following the same process, if $\Delta_1 > \Delta_2$, $pe_{onsite}|_{x=\Delta_1} > pe_{onsite}|_{x=\Delta_2}$. The inequality may be satisfied this time since $v^{(1)} < v^{(2)}$. If $\Delta_1 < \Delta_2$, then $pe_{onsite}|_{x=\Delta_1} < pe_{onsite}|_{x=\Delta_2}$ and $\int_0^{\Delta_1} bv^{(1)}dx < \int_0^{\Delta_2} bv^{(2)}dx$ so that the inequality always holds. Therefore, the effect of the inter-element forcing change (or lattice spacing change) is inconclusive; it may or may not induce a larger amplitude.

Time Progression of the Breather-like Mode

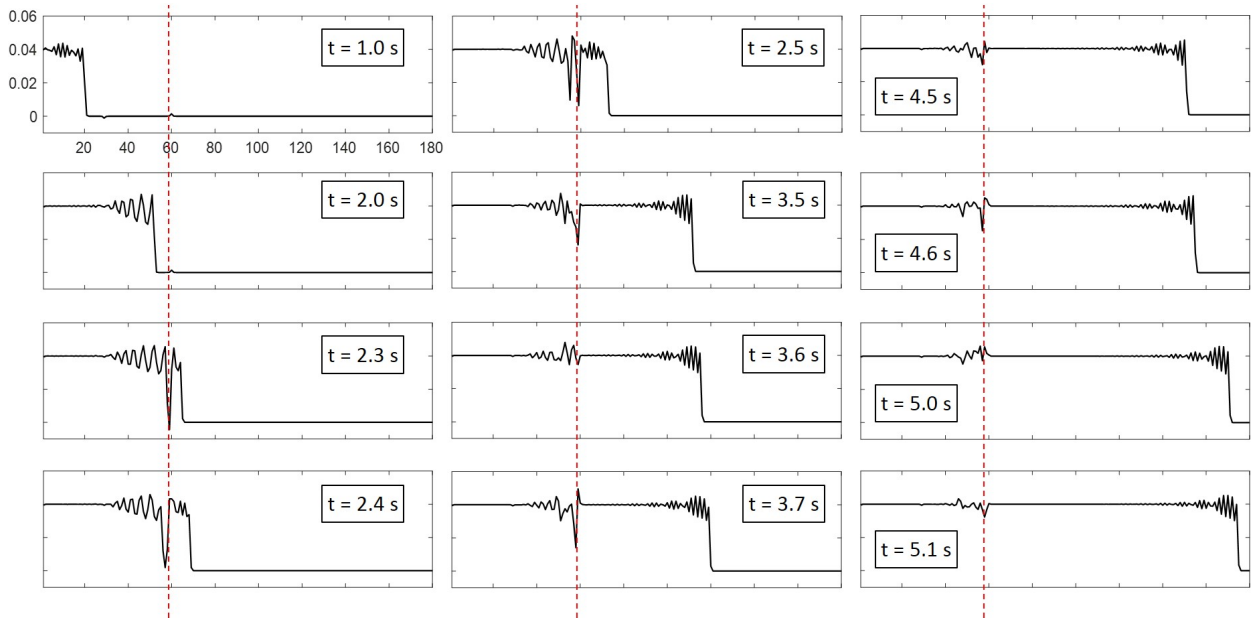

Figure A.5. Time progression of a breather-like mode in the spatial configuration. A spatially localised inter-well oscillation is generated while the main transition wave continues to propagate. The dashed red line indicates the boundary (59^{th} site) of the defect section.

Experimental Setup for Electromechanical Conversion Performance

Figure A.6(a) shows the bistable element with embedded piezoelectric transducers and its placement in the experimental setup. The specific location of the transducers are determined based on the FE analysis [Fig. A.6(b)], which shows that the largest in-plain strains of the fundamental mode in the length direction of the element occur near the roots.

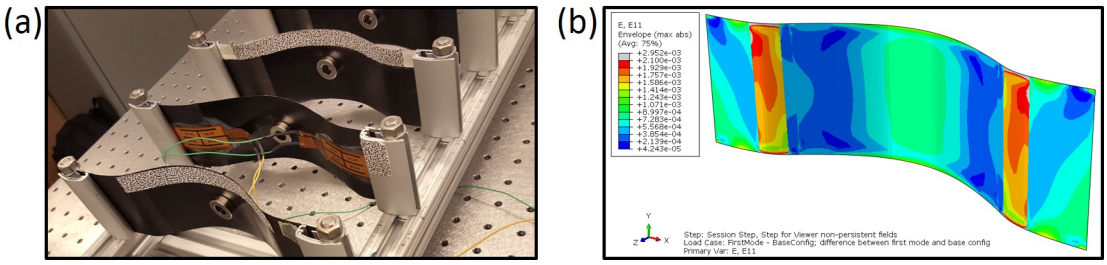

Figure A.6. (a) Piezoelectric transducer attachment to a bistable element and its installation within the lattice. (b) In-plane strain distribution of the fundamental mode in the length direction of the bistable element from FE analysis.

B. SUPPLEMENTARY INFORMATION FOR SOLITARY WAVES IN BISTABLE LATTICES WITH STIFFNESS GRADING: AUGMENTING PROPAGATION CONTROL

Projection of Eq. (11) on ψ_b

The projection of the linearized equation of motion [Eq. (11) in the manuscript] on ψ_b can be made by multiplying it by ψ_b and then integrating it over ξ. By taking advantage of orthogonality between the different modes, the term-by-term projections can be expressed as follows:

$$\int d\xi\, \psi_b^* f_{,\tau\tau} = \tfrac{\phi_{b,\tau\tau}}{c_b} \int d\xi\, \psi_b^* \psi_b + \tfrac{\phi_{1,\tau\tau}}{c_1} \underbrace{\cancel{\int d\xi\, \psi_b^* \psi_1}}_{\text{orthogonality}} + \int dk\, \phi_{k,\tau\tau} \underbrace{\cancel{\int d\xi\, \psi_b^* \psi_k}}_{\text{orthogonality}} = \phi_{b,\tau\tau}\,, \tag{B.1}$$

$$\int d\xi\, \psi_b^* \alpha(X) f_{,\tau\tau} = \tfrac{\phi_{b,\tau\tau}}{c_b} \int d\xi\, \alpha \psi_b^* \psi_b + \tfrac{\phi_{1,\tau\tau}}{c_1} \int d\xi\, \alpha \psi_b^* \psi_1 + \int dk\, \phi_{k,\tau\tau} \int d\xi\, \alpha \psi_b^* \psi_k, \tag{B.2}$$

$$\int d\xi\, \psi_b^* \alpha(X) f_{,\tau\xi} = -\tfrac{\phi_{b,\tau}}{2c_b} \int d\xi\, \gamma\alpha(X) \psi_b^* \psi_b + \tfrac{\phi_{1,\tau}}{c_1} \int d\xi\, \alpha \psi_b^* \psi_{1,\xi} + \int dk\, \phi_{k,\tau} \int d\xi\, \alpha \psi_b^* \psi_{k,\xi}\,, \tag{B.3}$$

$$\begin{aligned} \int d\xi\, \psi_b^* [-f_{,\xi\xi} + (2 - 3\,\mathrm{sech}^2\, \tfrac{\xi}{\sqrt{2}}) f] &= \int d\xi\, \psi_b^* \omega^2 f \\ &= \cancel{\tfrac{\omega_b^2 \phi_b}{c_b} \int d\xi\, \psi_b \psi_b} + \tfrac{\omega_1^2 \phi_1}{c_1} \cancel{\int d\xi\, \psi_b \psi_1} + \int dk\, \omega_k^2 \phi_k \cancel{\int d\xi\, \psi_b \psi_k} = 0, \end{aligned} \tag{B.4}$$

$$\begin{aligned} &\int d\xi\, \psi_b^* [-\alpha\gamma^2 f_{,\xi\xi} + \beta(2 - 3\,\mathrm{sech}^2\, \tfrac{\xi}{\sqrt{2}}) f] = \int d\xi\, \psi_b^* [\alpha\gamma^2 \omega^2 f + (\beta - \alpha\gamma^2)(2 - 3\,\mathrm{sech}^2\, \tfrac{\xi}{\sqrt{2}}) f] \\ &= \tfrac{\omega_1^2 \phi_1}{c_1} \int d\xi\, \alpha\gamma^2 \psi_b \psi_1 + \int dk\, \omega_k^2 \phi_k \int d\xi\, \alpha\gamma^2 \psi_b \psi_k + \tfrac{\phi_b}{c_b} \int d\xi\, (\beta - \alpha\gamma^2) \psi_b^* \psi_b \\ &+ \tfrac{\phi_1}{c_1} \int d\xi\, (\beta - \alpha\gamma^2) \psi_b^* \psi_1 + \int dk\, \phi_k \int d\xi\, (\beta - \alpha\gamma^2) \psi_b^* \psi_k - \tfrac{3\sqrt{2}\phi_b}{c_b} \int d\xi\, (\beta - \alpha\gamma^2) \psi_b^3 \\ &- \tfrac{3\sqrt{2}\phi_1}{c_1} \int d\xi\, (\beta - \alpha\gamma^2) \psi_b^2 \psi_1 - 3\sqrt{2} \int dk\, \phi_k \int d\xi\, (\beta - \alpha\gamma^2) \psi_b^2 \psi_k, \end{aligned} \tag{B.5}$$

where the relation $-\psi_{,\xi\xi} + (2 - 3\,\mathrm{sech}^2\left(\tfrac{\xi}{\sqrt{2}}\right))\psi = \omega^2 \psi$ and $\omega_b = 0$ are used in Eqs. (B.4) and (B.5).

$$\int d\xi\, \psi_b^* f_{,\tau} = \phi_{b,\tau}\,, \tag{B.6}$$

$$\int d\xi\, \psi_b^* \alpha(X) f_{,\tau} = \tfrac{\phi_{b,\tau}}{c_b} \int d\xi\, \alpha(X) \psi_b^* \psi_b + \tfrac{\phi_{1,\tau}}{c_1} \int d\xi\, \alpha(X) \psi_b^* \psi_1 + \int dk\, \phi_{k,\tau} \int d\xi\, \alpha(X) \psi_b^* \psi_k, \tag{B.7}$$

$$\int d\xi\, \psi_b^* f_{,\xi} = \tfrac{\phi_b}{c_b} \underbrace{\cancel{\int d\xi\, \psi_b^* \psi_{b,\xi}}}_{\text{direct integration}} + \tfrac{\phi_1}{c_1} \int d\xi\, \psi_b^* \psi_{1,\xi} + \int dk\, \phi_k \int d\xi\, \psi_b^* \psi_{k,\xi}\,, \tag{B.8}$$

$$\int d\xi\, \psi_b^* \alpha(X) f_{,\xi} = -\tfrac{\phi_b}{2c_b} \int d\xi\, \gamma\alpha(X)\psi_b^*\psi_b + \tfrac{\phi_1}{c_1} \int d\xi\, \alpha(X)\psi_b^*\psi_{1,\xi} + \int dk\, \phi_k \int d\xi\, \alpha(X)\psi_b^*\psi_{k,\xi}\,, \tag{B.9}$$

$$\int d\xi\, \psi_b^* \alpha(X) \operatorname{sech}^2 \tfrac{\xi}{\sqrt{2}} \tanh \tfrac{\xi}{\sqrt{2}} = -\int d\xi\, \alpha(X)\psi_b^*\psi_{b,\xi} = \tfrac{1}{2} \int d\xi\, \gamma\alpha(X)\psi_b^*\psi_b, \tag{B.10}$$

$$\int d\xi\, \psi_b^* \alpha(X) \tfrac{1}{\sqrt{2}} \operatorname{sech}^2(\tfrac{\xi}{\sqrt{2}}) = \int d\xi\, \alpha(X)\psi_b^*\psi_b, \tag{B.11}$$

$$\int d\xi\, \psi_b^* \tfrac{1}{\sqrt{2}} \operatorname{sech}^2(\tfrac{\xi}{\sqrt{2}}) = \int d\xi\, \psi_b^*\psi_b = c_b, \tag{B.12}$$

$$\int d\xi\, \psi_b^* \beta(X) \operatorname{sech}^2 \tfrac{\xi}{\sqrt{2}} \tanh \tfrac{\xi}{\sqrt{2}} = -\int d\xi\, \beta(X)\psi_b^*\psi_{b,\xi} = \tfrac{1}{2} \int d\xi\, \gamma\beta(X)\psi_b^*\psi_b, \tag{B.13}$$

Combining all terms together and assuming that the contributions from the coupling between different modes are minimal, the equation becomes

$$\begin{aligned} &\phi_{b,\tau\tau} - \gamma^2 v^2 \frac{\phi_{b,\tau\tau}}{c_b} \int d\xi\, \alpha\psi_b^*\psi_b - v\gamma^3 \frac{\phi_{b,\tau}}{c_b} \int d\xi\, \alpha(X)\psi_b^*\psi_b + \frac{\phi_b}{c_b} \int d\xi\, (\beta - \alpha\gamma^2)\psi_b^*\psi_b \\ &- \frac{3\sqrt{2}\phi_b}{c_b} \int d\xi\, (\beta - \alpha\gamma^2)\psi_b^3 + \gamma\delta\phi_{b,\tau} + \gamma v \frac{\phi_{b,\tau}}{c_b} \int d\xi\, \alpha(X)\psi_b^*\psi_b + \gamma^2 \frac{\phi_b}{2c_b} \int d\xi\, \alpha(X)\psi_b^*\psi_b \\ &+ \frac{1}{2}\gamma^3 \int d\xi\, \alpha(X)\psi_b^*\psi_b - \gamma \int d\xi\, \alpha(X)\psi_b^*\psi_b - \gamma\delta v c_b - \frac{1}{2}\gamma \int d\xi\, \beta(X)\psi_b^*\psi_b = 0. \end{aligned} \tag{B.14}$$

Eq. (B.14) can be solved numerically for any perturbation functions of $\alpha(X)$ and $\beta(X)$. However, consider linear variations $\alpha(X) = \tilde{\alpha}X$ and $\beta(X) = \tilde{\beta}X$ with small $\tilde{\alpha}$ and $\tilde{\beta}$ to seek for a closed-form solution. We further limit the analysis to the low-speed propagations $v \ll 1$, and then Eq. (B.14) becomes

$$\phi_{b,\tau\tau} + \gamma\delta\phi_{b,\tau} = -\tfrac{1}{2}\gamma^3\tilde{\alpha}c_b + \gamma\tilde{\alpha}c_b + \gamma\delta v c_b + \tfrac{1}{2}\gamma\tilde{\beta}c_b. \tag{B.15}$$

C. SUPPLEMENTARY INFORMATION FOR EXTREME FREQUENCY CONVERSION FROM SOLITON RESONANT INTERACTIONS

Solution for the Beam Subjected to a Moving Particle

The forced motion of a fixed-free beam under a moving impulse can be solved by the normal mode expansion. The normal modes can be obtained by solving the homogeneous problem

$$\phi(x) - \beta^4 \phi(x) = 0, \tag{C.1}$$

where $\beta^4 = \frac{\omega^2}{a^2}$, $a^2 = \frac{EI}{\rho A}$, and the prime represents the derivative with respect to x. One way to represent the normal modes of the fixed-free beam is

$$\phi_n(x) = (\cos\beta_n x - \cosh\beta_n x) + \zeta_n(\sin\beta_n x - \sinh\beta_n x), \tag{C.2}$$

where $\zeta_n = \frac{\sin\beta_n L - \sinh\beta_n L}{\cos\beta_n L + \cosh\beta_n L}$, and the eigenvalue β_n can be obtained from the roots of the characteristic equation $\cos\beta L \cosh\beta L = 1$. The unknown solution for the transverse displacement $v(x,t)$ can be expanded in terms of the normal modes as $v(x,t) = \sum_{n=1}^{\infty} q_n(t)\phi_n(x)$, where $q_n(t)$'s are the generalized Fourier coefficients corresponding to the normal modes $\phi_n(x)$'s. Substituting $v(x,t)$ into the governing equation [Eq. (1) in the manuscript] and using Eq. (C.1),

$$\sum_{n=1}^{\infty} [\ddot{q}_n(t) + a^2\beta_n^4 q_n(t)]\phi_n(x) = b\delta(x - ct), \tag{C.3}$$

where $b = \frac{eP}{\rho A}$. Using the orthogonality of $\phi_n(x)$'s, we obtain an ordinary differential equation for $q_n(t)$:

$$\ddot{q}_n(t) + a^2\beta_n^4 q_n(t) = \frac{\int b\delta(x - ct)\phi_n(x)dx}{W_n} = \frac{-b\phi_n(ct)}{W_n}. \tag{C.4}$$

where $W_n = \int \phi_n^2(x)dx$. Assuming zero initial conditions [$v(0) = 0$, $\dot{v}(0) = 0$], the solution for $a_n(t)$ can be obtained from the method of variation of parameters:

$$q_n(t) = \begin{cases} -\frac{b}{\omega_n W_n} \int_0^t \phi_n(c\tau) \sin \omega_n(t-\tau) d\tau & \text{for } 0 < t \leq \frac{L}{c} \\ -\frac{b}{\omega_n W_n} \int_0^{\frac{L}{c}} \phi_n(c\tau) \sin \omega_n(t-\tau) d\tau & \text{for } t > \frac{L}{c}, \end{cases} \tag{C.5}$$

yielding

$$q_n(t) = \begin{cases} \frac{b}{W_n} \Bigg(\frac{2c\beta_n^2 \sin \omega_n t}{\gamma_n^- \gamma_n^+} - \frac{2c^2 \beta_n^3 \zeta_n \cos \omega_n t}{\gamma_n^- \gamma_n^+} - \frac{\beta_n \sin c\beta_n t}{\gamma_n^-} \\ \quad + \frac{\beta_n \zeta_n \cos c\beta_n t}{\gamma_n^-} + \frac{\beta_n \sinh c\beta_n t}{\gamma_n^+} + \frac{\beta_n \zeta_n \cosh c\beta_n t}{\gamma_n^+} \Bigg) & \text{for } 0 < t \leq \frac{L}{c} \\ \frac{b}{W_n} \Bigg(\frac{2c\beta_n^2 \omega_n \sin \omega_n t}{\gamma_n^- \gamma_n^+} - \frac{2c^2 \beta_n^3 \zeta_n \cos \omega_n t}{\gamma_n^- \gamma_n^+} \\ \quad - \frac{c\beta^2(\zeta_n \gamma_n^+ \sin \beta_n L + \gamma_n^+ \cos \beta_n L - \zeta_n \gamma_n^- \sinh \beta_n L - \gamma_n^- \cosh \beta_n L) \sin \omega_n (t - \frac{L}{c})}{\omega_n \gamma_n^- \gamma_n^+} & \text{for } t > \frac{L}{c}, \\ \quad + \frac{\beta_n(-\gamma_n^+ \sin \beta_n L + \zeta_n \gamma_n^+ \cos \beta_n L + \gamma_n^- \sinh \beta_n L + \zeta_n \gamma_n^- \cosh \beta_n L) \cos \omega_n (t - \frac{L}{c})}{\gamma_n^- \gamma_n^+} \Bigg) \end{cases}$$

where $\gamma_n^- = c^2\beta_n^2 - \omega_n^2$ and $\gamma_n^+ = c^2\beta_n^2 + \omega_n^2$.

The parameters used for the example in Fig. 1(C) of the main manuscript are EI=70,000 MPa, ρ=2.7×10^{-9} tonne, w=10 mm, h=10 mm, L=100 mm, e=3 mm, P=10,000 N/mm, and c= 20,000 mm/s. The input pulse is applied for 0.005 s (=L/c), and the frequency spectrum is obtained for the 0.04 s of the response.

Metabeam Description and Design Parameters

A rectangular building block forming the external frame of the metabeam is composed of the linear springs with constants k_4, k_5, and k_6 connecting the point masses m_2 and m_3 at the top and bottom vertices, respectively, and two diagonal springs with constants k_7 and k_8 providing static stability to the frame [refer to Fig. 2(A) in the manuscript]. The baseline values for k_4, k_5, k_6, k_7, and k_8 are selected to have the same stiffness, 1,500 N/mm, for design simplicity. Stemming from the top and bottom masses are linear springs with constants k_2 and k_3 joining the center mass m_1 at an angle, forming a bistable mechanism. For the baseline unit cell design, k_2=1.076 N/mm and k_3= 0.6 N/mm are selected: the value of k_2 is chosen such that the spring forces are balanced in transverse direction[1] under small perturbations along the main lattice axis so that the unit cell mass does not incur an excessive transverse fluctuation while undergoing inter-well oscillations. Importantly, the general dynamics still remain valid for different sets of the stiffness values as is evident in *Tuning flexibility* section of the manuscript. The center masses of the neighboring bistable elements are then connected to one another by the linear inter-site springs with stiffness k_1. k_1= 1.241 N/mm is selected for the baseline design to minimize the discreteness effects of the lattice [45, 217]. The ratio between k_1 and the effective in-plane stiffness $k_{\text{eff}} = \left(\frac{k_2}{L_2^2+R^2} + \frac{k_3}{L_3^2+R^2}\right) R^2$ of the bistable unit cell affects the lattice discreteness and is ∼10 for the selected stiffness values. For the numerical simulations in this study, the mass proportional damping with a coefficient γ is applied to suppress unwanted transient dynamics. The coefficient is chosen to be γ= 9.91 s^{-1} for the baseline design such that the decay rate corresponds to the damping ratio ζ= 0.03 with respect to the fundamental structural mode. The governing equations of motion can be found in Sec. 12 of this Supplemental Material.

Table C.1 lists the sets of design parameters for all the metabeam designs appearing in this study. Design 1 shifts the operating frequency band (input frequencies initiating the solitonic resonance) to a higher frequency region. This is achieved by stiffening the springs forming the bistable elements (springs with constants k_2 and k_3) from the baseline design

[1]The metabeam is defined in a 2D space. In this study, the in-plane direction is the direction along the bistable lattice, and the out-of-plane (or, transverse) direction is the direction perpendicular to the in-plane direction.

since the transition wave generation, which leads to the solitonic resonance, is governed by the resonant excitation of the bistable unit cell in the in-plane direction. Design 2 shifts the output frequency of the solitonic resonance to a higher frequency region. The springs forming the external frames (springs with constants k_4, k_5, k_6, k_7, and k_8) govern the natural frequencies of the macrostructural modes and are thus stiffened to increase the output frequency. Design 3 and 4 demonstrate the extreme tunability that allows frequency conversion between frequencies several orders of magnitude apart. To achieve an extreme low-to-high (high-to-low) frequency conversion, the internal bistable microstructure of Design 3 (Design 4) is tuned to have a very low (high) natural frequency. For Design 5, the design parameters are adjusted to yield closely approximate values for the size of the metastructure (14 unit cells 27 mm apart), the natural frequency of the unit cell (65 Hz) and that of the macrostructure (4.62Hz) to those of the experimental demonstrator. Design 5-1 and Design 5-2 are variations of Design 5, where only the mass proportional damping coefficient values are increased and decreased, respectively, to observe the effect of system damping on the output frequency spectrum under low-frequency excitations.

Table C.1. Summary of the parameters for each metabeam design. The units of the stiffness k_{i}'s, mass m_{i}'s, distance L_{i}'s and R, and mass proportional damping coefficient γ are N/mm, g, mm, and s^{-1}, respectively. N is the number of unit cells forming the metabeam.

	k_1	k_2	k_3	$k_{4,5}$	k_6	$k_{7,8}$	m_1	$m_{2,3}$	L_1	L_2	L_3	R	γ	N
Baseline	1.241	1.076	0.6	1,500	1,500	1,500	2	1	20	40	20	8	9.91	30
Design 1	4.96	4.30	2.4	1,500	1,500	1,500	2	1	20	40	20	8	9.91	30
Design 2	1.241	1.076	0.6	6,000	6,000	6,000	2	1	20	40	20	8	9.91	30
Design 3	0.1	0.242	0.2	1600	100	800	20	10	25	55	45	8	0.708	20
Design 4	96.3	100.2	70	800	800	800	1	1	5	6	4	1.2	31.3	40
Design 5	2	6.28	5.7	6	0.4	5	3	6	27	50	45	10	1.710	14
Design 5-1	2	6.28	5.7	6	0.4	5	3	6	27	50	45	10	3.42	14
Design 5-2	2	6.28	5.7	6	0.4	5	3	6	27	50	45	10	0.285	14

Metabeams under a Different Boundary Condition

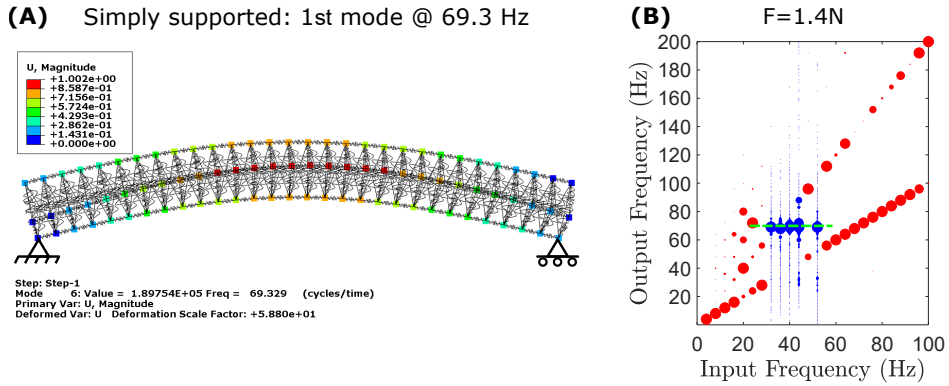

Figure C.1. (A) Fundamental structural mode of the baseline design under the simply-supported boundary condition. (B) The corresponding output frequency diagram under a large enough forcing amplitude (F= 1.4 N) to trigger transition waves.

The input-independent frequency conversion into a single dominant frequency (solitonic resonance) is a robust phenomenon not tied to a specific boundary condition. The simply-supported boundary condition is simulated by fixing the leftmost bottom node and constraining the out-of-plane motion of the rightmost bottom node. All design parameters are kept the same as those of the baseline design, and the changed boundary condition shifts the first structural mode to 69.3 Hz [Fig. C.1(A)]. For a sufficiently large input force that can trigger transition waves, the same characteristic behavior (input-independent output frequency at the structural mode) remains for the domain where transition waves are generated as shown in Fig. C.1(B).

Measuring Site Dependence

The dominant output frequency of the solitonic resonance depends on where the responses are measured. Since the transition waves are like a moving impulsive input caused by a traveling quasi-particle which has broad frequency band, the first few modes are simultaneously excited (the lower modes are stronger in general). When the responses are measured near the nodes of a particular mode shape, the contribution from that particular mode is masked as can be seen from the frequency response at 24^{th} site, where the 2^{nd} structural mode vanishes

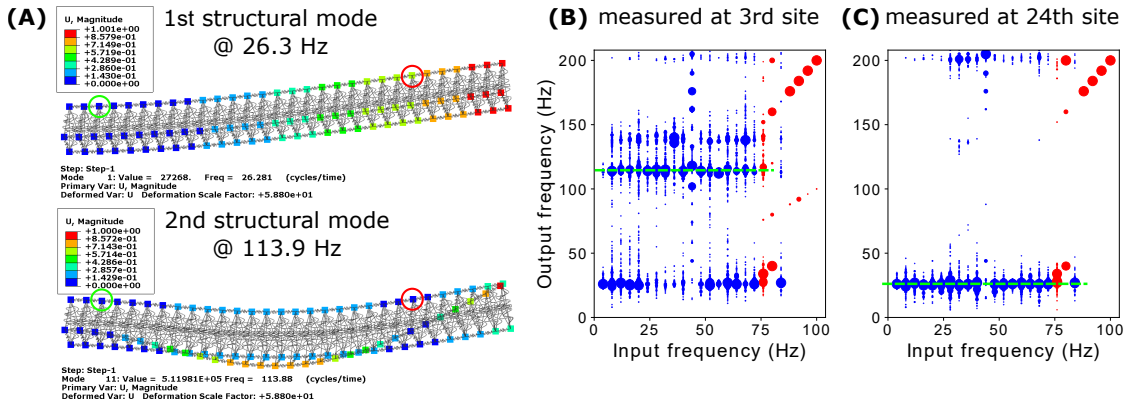

Figure C.2. Measuring site dependence on the dominant output frequency of solitonic resonance. (A) First and second structural mode shapes (B) Output frequency diagram measured at 3rd site (circled in green in the mode shapes) and 24th site (circled in red).

completely. On the contrary, the 2nd mode is more emphasized when measured at the 3rd node.

Amplification by Solitonic Resonance

Since solitonic resonance relies on a series of transition waves, which appear as high-orbit inter-well oscillations for each element of the underlying bistable lattice, a larger-amplitude macroscopic behavior is expected, compared to the case where transition waves are not triggered. At 32 Hz input frequency, for example, the critical forcing amplitude that enables solitonic resonance is about 0.6 N. The responses under forcing amplitudes just before and after solitonic resonance are plotted in Fig. C.3. Figure C.3(A) shows the in-plane displacements of the center node at the rightmost unit cell. The jumps between the two equilibrium points (0 mm and 16 mm) indicate that transition waves are triggered under 0.61 N input (plotted in blue), as opposed to small fluctuations about one of the equilibrium points under 0.59 N input (plotted in red).[2] Figure C.3(B) shows the corresponding out-of-plane displacements of the top node at the rightmost unit cell, and the maximum amplitude

[2]The in-plane displacements is larger near the excitation site (∼4 mm); however, their wave amplitudes do not propagate to the opposite end of the structure due to the system dissipation. Solitonic resonance do not exhibit such dissipation in wave amplitudes throughout the bistable lattice since unattenuated propagation is a hallmark of transition waves.

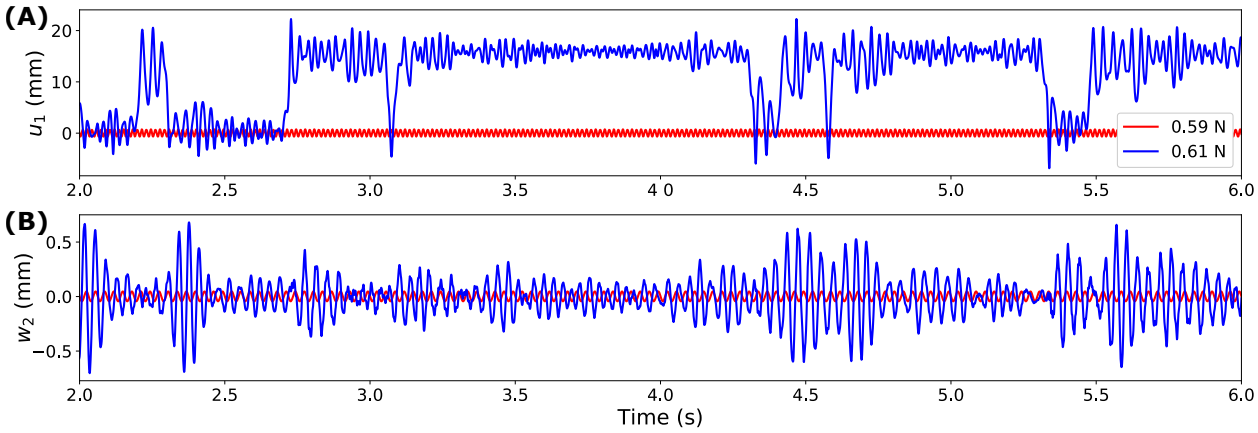

Figure C.3. (A) In-plane displacement of the center node and (B) the out-of-plane displacement of the top node at the rightmost unit cell under 32 Hz inputs near the critical forcing amplitude yielding solitonic resonance. There is drastic amplification of the motion when solitonic resonance occurs (at 0.61 N plotted in blue), compared to the case solitonic resonance is not triggered (at 0.59 N plotted in red).

is ∼14 times larger when solitonic resonance occurs than the case it does not. The increase in the forcing amplitude is only ∼3.4%, yet the output displacements associated with solitonic resonance is much larger. In other words, the excitation of solitonic resonance shows the hallmark signal amplification effect in resonant responses.

Solitonic Resonance from Noisy Sources

Solitonic resonance can also be excited by inputs with wideband spectra. To demonstrate this, we generate noisy signals by combining multiple sinusoidal inputs whose frequencies are incommensurate with one another to excite the metabeams. The frequency components are obtained from a power-law relationship $f_\mathrm{i} = \frac{1}{3}\pi \mathrm{i}^{1.42}$ between 0–200 Hz. The sinusoids are prepared with alternating phases to avoid an initial abrupt force peak; as time progresses, the combined signals become more randomly dispersed due to the incommensurate frequency relationship, thereby resulting in a noisy excitation. The final form of the noise is $n(t) = \sum_\mathrm{i} A_\mathrm{i}(-1)^{\mathrm{i}+1} \sin 2\pi f_\mathrm{i} t$, where A_i is the amplitude of each sinusoid, which is set equal to one another to simulate approximately randomly distributed excitation spectrum. In the limit, this tends to white noise. The mass proportional damping coefficient is reduced to

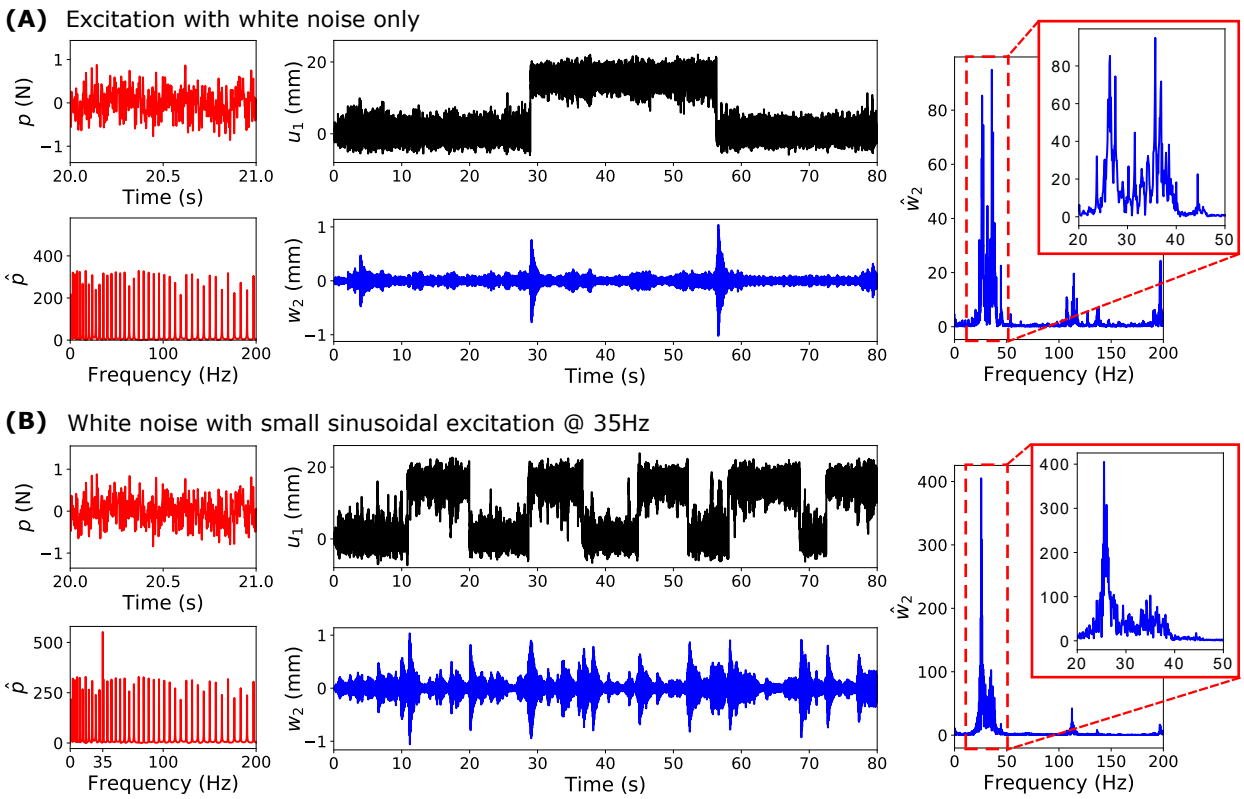

Figure C.4. Responses of the metabeam under (A) a white noise only and (B) a combined input with both white noise and small sinusoidal excitation. p is the input force, u_1 is the in-plane displacement obtained at the excitation site, w_2 is the out-of-plane displacement obtained at the top node of the rightmost unit cell, and $\hat{u}_1$ and $\hat{w}_2$ are the corresponding frequency contents obtained from the responses between 70–80 s.

3.30 s^{-1} from the baseline design to facilitate state transition, and the simulation is run for a sufficiently long period (80 s) to capture the random effects from the noisy inputs. The frequency contents are obtained from the responses between 70 s and 80 s.

The intensity of the noise is increased until an in-plane direction state transition is triggered at the excited element; the first occurrence of the state transition is observed at A= 0.066 N [see Fig. C.4(A)]. However, the rate of the occurrence of the transition waves is intermittent and random, which cannot be used as a reliable source of coherent output frequency generation. We add a small sinusoidal input (0.11 N at 35 Hz which is near the resonant frequency of the unit cell) on top of the noise to promote more frequent inter-well oscillations necessary for generating solitonic resonance. The effect of this additional input

component is small as the required forcing amplitude to trigger transition waves from a purely sinusoidal input at 35 Hz is ∼0.55 N. The output responses under this combined excitation are plotted in Fig. C.4(B). The in-plane displacement u_1 at the excitation site shows that inter-well oscillations occur more often when compared to the case under noise only. Specifically, the resulting out-of-plane displacement w_2 of the top node at the rightmost unit cell and its frequency content $\hat{w}_2$ display a single dominant output frequency near the macrostructural mode. In other words, a small fraction of the input energy otherwise required for a perfect system is enough to yield solitonic resonance under the presence of noise. Thus, solitonic resonance will be enhanced in realistic conditions, which inevitably are subjected to noisy perturbations. Importantly, this result implies that even noisy sources (e.g., colored inputs) can be transformed into a single coherent mode through the strongly nonlinear interaction with the metabeam.

Characteristic Time Responses

Four characteristic time responses that can be observed in the studied metabeam are plotted in Fig. C.5. For a very small force input, the output frequency directly corresponds to the input frequency [Fig. C.5(A)]. When operated in a weakly nonlinear regime, the second harmonic frequency begins to contribute to the output response. Depending on where the output frequencies fall on the dispersion relation, both of the frequency contributions may coexist [Fig. C.5(B)], or either of the contributions may cut off, leading to linear response or frequency doubling [Fig. C.5(C)][3]. Finally, solitonic resonance occurs when transition waves are triggered within the metabeam [Fig. C.5(D)]; the dominant frequency is totally unrelated to the input frequency.

Experimental Method

The experimental demonstrator was prepared by assemblying multiple parts printed with a fused-deposition-modeling 3D printer (Ultimaker 3 Extended). First, a lattice structure [the black component in Fig. 4(A) in the manuscript and Fig. C.6(A)] was 3D-printed in

[3]Their complete characterization will be addressed in a separate study

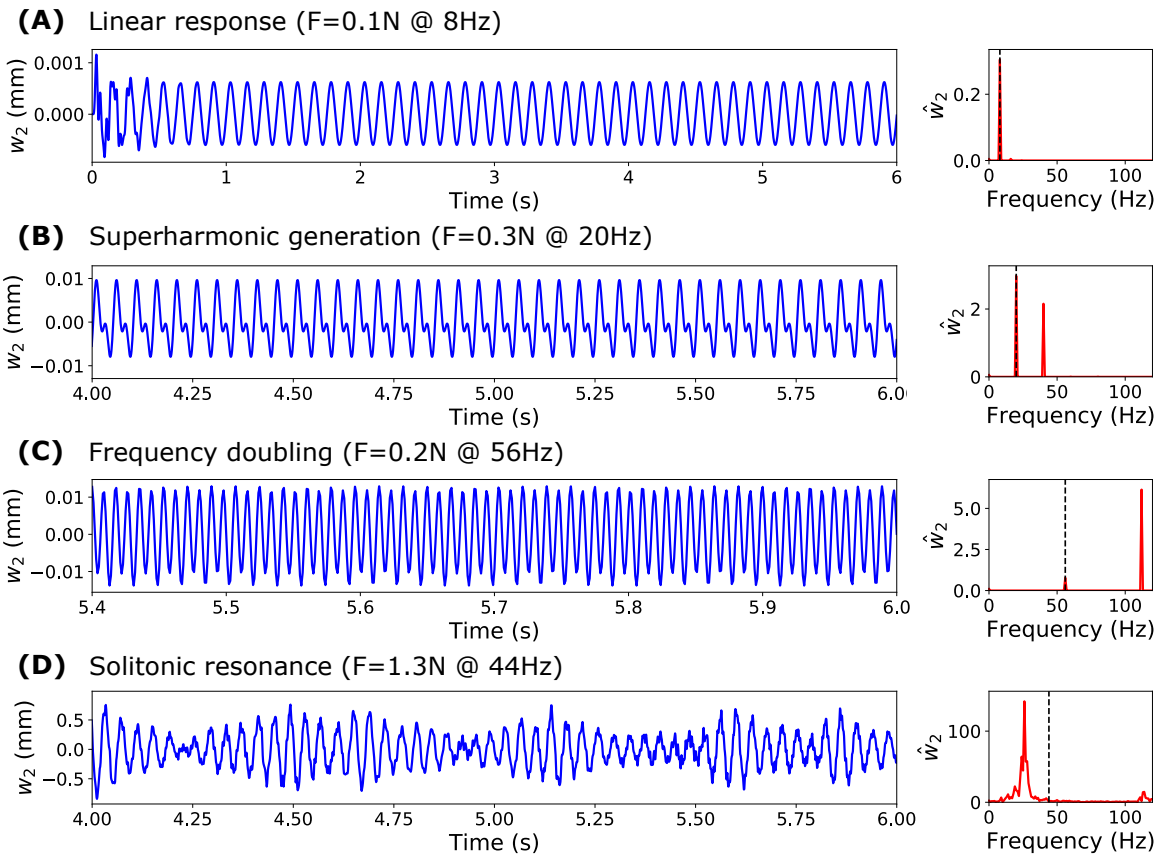

Figure C.5. Four characteristic time responses of the metabeam and their frequency contents: (A) linear response whose output frequency corresponds to the input frequency, (B) generation of superharmonic contribution to the input frequency, (C) frequency doubling, and (D) solitonic resonance. The input frequencies are indicated by the black dashed lines in the frequency spectra.

black PLA material, where the ribs are interconnected by spring-like features[4]. The lattice axis (along the intersite springs) was slightly offset from the centerline of the structure so as to amplify the flexural motion. Next, a set of four flexible holders [the white component in Fig. 4(A) and Fig. C.6(B)] are printed in white PLA and fitted with the flanges of the lattice structure. Upon assemblage, the holders precompress the lattice to allow two macroscopically different stable states [Fig. 4(A)-i,ii] and also to provide flexibility in the out-of-plane direction. To increase the inertia of unit cells, the cylindrical hole at the center of each unit cell is filled with ∼2.6 g of solder. The fixed-free boundary condition was realized by

[4]The maximum build plate size of Ultimaker 3 Extended is 215 mm, and so the lattice structure was printed in two pieces and glued together.

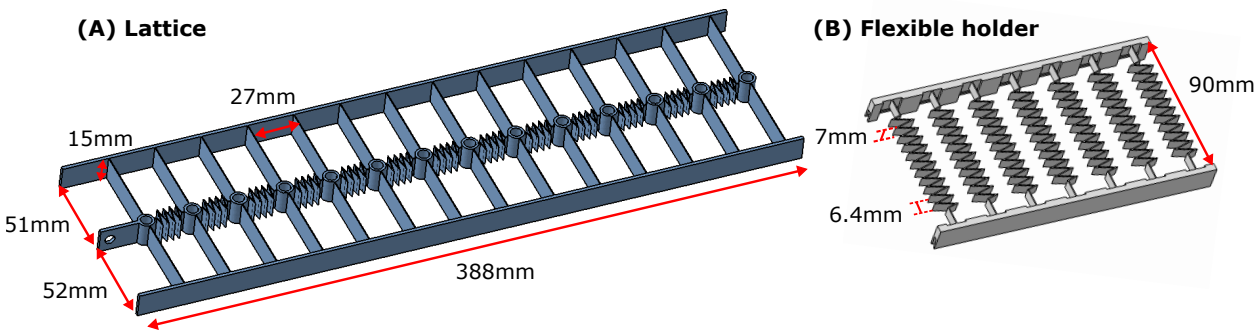

Figure C.6. CAD models for (A) the lattice and (B) the flexible holder with key geometric dimensions shown.

clamping the flanges at one end of the assembled structure to the rigid test rig and leaving the other end unconstrained [Fig. 4(A)-iii].

The metabeam was excited by APS 113 long-stroke electrodynamic shaker powered by APS 125 power amplifier. An open-loop control system was designed in Simulink, and a sinusoidal input signal was sent through dSpace data acquisition system (DS1104) to control the shaker. The amplitude of the input signal was controlled by manually changing the amplifier gain; the gain was increased until noticeable periodic motions started for the small-amplitude responses and until the transition waves were generated in the metabeam for the large-amplitude responses. Due to the shaker's limited capability, only approximate displacement-controlled tests were performed. Although the reaction force from the demonstrator affects the shaker force, its effect is minimal due to the heavy armature weight (2.5 kg), which is cross-checked by measuring the input displacements with a laser displacement sensor (Keyence LK-H157) pointing at the flat surface of the shaker head. The measured input displacements are almost sinusoidal with small contributions from the higher harmonics, which becomes vanishingly small as the input frequency increases further due to the increased inertial effect of the moving parts of the shaker[5]. The output responses were measured by another laser sensor, pointing to one of the beam surfaces near the free end as shown in Fig. 4(A)-iii.

[5]Refer to the following section for the measured displacements

Selected Experimental Results

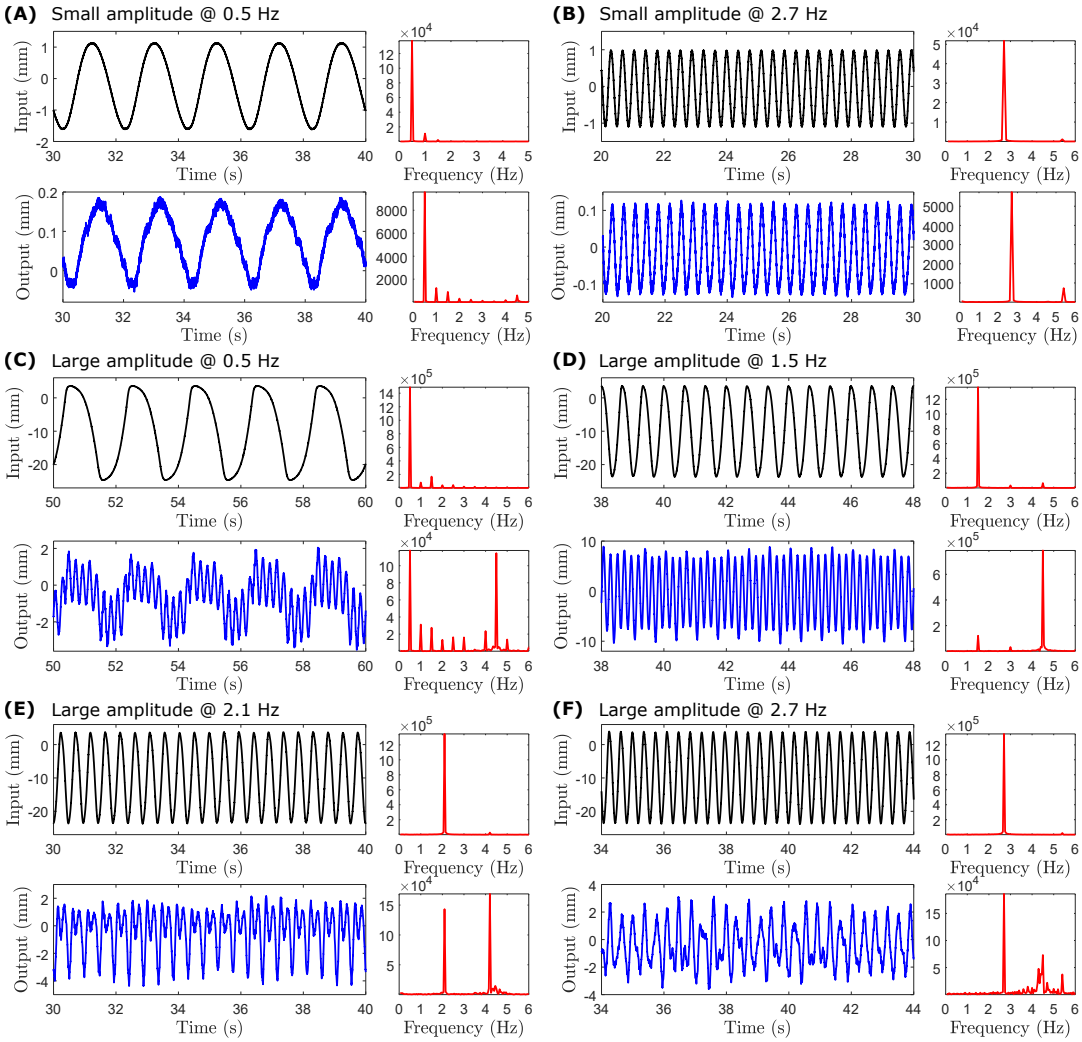

Figure C.7. Selected experimental results. (A,B) Metabeam response for 0.5 Hz and 2.7 Hz under small-amplitude displacement inputs yielding direct correspondence between the input and the dominant output frequencies. (C-E) Metabeam response for 0.5 Hz, 1.5 Hz, and 2.1 Hz under large-amplitude displacement inputs yielding superharmonic resonances of the input frequencies. (F) Metabeam response for 2.7 Hz, showing solitonic resonance, the frequency content of which is incommensurate with the input frequency.

Some of the measured time responses and the associated frequency contents are presented in Fig. C.7. The applied displacements are not purely sinusoidal but contain the harmonics of the input frequency due to the reaction force from the metabeam sample. However, these harmonic contributions are minimal compared to the input frequency, especially for

higher input frequencies. Under small-amplitude input displacements, the excited input frequencies are directly reflected in the output frequency content, exhibiting typical linear behaviors [Fig. C.7(A,B)]. For large-amplitude input displacements that trigger transition waves, the contributions from the harmonics of the input frequency are emphasized. For input frequencies whose integer multiples are close to the natural frequency of the metabeam (∼4.62 Hz), superharmonic resonances occur as can be identified by the spikes at the corresponding harmonics of the input frequencies [Fig. C.7(C-E)]. However, for input frequencies whose harmonics are not close to the natural frequency of the metabeam, a totally unrelated frequency band appears which is due to the transient effect from the generated transition waves [Fig. C.7(F)]. This constitutes incommensurate frequency generation, a signature of the solitonic resonance phenomenon.

Natural Frequencies of the Experimental Demonstrator

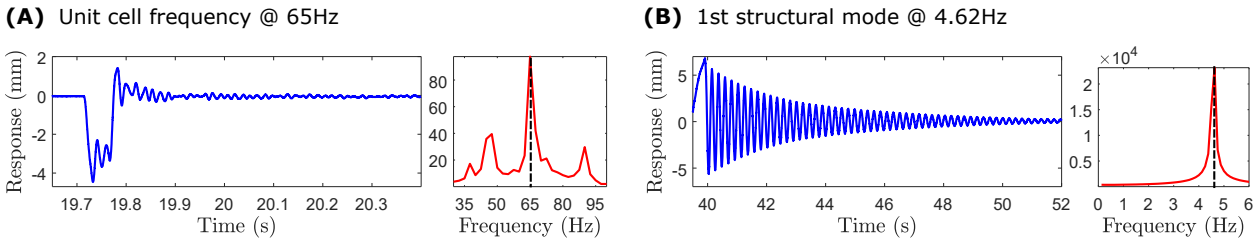

Figure C.8. Measured free vibration responses and the corresponding frequency contents for (A) the unit cell and (B) the macroscopic structure under impulsive inputs.

The natural frequency of the unit cell was obtained by gently hammering the first element in the in-plane direction and measuring its free response. The measured element was disconnected from the neighboring unit cell so as not to measure the natural frequencies of the coupled system modes. To find the dominant frequency, the response signal was analyzed between 20 s and 20.4 s, where the vibration amplitudes are small enough to minimize the shift from nonlinear effects. The dominant mode occurs at ∼65 Hz [Fig. C.8(A)]. For the structural mode, a small initial displacement was applied at the free end, and then the free response was measured. The signal was analyzed between 44 s and 52 s to obtain the frequency content, and the natural frequency is measured to be ∼4.62 Hz [Fig. C.8(B)].

Damping Effect in the Low Input Frequency Domain

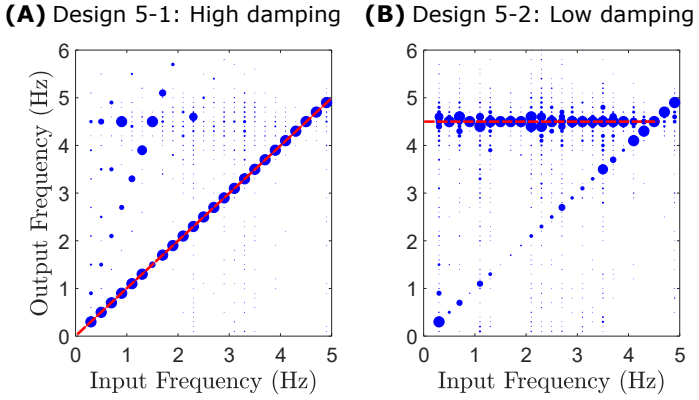

Figure C.9. Output frequency diagrams for the qualitatively similar numerical design under (A) high and (B) low system damping.

Since the output frequency branch near the macroscopic structural mode arises due to the repeated transient effects from the traveling transition waves, the degree of the system damping greatly affects which solution branch dominates the response. For a large proportional damping coefficient $\gamma = 3.42$ s^{-1}, twice larger than that of the qualitatively similar design in the manuscript (Design 5), the solitonic resonance branch begins to disappear [Fig. C.9(A)]. On the other hand, for very low proportional damping coefficient $\gamma = 0.285$ s^{-1}, which corresponds to damping ratio $\zeta = 0.005$ with respect to the fundamental structural mode, the solitonic resonance branch is accentuated, becoming qualitatively closer to a complete input-independent transformation [Fig. C.9(B)].

Governing Equations

Each unit cell of the metabeam has 6 degrees of freedom, and the equations of motion can be derived from the Euler-Lagrangian method. The Lagrangian $\mathcal{L} = \mathcal{T} - \mathcal{V}$ can be readily written as

$$\begin{aligned}\mathcal{T} &= \sum_{n-1}^{N}\left[\frac{1}{2}m_1(\dot{u}_{1,n}^2+\dot{w}_{1,n}^2)+\frac{1}{2}m_2(\dot{u}_{2,n}^2+\dot{w}_{2,n}^2)+\frac{1}{2}m_3(\dot{u}_{3,n}^2+\dot{w}_{3,n}^2)\right]\\ \mathcal{V} &= \sum_{n=1}^{N}\left[\frac{1}{2}k_2\Delta_2^2+\frac{1}{2}k_3\Delta_3^2+\frac{1}{2}k_6\Delta_6^2\right]+\sum_{n=1}^{N-1}\left[\frac{1}{2}k_1\Delta_1^2+\frac{1}{2}k_4\Delta_4^2+\frac{1}{2}k_5\Delta_5^2+\frac{1}{2}k_7\Delta_7^2+\frac{1}{2}k_8\Delta_8^2\right],\end{aligned} \tag{C.6}$$

where $\mathcal{T}$ and $\mathcal{L}$ are the system's total kinetic and potential energies, N is the number of unit cells, and $u_{m,n}$ and $w_{m,n}$ are the in-plane and out-of-plane displacements of the m^{th} mass of the n^{th} unit cell, respectively. The corresponding spring deflection Δ_{i} for each spring with stiffness k_{i} is given as:

$$
\begin{aligned}
\Delta_1 &= \sqrt{(L_1 + u_{1,n+1} - u_{1,n})^2 + (w_{1,n+1} - w_{1,n})^2} - L_1 \\
\Delta_2 &= \sqrt{(R + u_{2,n} - u_{1,n})^2 + (L_2 + w_{2,n} - w_{1,n})^2} - \sqrt{R^2 + L_2^2} \\
\Delta_3 &= \sqrt{(R + u_{3,n} - u_{1,n})^2 + (L_3 + w_{1,n} - w_{3,n})^2} - \sqrt{R^2 + L_3^2} \\
\Delta_4 &= \sqrt{(L_1 + u_{2,n+1} - u_{2,n})^2 + (w_{2,n+1} - w_{2,n})^2} - L_1 \\
\Delta_5 &= \sqrt{(L_1 + u_{3,n+1} - u_{3,n})^2 + (w_{3,n+1} - w_{3,n})^2} - L_1 \\
\Delta_6 &= \sqrt{(u_{2,n} - u_{3,n})^2 + (L_2 + L_3 + w_{2,n} - w_{3,n})^2} - (L_2 + L_3) \\
\Delta_7 &= \sqrt{(L_1 + u_{2,n+1} - u_{3,n})^2 + (L_2 + L_3 + w_{2,n+1} - w_{3,n})^2} - \sqrt{L_1^2 + (L_2 + L_3)^2} \\
\Delta_8 &= \sqrt{(L_1 + u_{3,n+1} - u_{2,n})^2 + (L_2 + L_3 + w_{2,n} - w_{3,n+1})^2} - \sqrt{L_1^2 + (L_2 + L_3)^2}.
\end{aligned}
\tag{C.7}
$$

Additionally, small dissipation is applied in the form of a mass proportional damping with a coefficient γ to suppress any unwanted transient effect. The full expressions of the governing equations for the n^{th} unit cell are shown at the end of this section.

The obtained set of discrete equations is highly coupled and nonlinear involving several radical expressions. There exists no exact solution, and thus we use a commercial numerical solver, Abaqus/Standard, for the numerical analyses. The built-in implicit solver uses Hilber-Hughes-Taylor method [214], but the numerical solution parameter α is set to zero so that the method becomes equivalent to the standard Newmark method. The baseline model, Design 1, and Design 2 are simulated for 6 s with the fixed time step Δt= 10^{-6} s, and the frequency contents are obtained from the time response between 5 s and 6 s. Design 3, Design 5, and its variations are simulated for 20 s with Δt= 10^{-5} s, and the frequency contents are obtained from the response between 10 s and 20 s. Design 4 is simulated for 8 s with Δt= 10^{-6} s, and the frequency contents are obtained from the response between 4 s and 8 s.

$$
\begin{aligned}
&m_1\ddot{u}_{1,n}+\gamma m_1\dot{u}_{1,n}+\frac{k_2\left(-u_{1,n}+u_{2,n}+R\right)\left(\sqrt{L_2^2+R^2}-\sqrt{\left(-w_{1,n}+w_{2,n}+L_2\right)^2+\left(-u_{1,n}+u_{2,n}+R\right)^2}\right)}{\sqrt{\left(-w_{1,n}+w_{2,n}+L_2\right)^2+\left(-u_{1,n}+u_{2,n}+R\right)^2}}\\
&+\frac{k_3\left(-u_{1,n}+u_{3,n}+R\right)\left(\sqrt{L_3^2+R^2}-\sqrt{\left(w_{1,n}-w_{3,n}+L_3\right)^2+\left(-u_{1,n}+u_{3,n}+R\right)^2}\right)}{\sqrt{\left(w_{1,n}-w_{3,n}+L_3\right)^2+\left(-u_{1,n}+u_{3,n}+R\right)^2}}\\
&+\frac{k_1\left(-u_{1,n\text{-}1}+u_{1,n}+L_1\right)\left(\sqrt{\left(-u_{1,n\text{-}1}+u_{1,n}+L_1\right)^2+\left(w_{1,n\text{-}1}-w_{1,n}\right)^2}-L_1\right)}{\sqrt{\left(-u_{1,n\text{-}1}+u_{1,n}+L_1\right)^2+\left(w_{1,n\text{-}1}-w_{1,n}\right)^2}}\\
&-\frac{k_1\left(-u_{1,n}+u_{1,n+1}+L_1\right)\left(\sqrt{\left(-u_{1,n}+u_{1,n+1}+L_1\right)^2+\left(w_{1,n}-w_{1,n+1}\right)^2}-L_1\right)}{\sqrt{\left(-u_{1,n}+u_{1,n+1}+L_1\right)^2+\left(w_{1,n}-w_{1,n+1}\right)^2}}=0,
\end{aligned}
\tag{C.8}
$$

$$
\begin{aligned}
&m_1\ddot{w}_{1,n}+\gamma m_1\dot{w}_{1,n}+\frac{k_2\left(-w_{1,n}+w_{2,n}+L_2\right)\left(\sqrt{L_2^2+R^2}-\sqrt{\left(-w_{1,n}+w_{2,n}+L_2\right)^2+\left(-u_{1,n}+u_{2,n}+R\right)^2}\right)}{\sqrt{\left(-w_{1,n}+w_{2,n}+L_2\right)^2+\left(-u_{1,n}+u_{2,n}+R\right)^2}}\\
&+\frac{k_3\left(w_{1,n}-w_{3,n}+L_3\right)\left(\sqrt{\left(w_{1,n}-w_{3,n}+L_3\right)^2+\left(-u_{1,n}+u_{3,n}+R\right)^2}-\sqrt{L_3^2+R^2}\right)}{\sqrt{\left(w_{1,n}-w_{3,n}+L_3\right)^2+\left(-u_{1,n}+u_{3,n}+R\right)^2}}\\
&+\frac{k_1\left(w_{1,n}-w_{1,n\text{-}1}\right)\left(\sqrt{\left(-u_{1,n\text{-}1}+u_{1,n}+L_1\right)^2+\left(w_{1,n\text{-}1}-w_{1,n}\right)^2}-L_1\right)}{\sqrt{\left(-u_{1,n\text{-}1}+u_{1,n}+L_1\right)^2+\left(w_{1,n\text{-}1}-w_{1,n}\right)^2}}\\
&+\frac{k_1\left(w_{1,n}-w_{1,n+1}\right)\left(\sqrt{\left(-u_{1,n}+u_{1,n+1}+L_1\right)^2+\left(w_{1,n}-w_{1,n+1}\right)^2}-L_1\right)}{\sqrt{\left(-u_{1,n}+u_{1,n+1}+L_1\right)^2+\left(w_{1,n}-w_{1,n+1}\right)^2}}=0,
\end{aligned}
\tag{C.9}
$$

$$
\begin{aligned}
&m_2\ddot{u}_{2,n}+\gamma m_2\dot{u}_{2,n}+\frac{k_2\left(-u_{1,n}+u_{2,n}+R\right)\left(\sqrt{\left(-w_{1,n}+w_{2,n}+L_2\right)^2+\left(-u_{1,n}+u_{2,n}+R\right)^2}-\sqrt{L_2^2+R^2}\right)}{\sqrt{\left(-w_{1,n}+w_{2,n}+L_2\right)^2+\left(-u_{1,n}+u_{2,n}+R\right)^2}}\\
&+\frac{k_4\left(-u_{2,n\text{-}1}+u_{2,n}+L_1\right)\left(\sqrt{\left(-u_{2,n\text{-}1}+u_{2,n}+L_1\right)^2+\left(w_{2,n\text{-}1}-w_{2,n}\right)^2}-L_1\right)}{\sqrt{\left(-u_{2,n\text{-}1}+u_{2,n}+L_1\right)^2+\left(w_{2,n\text{-}1}-w_{2,n}\right)^2}}\\
&-\frac{k_4\left(-u_{2,n}+u_{2,n+1}+L_1\right)\left(\sqrt{\left(-u_{2,n}+u_{2,n+1}+L_1\right)^2+\left(w_{2,n}-w_{2,n+1}\right)^2}-L_1\right)}{\sqrt{\left(-u_{2,n}+u_{2,n+1}+L_1\right)^2+\left(w_{2,n}-w_{2,n+1}\right)^2}}\\
&+\frac{k_7\left(u_{2,n}-u_{3,n\text{-}1}+L_1\right)\left(\sqrt{\left(u_{2,n}-u_{3,n\text{-}1}+L_1\right)^2+\left(w_{2,n}-w_{3,n\text{-}1}+L_2+L_3\right)^2}-\sqrt{L_1^2+\left(L_2+L_3\right)^2}\right)}{\sqrt{\left(u_{2,n}-u_{3,n\text{-}1}+L_1\right)^2+\left(w_{2,n}-w_{3,n\text{-}1}+L_2+L_3\right)^2}}\\
&+\frac{k_6\left(u_{2,n}-u_{3,n}\right)\left(\sqrt{\left(w_{2,n}-w_{3,n}+L_2+L_3\right)^2+\left(u_{2,n}-u_{3,n}\right)^2}-L_2-L_3\right)}{\sqrt{\left(w_{2,n}-w_{3,n}+L_2+L_3\right)^2+\left(u_{2,n}-u_{3,n}\right)^2}}\\
&-\frac{k_8\left(-u_{2,n}+u_{3,n+1}+L_1\right)\left(\sqrt{\left(-u_{2,n}+u_{3,n+1}+L_1\right)^2+\left(w_{2,n}-w_{3,n+1}+L_2+L_3\right)^2}-\sqrt{L_1^2+\left(L_2+L_3\right)^2}\right)}{\sqrt{\left(-u_{2,n}+u_{3,n+1}+L_1\right)^2+\left(w_{2,n}-w_{3,n+1}+L_2+L_3\right)^2}}=0,
\end{aligned}
\tag{C.10}
$$

$$
\begin{aligned}
&m_2\ddot{w}_{2,n}+\gamma m_2\dot{w}_{2,n}+\frac{k_2\left(-w_{1,n}+w_{2,n}+L_2\right)\left(\sqrt{\left(-w_{1,n}+w_{2,n}+L_2\right)^2+\left(-u_{1,n}+u_{2,n}+R\right)^2}-\sqrt{L_2^2+R^2}\right)}{\sqrt{\left(-w_{1,n}+w_{2,n}+L_2\right)^2+\left(-u_{1,n}+u_{2,n}+R\right)^2}}\\
&+\frac{k_4\left(w_{2,n}-w_{2,n\text{-}1}\right)\left(\sqrt{\left(-u_{2,n\text{-}1}+u_{2,n}+L_1\right)^2+\left(w_{2,n\text{-}1}-w_{2,n}\right)^2}-L_1\right)}{\sqrt{\left(-u_{2,n\text{-}1}+u_{2,n}+L_1\right)^2+\left(w_{2,n\text{-}1}-w_{2,n}\right)^2}}\\
&+\frac{k_4\left(w_{2,n}-w_{2,n+1}\right)\left(\sqrt{\left(-u_{2,n}+u_{2,n+1}+L_1\right)^2+\left(w_{2,n}-w_{2,n+1}\right)^2}-L_1\right)}{\sqrt{\left(-u_{2,n}+u_{2,n+1}+L_1\right)^2+\left(w_{2,n}-w_{2,n+1}\right)^2}}\\
&+\frac{k_7\left(w_{2,n}-w_{3,n\text{-}1}+L_2+L_3\right)\left(\sqrt{\left(u_{2,n}-u_{3,n\text{-}1}+L_1\right)^2+\left(w_{2,n}-w_{3,n\text{-}1}+L_2+L_3\right)^2}-\sqrt{L_1^2+\left(L_2+L_3\right)^2}\right)}{\sqrt{\left(u_{2,n}-u_{3,n\text{-}1}+L_1\right)^2+\left(w_{2,n}-w_{3,n\text{-}1}+L_2+L_3\right)^2}}\\
&+\frac{k_6\left(w_{2,n}-w_{3,n}+L_2+L_3\right)\left(\sqrt{\left(w_{2,n}-w_{3,n}+L_2+L_3\right)^2+\left(u_{2,n}-u_{3,n}\right)^2}-L_2-L_3\right)}{\sqrt{\left(w_{2,n}-w_{3,n}+L_2+L_3\right)^2+\left(u_{2,n}-u_{3,n}\right)^2}}\\
&+\frac{k_8\left(w_{2,n}-w_{3,n+1}+L_2+L_3\right)\left(\sqrt{\left(-u_{2,n}+u_{3,n+1}+L_1\right)^2+\left(w_{2,n}-w_{3,n+1}+L_2+L_3\right)^2}-\sqrt{L_1^2+\left(L_2+L_3\right)^2}\right)}{\sqrt{\left(-u_{2,n}+u_{3,n+1}+L_1\right)^2+\left(w_{2,n}-w_{3,n+1}+L_2+L_3\right)^2}}=0,
\end{aligned}
\tag{C.11}
$$

$$
\begin{aligned}
&m_3\ddot{u}_{3,n}+\gamma m_3\dot{u}_{3,n}+\frac{k_3\left(-u_{1,n}+u_{3,n}+R\right)\left(\sqrt{\left(w_{1,n}-w_{3,n}+L_3\right)^2+\left(-u_{1,n}+u_{3,n}+R\right)^2}-\sqrt{L_3^2+R^2}\right)}{\sqrt{\left(w_{1,n}-w_{3,n}+L_3\right)^2+\left(-u_{1,n}+u_{3,n}+R\right)^2}}\\
&+\frac{k_8\left(-u_{2,n\text{-}1}+u_{3,n}+L_1\right)\left(\sqrt{\left(-u_{2,n\text{-}1}+u_{3,n}+L_1\right)^2+\left(w_{2,n\text{-}1}-w_{3,n}+L_2+L_3\right)^2}-\sqrt{L_1^2+\left(L_2+L_3\right)^2}\right)}{\sqrt{\left(-u_{2,n\text{-}1}+u_{3,n}+L_1\right)^2+\left(w_{2,n\text{-}1}-w_{3,n}+L_2+L_3\right)^2}}\\
&-\frac{k_6\left(u_{2,n}-u_{3,n}\right)\left(\sqrt{\left(w_{2,n}-w_{3,n}+L_2+L_3\right)^2+\left(u_{2,n}-u_{3,n}\right)^2}-L_2-L_3\right)}{\sqrt{\left(w_{2,n}-w_{3,n}+L_2+L_3\right)^2+\left(u_{2,n}-u_{3,n}\right)^2}}\\
&-\frac{k_7\left(u_{2,n+1}-u_{3,n}+L_1\right)\left(\sqrt{\left(u_{2,n+1}-u_{3,n}+L_1\right)^2+\left(w_{2,n+1}-w_{3,n}+L_2+L_3\right)^2}-\sqrt{L_1^2+\left(L_2+L_3\right)^2}\right)}{\sqrt{\left(u_{2,n+1}-u_{3,n}+L_1\right)^2+\left(w_{2,n+1}-w_{3,n}+L_2+L_3\right)^2}}\\
&+\frac{k_5\left(-u_{3,n\text{-}1}+u_{3,n}+L_1\right)\left(\sqrt{\left(-u_{3,n\text{-}1}+u_{3,n}+L_1\right)^2+\left(w_{3,n\text{-}1}-w_{3,n}\right)^2}-L_1\right)}{\sqrt{\left(-u_{3,n\text{-}1}+u_{3,n}+L_1\right)^2+\left(w_{3,n\text{-}1}-w_{3,n}\right)^2}}\\
&-\frac{k_5\left(-u_{3,n}+u_{3,n+1}+L_1\right)\left(\sqrt{\left(-u_{3,n}+u_{3,n+1}+L_1\right)^2+\left(w_{3,n}-w_{3,n+1}\right)^2}-L_1\right)}{\sqrt{\left(-u_{3,n}+u_{3,n+1}+L_1\right)^2+\left(w_{3,n}-w_{3,n+1}\right)^2}}=0,
\end{aligned}
\tag{C.12}
$$

$$
\begin{aligned}
&m_3\ddot{w}_{3,n}+\gamma m_3\dot{w}_{3,n}+\frac{k_3\left(w_{1,n}-w_{3,n}+L_3\right)\left(\sqrt{L_3^2+R^2}-\sqrt{\left(w_{1,n}-w_{3,n}+L_3\right)^2+\left(-u_{1,n}+u_{3,n}+R\right)^2}\right)}{\sqrt{\left(w_{1,n}-w_{3,n}+L_3\right)^2+\left(-u_{1,n}+u_{3,n}+R\right)^2}}\\
&-\frac{k_8\left(w_{2,n\text{-}1}-w_{3,n}+L_2+L_3\right)\left(\sqrt{\left(-u_{2,n\text{-}1}+u_{3,n}+L_1\right)^2+\left(w_{2,n\text{-}1}-w_{3,n}+L_2+L_3\right)^2}-\sqrt{L_1^2+\left(L_2+L_3\right)^2}\right)}{\sqrt{\left(-u_{2,n\text{-}1}+u_{3,n}+L_1\right)^2+\left(w_{2,n\text{-}1}-w_{3,n}+L_2+L_3\right)^2}}\\
&-\frac{k_6\left(w_{2,n}-w_{3,n}+L_2+L_3\right)\left(\sqrt{\left(w_{2,n}-w_{3,n}+L_2+L_3\right)^2+\left(u_{2,n}-u_{3,n}\right)^2}-L_2-L_3\right)}{\sqrt{\left(w_{2,n}-w_{3,n}+L_2+L_3\right)^2+\left(u_{2,n}-u_{3,n}\right)^2}}\\
&-\frac{k_7\left(w_{2,n+1}-w_{3,n}+L_2+L_3\right)\left(\sqrt{\left(u_{2,n+1}-u_{3,n}+L_1\right)^2+\left(w_{2,n+1}-w_{3,n}+L_2+L_3\right)^2}-\sqrt{L_1^2+\left(L_2+L_3\right)^2}\right)}{\sqrt{\left(u_{2,n+1}-u_{3,n}+L_1\right)^2+\left(w_{2,n+1}-w_{3,n}+L_2+L_3\right)^2}}\\
&+\frac{k_5\left(w_{3,n}-w_{3,n\text{-}1}\right)\left(\sqrt{\left(-u_{3,n\text{-}1}+u_{3,n}+L_1\right)^2+\left(w_{3,n\text{-}1}-w_{3,n}\right)^2}-L_1\right)}{\sqrt{\left(-u_{3,n\text{-}1}+u_{3,n}+L_1\right)^2+\left(w_{3,n\text{-}1}-w_{3,n}\right)^2}}\\
&+\frac{k_5\left(w_{3,n}-w_{3,n+1}\right)\left(\sqrt{\left(-u_{3,n}+u_{3,n+1}+L_1\right)^2+\left(w_{3,n}-w_{3,n+1}\right)^2}-L_1\right)}{\sqrt{\left(-u_{3,n}+u_{3,n+1}+L_1\right)^2+\left(w_{3,n}-w_{3,n+1}\right)^2}}=0.
\end{aligned}
\tag{C.13}
$$

Movie S1: Solitonic Resonance

Movie S1 shows simulations of solitonic resonance responses obtained under F= 1.7 N at 8 Hz, 36 Hz and 68 Hz. The first half (starting at 3 s) of the playback shows the animated results between 4 s and 5 s in the simulations time. Transition wave propagation within each metabeams is observable from the recurrent oscillations of the bistable elements between the stable points. To identify the macroscopic structural motion better, the out-of-plane (Y-direction in the simulation coordinate) deformations are scaled by ten times for the second half (starting at 19 s) of the playback. The stable propagation of the compression and rarefaction wave groups bolsters quasi-particle nature of the transition waves. Even though the input frequencies are drastically different, the out-of-plane motions occur at a similar frequency, indicating input-independent frequency conversion.

Movie S2: Experimental Demonstration

Movie S2 shows an experimental observation of solitonic resonance under 1.1 Hz displacement input large enough to trigger transition waves. As transition waves propagate within the metabeam, a series of free vibrations near the natural frequency of the structure occurs, yielding an output frequency contribution different from the input frequency. The solitonic resonance is manifested by the faster transverse vibration than the input frequency.

D. SUPPLEMENTARY INFORMATION FOR HIGH-PERFORMANCE COMPUTING ARCHITECTURE FOR PARALLELIZED COMPUTATION OF METASTRUCTURES COMPOSED OF MULTI-STABLE UNIT CELLS

Design Parameters

The following single unit cell design in Tab. D.1 is used throughout all the simulations of the metabeam problems, where the definitions of the parameters are given in Ref. [205]. Only the number of the unit cells are varied among the analyses: N=30 is used for the code validation and numerical performance analyses; three different values for N (128, 1024, 16384) are used for the strong scaling analysis; proportionally scaled sizes to the number of processes for the weak scaling analysis; and, N=80,001 is used for the nonlinear energy flow example.

Table D.1. Summary of the metabeam design parameters. The units of the stiffness k_{i}'s, mass m_{i}'s, distance L_{i}'s and R, and mass proportional damping coefficient γ are N/mm, g, mm, and s^{-1}, respectively. The parameter definitions follow those in Ref. [205]

k_1	k_2	k_3	k_4, k_5	k_6	k_7, k_8	m_1	m_2, m_3	L_1	L_2	L_3	R	γ
1.241	1.076	0.6	100	100	100	2	1	20	40	20	8	9.91

For the 1D lattice of quartic onsite potentials (discrete ϕ-4 model), the following form of the governing equation is used:

$$m\ddot{u}_n = k(u_{n+1} - 2u_n + u_{n-1}) - (C_1 + 2C_2u_n + 3C_3u_n^2 + 4C_4u_n^3) - b\dot{u}_n, \tag{D.1}$$

where u_n is the displacement of the n^{th} unit cell, m is the mass of the unit cell, k is the inter-site spring stiffness, C_{i}'s are the coefficients of the quartic onsite potential, and b is the onsite damping coefficient. The design parameters for the ϕ-4 lattices used in this study are listed in Tab. D.2.

Table D.2. Summary of the design parameters for 1D bi-stable lattices.

Design	k	C_1	C_2	C_3	C_4	b
Discrete asymmetric	1	-0.036	-0.060	0.012	0.030	0.1
Continuous asymmetric	1	-0.0090	-0.0150	0.0030	0.0075	0.1
Discrete symmetric	1	0	-0.015	0	0.0075	0
Propagation speed	1	0	-0.03	0	0.015	0

Lastly, the governing equation for the multi-stable lattice with coupled pendula (discrete sine-Gordon model) can be written as:

$$I\ddot{\theta}_n = k_\theta(\theta_{n+1} - 2\theta_n + \theta_{n-1}) - mgl\sin\theta_n - b_\theta\dot{\theta}_n, \tag{D.2}$$

where θ_n is the rotation of the n^{th} pendulum, I is the moment of inertia of the pedulum about the rotational axis, k_θ is the stiffness of the torsional spring coupling two neighboring pendula, m is the tip mass of the pendulum, g is the gravitational constant, l is the length of the pendulum, and b_θ is the rotational damping coefficient. A simple canonical design is used for the code validation. The values of I, k_θ, m, g, and l are all set to 1 for the numerical simplicity, while and b_θ is set to 0.

Code Validation for the 1D Lattices

The exact solution for the discrete 1D lattice with quartic onsite potentials does not exist just as the metabeam problem. Hence, its correct implementation is validated by comparing the solutions obtained from our code's RK4 method with those from the Matlab code used in the previous studies [97], which uses 2^{nd}-order accurate central difference method. Three example cases are considered: first, a bi-stable lattice with asymmetric onsite potentials, where the ratio between the inter-site and onsite stiffness are small, signifying a typical discrete behavior; second, a similar lattice with asymmetric onsite potentials but with a large inter-site to onsite stiffness ratio, signifying a more continuous behavior; lastly, a bi-stable lattice with symmetric onsite potentials. All three designs are composed of 500 unit cells, and the corresponding design parameters are listed in **Design Parameters** section.

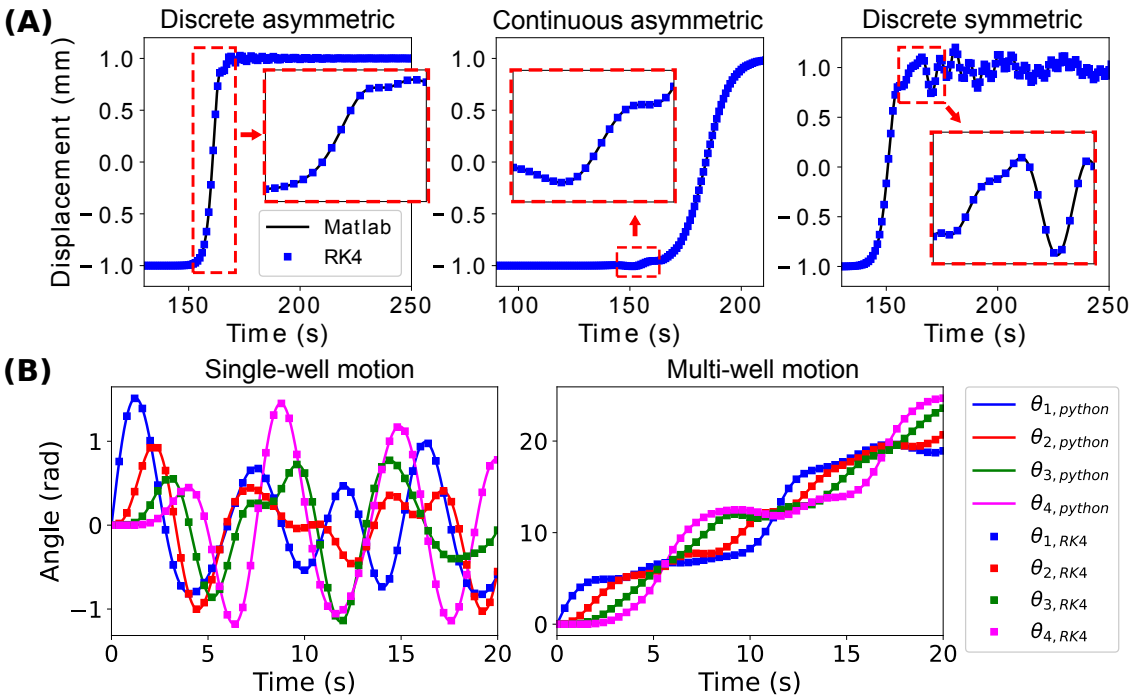

Figure D.1. (A) Code validation for the discrete 1D lattice with quartic onsite potentials. The displacements of the 100$^{\text{th}}$ element from our code's RK4 method are plotted for discrete asymmetric, continuous asymmetric, and discrete symmetric designs and compared with those obtained with the Matlab code in the previous work [97]. (B) Code validation for the 1D multi-stable lattice with coupled pendula. The response angles of the 3$^{\text{rd}}$ element from a built-in Python function and our code's RK4 method are compared for two qualitatively different motions (one bounded in a single potential well, the other traversing through multiple wells).

The transition waves are triggered by prescribing initial velocities to the first unit cells, the velocities of which are 2 m/s for both of the asymmetric cases and 1 m/s for the symmetric case. The responses are simulated for 400 s with Δt=0.01 s. Figure D.1(A) shows the displacements of the 100$^{\text{th}}$ unit cell for each design, obtained from both codes. For all of the example cases, the solutions match closely, and the RMS errors between the solutions from the two codes are 1.721×10^{-4} mm, 3.39×10^{-4} mm, and 4.29×10^{-4} mm, respectively.

In order to validate the implementation of the discrete sine-Gordon model, a system of four coupled pendula is used (the design parameters can be found in **Design Parameters** section). Two qualitatively different behaviors are tested by imposing different initial velocity $\dot{\theta}_1(0)$ at the first element. With $\dot{\theta}_1(0)$= 2.0, the motion is confined in a single potential

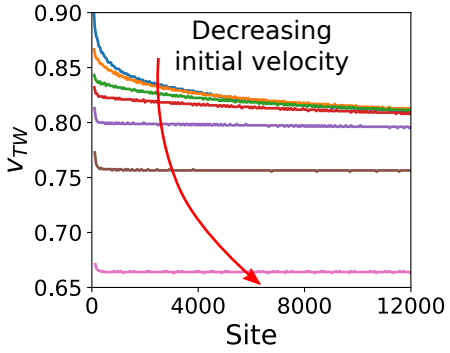

Figure D.2. Propagation speeds of the transition waves in a discrete ϕ-4 lattice under various initial velocities of the transition waves.

well; with $\dot{\theta}_1(0)= 4.6$, the motion traverses multiple wells (a transition wave is generated). The reference solution sets are obtained from odeint method in SciPy's (a Python library) *integrate* module. The responses obtained from the RK4 method of our code are plotted together with the reference sets in Fig. D.1(B), again showing almost exact agreement with each other. For example, the RMS errors for the time response of the 3$^{\text{rd}}$ element between the two methods are 5.80×10^{-4} rad and 1.394×10^{-3} rad, respectively, which are small compared to the ranges of it motion.

Propagation Speeds of the Transition Waves in ϕ-4 Lattices

For the continuum limit of a ϕ-4 lattice with symmetric onsite potential, there is a known theoretical solution for the displacement $u(x,t)$ in the following canonical form: $u(x,t) = \tanh\frac{x-vt}{\sqrt{2}\sqrt{1-v^2}}$ [45], where x and v are the spatial coordinate and the constant propagation speed of the transition wave. This particular solution indicates that the transition wave has an invariant waveform for any subsonic propagation. It is of interest to see if such a d'Alembert's (traveling at a constant speed) solution exists for the discrete ϕ-4 lattice as well. A transition wave can be easily generated by imposing an initial velocity to the first unit cell. However, this initial velocity does not directly translate into the initial propagation speed of the transition wave since the transition wave is the product of chaotic snap-through dynamics. Dissipation in this type of lattice is known to result in the spatial attenuation for the linear waves (phonons) but slow down the waves itself for the transition waves [170].

Hence, to manipulate the propagation speed of the transition wave, we additionally impose onsite damping to the first few unit cells. The longer the dissipation region spans, the slower the transition wave becomes.

Numerically, the propagation speed v_{TW} of the transition wave can be obtained by finding the zero crossings of the time responses at two nearby sites and then dividing the distance between the two sites by their time difference. Figure D.2 shows the instantaneous propagation speeds of the transition waves for various initial velocities imposed to a homogeneous lattice composed of 20,000 bi-stable unit cells, where the same unit cell design as the discrete symmetric case in **Code Validation for the 1D Lattices** section is used. As opposed to the theoretical traveling wave solution in the continuous ϕ-4 lattice, the transition wave in the discrete counterpart does not always propagate at a constant speed. Rather, there seems to exist a certain critical value, below which the propagation speed is quickly settled to a constant value within the first few unit cells and remain constant throughout the length of the lattice (e.g., the bottom three curves) but above which the propagation speed continuously decreases at a slow, diminishing rate (e.g., the top four curves). This behavior is presumably due to the lattice discreteness effect coupled with the interaction with the allowed phased speeds of the phonons. In a discrete lattice, oscillatory tails (phonons) are generated as a result of snap-through transitions that the traveling transition wave yields. If the propagation speeds of these oscillatory tails are lower than the speed of the transition wave, the transition wave constantly loses a portion of its transport energy for the generation of these tails, hence slowing down. On the contrary, if the speeds of the tails are greater, the tails and the main transition wave are always interacting with each other, conserving its transport energy. The verification of this postulate and more in-depth investigation on the stability of the transition wave speed in a discrete ϕ-4 lattice will be addressed in a separate study.

VITA

Myungwon Hwang was born in Jinju, South Korea, on October 6th, 1987. He received his Bachelor's (2009) and Master's (2011) degrees in Aerospace Engineering from Georgia Institute of Technology. As a master student, he was involved in the development of a computational tool simulating ground vibration tests of HALE aircraft, using geometrically exact beam theory. Between 2011 and 2014, he worked as a system and CAE engineer at DTR Corp., an automotive engine mount manufacturer in Korea. He joined Prof. Arrieta's Programmable Structures Lab at Purdue University in 2016 and continued for a Doctoral degree in Mechanical Engineering. His research interest includes vibrations and wave propagation in metastructures and interconnecting the observed phenomena with particle theory. Outside of work, he likes following automotive vlogs and playing the classic guitar.